INVESTIGATION OF COMPLEX REFRACTIVE INDEX OF GRAPHENE OXIDE USING POLARISATION RESPONSE OF GRAPHENE OXIDE-COATED PLANARIZED OPTICAL WAVEGUIDE

GAN SOON XIN

FACULTY OF SCIENCE

UNIVERSITI MALAYA

KUALA LUMPUR

2020

INVESTIGATION OF COMPLEX REFRACTIVE INDEX OF GRAPHENE OXIDE USING POLARISATION RESPONSE OF GRAPHENE OXIDE-COATED PLANARIZED OPTICAL WAVEGUIDE

GAN SOON XIN

DISSERTATION SUBMITTED IN FULFILMENT OF THE REQUIREMENTS FOR THE DEGREE OF MASTER OF SCIENCE

DEPARTMENT OF PHYSICS
FACULTY OF SCIENCE
UNIVERSITI MALAYA
KUALA LUMPUR

2020

UNIVERSITI MALAYA

ORIGINAL LITERARY WORK DECLARATION

Name of Candidate: **GAN SOON XIN**

Matric No: **SMA170060**

Name of Degree: **MASTER OF SCIENCE (M. Sc.)**

Title of Project Paper/Research Report/Dissertation/Thesis ("this Work"):

INVESTIGATION OF COMPLEX REFRACTIVE INDEX OF GRAPHENE OXIDE USING POLARISATION RESPONSE OF GRAPHENE OXIDE-COATED PLANARIZED OPTICAL WAVEGUIDE

Field of Study: **EXPERIMENTAL PHYSICS**

I do solemnly and sincerely declare that:

(1) I am the sole author/writer of this Work;
(2) This Work is original;
(3) Any use of any work in which copyright exists was done by way of fair dealing and for permitted purposes and any excerpt or extract from, or reference to or reproduction of any copyright work has been disclosed expressly and sufficiently and the title of the Work and its authorship have been acknowledged in this Work;
(4) I do not have any actual knowledge nor do I ought reasonably to know that the making of this work constitutes an infringement of any copyright work;
(5) I hereby assign all and every rights in the copyright to this Work to the University of Malaya ("UM"), who henceforth shall be owner of the copyright in this Work and that any reproduction or use in any form or by any means whatsoever is prohibited without the written consent of UM having been first had and obtained;
(6) I am fully aware that if in the course of making this Work I have infringed any copyright whether intentionally or otherwise, I may be subject to legal action or any other action as may be determined by UM.

Candidate's Signature Date:

Subscribed and solemnly declared before,

Witness's Signature Date:

Name:

Designation:

INVESTIGATION OF COMPLEX REFRACTIVE INDEX OF GRAPHENE OXIDE USING POLARISATION RESPONSE OF GRAPHENE OXIDE-COATED PLANARIZED OPTICAL WAVEGUIDE

ABSTRACT

Since a single atomic layer of carbon, also as known as graphene is being successfully exfoliated from 3D graphite, intense research on graphene and its derivative begins. Among them, graphene oxide (GO) is considered one of the most prominent candidates in the category of graphene derivatives for the application of electronic, optoelectronic and photonics. However, although GO has been applied in many applications like saturable absorbers of Q-switch laser and optical limiters for eye protection, its intrinsic optical properties especially complex refractive index reported so far still has a large deviation. Also, most of the optical characterization research on GO were conducted in the visible wavelength spectrum instead of near infrared (NIR) range. Thus, this thesis aims to determine the anisotropic complex refractive index of graphene oxide (GO) at 1550 nm using optical chip-based device. We propose a planarized optical waveguide structure that facilitates strong polarization dependent light interaction. The light propagation characteristic in thin film coated planarized optical waveguide is firstly studied. Using Finite Element Method (FEM), the optical response of planarized optical waveguide coated with thin film overlays with different refractive indices is obtained. The effective index, n_{eff} of optical waveguide increases with larger refractive index of the thin film overlay but decreases when its extinction coefficient is increased. The effective extinction coefficient, k_{eff} of the thin film coated increases when both the real and imaginary part of the thin film increases. It is found that TE-mode has stronger interaction with thin film overlay as compared to TM-mode, giving the capability of determining the optical constant of the thin film overlay by cross-referencing the experimental and numerical results. Following the completion of simulation work, experiment measuring

the propagation loss-to-coating thickness profile of GO-coated planarized optical waveguide is carried out. GO films with sub-micron thickness (0.1 μm to 1.0 μm) were successfully produced using drop-casting technique. As predicted by simulation, the GO-coated waveguide exhibits large polarization dependent loss which depends strongly on the coating thickness. By cross-referencing the experimental and simulation results, the GO film's complex refractive indices of 1.66+0.17*i* and 1.615+0.002*i* for TE- and TM-polarized light, respectively, are obtained. The uncertainties for the real part of refractive index are 0.03 and 0.020 for TE- and TM-polarized light respectively, whereas the uncertainties for the imaginary part of refractive index are 0.01 and 0.001 for TE- and TM-polarized light, respectively. The results obtained will be valuable in advancing the research and development of GO photonics, especially in the development of optical telecommunication devices where NIR wavelengths are used as information carrier.

Keywords: Graphene oxide, complex refractive index, planarized optical waveguide.

KAJIAN INDEKS BIASAN KOMPLEKS GRAFIN OKSIDA MENGGUNAKAN TINDAK BALAS PENGUTUBAN PEMANDU GELOMBONG PLANAR BERSALUT GRAFIN OKSIDA

ABSTRAK

Disebabkan satu lapisan karbon tunggal yang juga dikenali sebagai grafin telah berjaya dikupas dari grafit 3D, penyelidikan yang mendalam tentang grafin dan derivatifnya dimulakan. Antara semuanya, grafin oksida (GO) dianggap sebagai salah satu calon yang paling menonjol dalam kategori derivatif grafin untuk penggunaan elektronik, optoelektronik dan fotonik. Walaupun GO telah digunakan dalam banyak aplikasi seperti penyerap tepu untuk laser Q-switch dan optik penghalang untuk perlindungan mata, sifat optik asalnya: indeks biasan kompleks yang dilaporkan setakat ini masih dalam percanggahan. Selain itu, kebanyakan penyelidikan perincian optik pada GO dijalankan dalam spektrum panjang gelombang terlihat dan bukannya rangkaian infra-merah-dekat (NIR). Oleh itu, tesis ini bertujuan untuk menentukan indeks bias kompleks anisotropik grafin oksida (GO) pada 1550 nm menggunakan peranti berasaskan cip optik. Kami mencadangkan pemandu gelombang optik planar yang memudahkan interaksi cahaya yang kuat bergantung kepada polarisasi. Ciri penyebaran cahaya dalam filem nipis bersalut pemandu gelombang optik planar telah dikaji. Menggunakan Kaedah Elemen Finite (FEM), tindak balas optik pemandu gelombang optik planar yang tersalut lapisan filem nipis yang dilapisi dengan indeks biasan berbeza telah diperolehi. Indeks efektif, n_{eff} pemandu gelombong optik meningkat dengan indeks biasan filem nipis yang lebih besar tetapi berkurang apabila pekali kepupusan meningkat. Sebaliknya, pekali kepupusan efektif, k_{eff} filem nipis meningkat apabila kedua-dua bahagian sebenar dan khayalan filem nipis meningkat. Didapati bahawa mod-TE mempunyai interaksi yang lebih kuat dengan lapisan filem nipis berbanding mod-TM, memberikan keupayaan untuk menentukan pemalar optik lapisan filem nipis dengan merujuk keputusan ujikaji dan

keputusan berangka. Mengikut kerja simulasi yang telah lengkap, satu ujikaji pengukuran profil kehilangan penyebaran-ke-ketebalan salutan GO pemandu gelombang planar telah dijalankan. Filem GO dengan ketebalan sub-mikron (0.1 μm hingga 1.0 μm) berjaya dihasilkan menggunakan teknik drop-casting. Mengikut ramalan simulasi, pemandu gelombang bersalut GO menunjukkan kehilangan-kebergantungan polarisasi yang besar bergantung kepada ketebalan salutan. Merujuk keputusan ujikaji dan simulasi, indeks biasan kompleks filem GO adalah 1.66+0.17i untuk mod-TE dan 1.615+0.002i untuk mod-TM. Ketidakpastian bagi bahagian sebenar indeks biasan adalah 0.03 bagi mod-TE dan 0.020 bagi mod-TM, manakala ketidakpastian bagi bahagian khayalan indeks biasan adalah 0.01 untuk mod-TE dan 0.001 untuk mod-TM. Hasil kajian tersebut akan berharga dalam memajukan penyelidikan dan pengembangan fotonik GO, terutamanya dalam pengembangan alat telekomunikasi optik dengan menggunakan panjang gelombang NIR sebagai pembawa maklumat.

Kata kunci: Grafin oksida, indeks bias kompleks, pemandu gelombang optik planar

ACKNOWLEDGEMENTS

Foremost, I would like to express my sincere gratitude to my advisor Datuk Prof. Dr. Harith Ahmad for providing me the opportunity to conduct research in Photonics Research Centre, University of Malaya. Also, I would like to show special gratitude to my Co-supervisor Dr. Chong Wu Yi for supervising and guiding my work throughout the Master Program. His guidance helped me in all the time of research and writing of this thesis. I could not have imagined having a better advisor and mentor for my Master study. Besides, I would like to thank my lab mates: Chong Wen Sin, Lai Choon Kong, Ng Kok Bin, Chew Jing Wen and Nur Afiqah binti Mohd Ariffin for all their precious idea and discussion. The brainstorming session with them is very satisfying. On the other hand, I would like to thank Grant RP029C-15AFR, LR001-2014B and FP111-2019A for providing me financial support during the study. Lastly, my parents and girlfriend for their unconditional support and understanding.

TABLE OF CONTENTS

LIST OF FIGURES

LIST OF TABLES

LIST OF SYMBOLS & ABBREVATIONS

ψ	:	Arctangent of Amplitude Ratio upon Reflection
ω	:	Angular Frequency of Electromagnetic Wave
θ_{in}	:	Acceptance Angle
$\tilde{\sigma}$	:	AC Conductivity
α	:	Absorption Coefficient
V_D	:	Abbe Number
λ_c	:	Cut-off Wavelength
$\widetilde{\varepsilon_r}$	:	Complex Relative Permittivity
$\tilde{n}$	:	Complex Refractive Index
α_0	:	Critical Propagation Angle
n_{eff}	:	Effective Index
k_{eff}	:	Effective Extinction Coefficient
k	:	Imaginary Part of Refractive Index
ε_2	:	Imaginary Part of Complex Relative Permittivity
Δ	:	Phase Difference
ω_p	:	Plasma Frequency
n	:	Real Part of Refractive Index
n_D	:	Refractive Index at The Orange Fraunhofer D-line (589.2 nm)
n_F	:	Refractive Index at The Orange Fraunhofer F-line (486.1 nm)
n_C	:	Refractive Index at The Orange Fraunhofer C-line (656.3 nm)
ε_1	:	Real Part of Complex Relative Permittivity
r_s	:	Reflection Coefficient of s-polarized light

r_p	:	Reflection Coefficient of p-polarized light
n_c	:	Refractive Index of Core
n_{clad}	:	Refractive Index of Cladding
Δ_0	:	Refractive Index Difference Between Core and Cladding
c	:	Speed of Light
Z_0	:	Vacuum Impedance of Free Space
k_0	:	Wave Vector of Electromagnetic Wave
λ	:	Wavelength of Electromagnetic Wave
AWG	:	Array Waveguide Grating
CNT	:	Carbon Nanotube
CVD	:	Chemical Vapor Deposition
DMF	:	Dimethylformamide
EM	:	Electromagnetic
E	:	Electric Field
FEM	:	Finite Element Method
FESEM	:	Field-emission Scanning Electron Microscopy
FHD	:	Flame Hydrolysis Deposition
FBG	:	Fiber Bragg Grating
GO	:	Graphene Oxide
GD	:	Germanium-doped
ITO	:	Indium Tin Oxide
H	:	Magnetic Field
NA	:	Numerical Aperture
NIR	:	Near Infrared
PER	:	Polarization Extinction Ratio
PEG	:	Polyethylene Glycol

PLC	:	Planar Lightwave Circuit
rGO	:	Reduced Graphene Oxide
SWCNT	:	Single-walled Carbon Nanotube
SA	:	Saturable Absorber
THz-TDS	:	Terahertz Time-domain Spectroscopy
TE	:	Transverse Electric
TM	:	Transverse Magnetic
TIR	:	Total Internal Reflection
UV	:	Ultraviolet
V	:	V-number
XPS	:	X-ray Photoelectron Spectroscopy

CHAPTER 1: INTRODUCTION

1.1 Graphene

On 5th October 2010, Andre Konstantin Geim and Konstantin Sergeevich Novoselov were awarded the 2010 Novel Prize in Physics by The Royal Swedish Academy of Sciences for their pioneering research on graphene (Organization, 2010). Their achievements were built upon the first demonstration of single layer graphene film isolation using mechanical exfoliation - by means of repeatedly peeling off the layers of a bulk graphite using adhesive tape, and then transferred it onto a silicon dioxide substrate (Novoselov et al., 2004). Graphene is a single atomic layer thick carbon film exfoliated from the 3-dimensional bulk graphite. Its sp^2-hybridised carbon atoms form a 2-dimensional honeycomb-like structure. The realization of graphene immediately generated intense research interests in the scientific communities. Its remarkable properties, which include extremely large theoretical specific surface area of 2630 m^2g^{-1}, very high thermal conductivity, tensile strength which is two orders of magnitude larger than steel, zero bandgap at room temperature which resulted in ballistic conduction of electrons, have all resulted in graphene being termed a "wonder material" which finds many potential applications for aerospace, flexible electronics, and plasmonics (Grigorenko et al., 2012; Li & Kaner, 2008; Matthias Vaupel; Schwierz, 2010; Siochi, 2014). The zero bandgap and high intrinsic electron mobility, together with the single layer optical transmittance of approximately 97.7% across a broad frequency range also attracted interests from the photonics research community (Bao & Loh, 2012; Bonaccorso et al., 2010; Zhu et al., 2010). Particularly, one atomic layer thick graphene layer has been used as saturable absorbers in mode-locked lasers to generate ultrashort pulses with pulse width ranging from 174 fs to 756 fs (Bao et al., 2009; Popa et al., 2010; Sun et al., 2010; Zhang et al., 2009a; Zhang et al., 2010a; Zhang et al., 2009b; Zhao et al., 2010). A waveguide integrated electro-absorption modulator also can be made based on monolayer

graphene (Liu et al., 2011). An all-optical modulator with modulation depth of 38% and a response time of ~2.2 ps can be achieved using graphene as the cladding for a microfiber (Li et al., 2014). In Terahertz (THz) research, a monolithically integrated graphene modulator can be produced to modulate the intensity of THz radiation with 100% modulation depth (Liang et al., 2015). Graphene also act as an active element in photodetectors. Its excellent electrical and optical properties such as high carrier mobility, high surface to volume ratio and ~2.3% of single atomic layer light absorption has rendered it to be an outstanding choice in the realization of ultra-broadband photodetector (Avouris, 2010).

Graphene can be produced using a number of synthesis methods, which include mechanical exfoliation (Novoselov et al., 2004), chemical vapor deposition (CVD) (Kim et al., 2009) and solution exfoliation (Behabtu et al., 2010). Both mechanical exfoliation and CVD are able to produce very high quality graphene. However, both methods necessitate physical transfer of the high quality graphene sheet from bulk graphite or deposited on copper substrate, respectively, to the target surface. The transfer will inevitably introduce discontinuity and defects on the final graphene coating. These imperfections will deteriorate the performance of the fabricated graphene based devices and presents difficulties in large area coating. On the other hand, solution exfoliation of graphene can be achieved by dispersing pristine graphite in chlorosulponic acid. However, the dispersion quality highly depends on the acid strength, and the solubility of graphene decreased markedly when the acidity is lowered to below 80% chlorosulphonic acid (Behabtu et al., 2010). It is worth noting that, without sonication, the solubility of graphene in organic solvent such as N-Methyl-2-pyrrolidone (NMP) is negligible. These issues, together with the high cost of production in large volume, limited bandgap

tunability and low solubility in most solvents have created a huge barriers toward the development and larger scale implementation of graphene-based devices.

1.2 Graphene Oxide: From Precursor to Functional Element

An alternative route to large volume graphene coating is through using graphene oxide (GO) as intermediate precursor (Pei & Cheng, 2012). This route shows the highest potential to mass production of pristine graphene. GO can be produced using the relatively simple and flexible chemical process known as Hummer's method (Hummers & Offeman, 1958). Due to its hydrophilicity compared to graphene, GO can be dispersed very well in most polar solvents, including water. GO solution can then be coated over a larger surface area using solution coating techniques and then be reduced to graphene using thermal, chemical or optical approaches (Becerril et al., 2008; Kumar et al., 2011; Tran et al., 2015). More recently, GO has garnered considerable research interests of its own, not only because of its similar characteristics to graphene, but also due to its own unique characteristics. For examples, GO film is only permeable by water, and not by even the smallest gas molecules like hydrogen and helium (Nair et al., 2012). Furthermore, although GO is considered a dielectric material, its conductivity can be increased by reducing it to reduced GO (rGO) or graphene (Pei et al., 2010).

GO is a material consists of graphene sheets bonded with oxygen functional groups such as hydroxyl, carbonyl, carboxyl and epoxide groups (Lerf et al., 1998). The existence of these oxygen functional groups is the origin of its hydrophilicity that makes GO highly dispersive in water and other polar solvents. The asymmetrical shapes of individual GO flakes allow orderly stacked GO thin films to be produced via layer-by-layer self-assembly using a simple solution coating method (Sun et al., 2013). This method provides

an easy and practical way to perform uniform coating of ultrathin GO films onto a large area (Venugopal et al., 2012). These characteristics have resulted in GO being used as the functional material in various applications.

1.3 Graphene Oxide Structure

Though the synthesis of GO has been demonstrated by Benjamin C. Brodie as early as 1859 and later improved by Hummers and Offeman in 1957, the actual chemical structures of GO has yet to be determined due to its complex non-stoichiometric nature. A number of models have been proposed and are shown in Figure 1.1. Initially, Hofmann and Holst model states that an oxygen atom is bounded to two carbon atoms on the hexagon plane to form epoxy group (Hofmann & Holst, 1939). Later, the Ruess model proposed a wrinkled carbon layer which consists of cyclohexane-chairs of hydroxyl and ether oxygen groups (Ruess, 1947). This model was later revised by Scholz and Boehm, where the ether oxygen group was replaced by corrugated carbon sheet composed of ribbons with quinoidal structure (Scholz & Boehm, 1969). Mermoux et al. (Mermoux et al., 1991) proposed an alternative to the Reuss model by introducing a poly-carbon monofluoride structure, $(CF)_n$, while Nakajima et al. (Nakajima et al., 1988; Nakajima & Matsuo, 1994) proposed a level-2 type $(C_2F)_n$ model. In 1998, these models were superseded by that proposed by Lerf et al. (Lerf et al., 1998), which portray a GO sheet as random arrangement of aromatic sections with unoxidized benzene rings and alicyclic rings attaching C-OH, C=C, ether groups, with its edges terminated by hydroxyl and carboxylic groups.

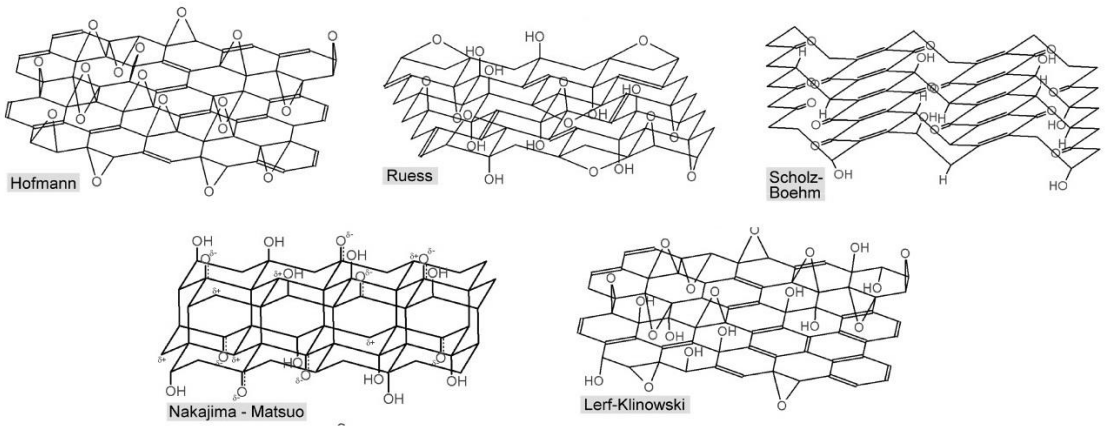

Figure 1.1: The proposed chemical structure of GO (Inagaki & Kang, 2014).

1.4 Electrical Properties of Graphene Oxide

GO can be considered as an insulator due to disruption of the sp^2 network by oxygen functional groups within the GO sheet. As a result, GO is not initially considered as a functional material for electronics applications. However, by using a variety of reduction techniques such as thermal, chemical, electrochemical or optical approaches, GO can be transformed into semiconductor or semimetal through the restoration of sp^2 graphitic bonding structure. The electrical conductivity of GO was increased from 4.2×10^{-6} S.cm^{-1} to ~210 S.cm^{-1} after thermal annealing at 1100 ^{o}C, with significant increase in carbon-to-oxygen atomic ratio from 2.17 (GO) to 23.7 (rGO) after the thermal treatment (Tran et al., 2015). From other reports, GO sheets with initial sheet resistance of ~1.0×10^{11} Ω/sq was reduced to ~1.0×10^{8}, ~1.0×10^{5} and ~1.0×10^{4} Ω/sq via pure chemical reduction (hydrazine), thermal-aided chemical reduction (hydrazine + 400 ^{o}C) and pure thermal annealing reduction (1100 ^{o}C), respectively (Wang et al., 2010). Besides, chemically modified GO film also exhibits up to 90% transmittance at 550 nm, making it a promising candidate as transparent electrodes (Becerril et al., 2008).

The mechanisms of electrical conduction of GO and rGO sheets can be explained as follows. The delocalization of free carriers in GO or rGO films are often being blocked or trapped by the sp^3 cluster within the graphene layer, thus restricting the carrier mobility and hence conductivity of GO or rGO films. The correlation between electrical conductivity and sp^2 domain fraction in rGO film was investigated in (Mattevi et al., 2009). The extrapolation of electrical conductivity of thermally reduced GO film against the sp^2 carbon fraction, as characterized by X-ray photoelectron spectroscopy (XPS) is shown in Figure 1.2. There are two types of electrical conduction mechanisms in GO, which are the tunneling/hopping and percolation of free carriers. As-synthesized GO film only has a very small fraction of sp^2 cluster. Therefore, the transportation of carriers relies on tunneling/hopping mechanism, which is not efficient. However, once the sp^2 fraction in GO film exceeded the "percolation threshold" (0.6 fraction of sp^2 domain), the interconnectivity of sp^2 domains increases, therefore enabling percolation of free carriers among the sp^2 clusters and lead to the significant improvement of electrical conductivity. The structure of GO at different level of reduction is shown in Figure 1.3. It's worth noting that electrical conduction through GO structures in Figure 1.3 (a) and (b) depends on the tunneling/hopping mechanism, whereas electrical conduction of GO structures in Figure 1.3 (c) and (d) is determined by the percolation of free carriers. It is important to understand how the chemical structure of GO changes during the reduction process as the free carriers from sp^2 domain can affect its intrinsic optical properties.

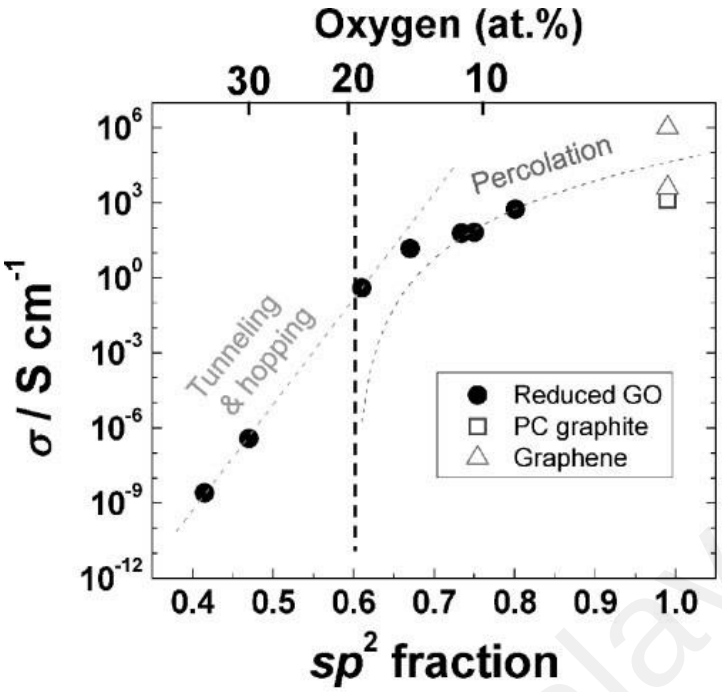

Figure 1.2: Extrapolation of electrical conductivity of thermally reduced GO film against the sp^2 carbon fraction characterized by XPS (Mattevi et al., 2009).

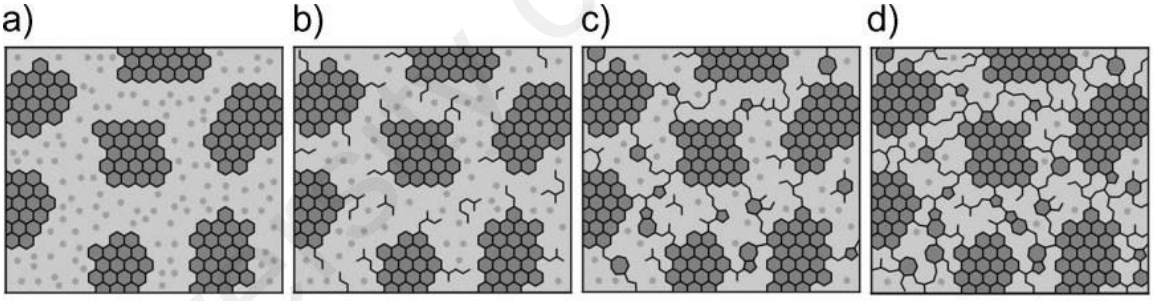

Figure 1.3: Structure of GO at different level of thermal reduction: a) room temperature, b) ~100 ^{o}C, c) ~220 ^{o}C, d) ~500 ^{o}C. Dark grey and light grey areas represents sp^2 and sp^3 cluster respectively (Mattevi et al., 2009).

1.5 Optical Properties of Graphene Oxide

The absorption spectral edge of GO falls in the ultraviolet (UV) region, which is attributed to the π-π∗ and n-π∗ electronic transitions. The *p*-orbital of carbon in GO can either be jointed in phase (π-bond) or out of phase (π∗-bond) as shown in Figure 1.4, where the π-orbital is in a lower energy state compared to π∗-orbital, granting photon

induced transitions from the π-orbital to π∗-orbital. Besides, due to the ketonic structure of GO, it will also allow a second electronic transition called the n-π∗ transition, which is attributed to the excitation of electron from non-bonding n-orbital to the π∗-orbital. On the energy scale, the π-π∗ transition is more energetic than the n-π∗ transition, which corresponds to shorter wavelength absorption from the π-π∗ transition.

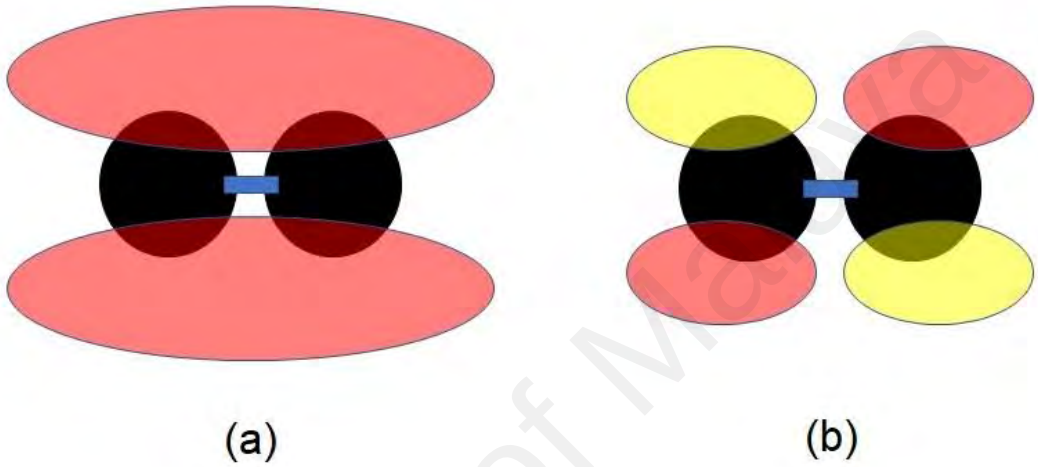

Figure 1.4: The p orbital of two carbon joint (a) in-phase and (b) out-of-phase.

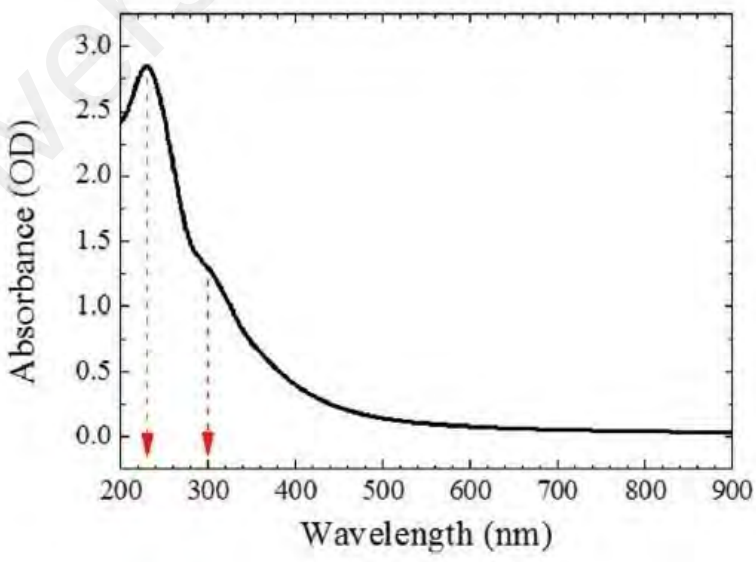

Figure 1.5: UV-Vis absorption spectrum of GO suspension in a cuvette (Shang et al., 2012).

Figure 1.5 shows the UV-Vis spectra of water dispersed GO suspension in a 2 mm cuvette. There is a main absorption peak at around 231 nm and another shoulder absorption peak at 303 nm, which correspond to the π-π∗ and n-π∗ transitions, respectively (Shang et al., 2012). The difference in the absorption peak intensities between these two transitions can be explained by the higher molar absorptivity for the π-π∗ transition as compared to the n-π∗ (Ingle & Crouch, 1988). The absorption peak at ~300 nm is contributed by the carbonyl group in the GO molecules. Results obtained from X-ray photoelectron spectroscopy (XPS) show that there are four main oxygen functional groups present in the GO samples. The dominant groups are epoxy and hydroxyl (-OH), followed by a smaller constitution of carboxyl and carbonyl groups (Li et al., 2012; Tran et al., 2011). With such correlation between absorption spectra and oxygen-functional groups, one can employ the absorption characteristic of GO to monitor the changes in composition of a GO sample. For example, once the GO transforms into reduced graphene oxide (rGO) through hydrazine reduction, the absorption peak at 231 nm will be shifted to 267 nm, which represents the restoration of conjugated C=C bonds (Zhang et al., 2010b). Besides, the absorption feature at ~300 nm which corresponds to n-π∗ transition also decreases intensity after the reduction process via acid-aided dehydration of GO (Chen & Yan, 2010).

The delocalized π carriers from the sp^2 domain are the primary source of optical non-linearities in graphene and its derivatives (De La Torre et al., 2004). GO, which possesses a highly tunable energy bandgap compared to graphene, is a relatively better candidate for nonlinear optical applications (Omidvar et al., 2016). The chemistry structure of GO - two dimensional nature enriched with oxygen functional groups - allows it to be readily hybridized with other nonlinear optical materials, nanoparticles and dyes to form composite with enhanced nonlinearity (Omidvar et al., 2018). Furthermore, according to

Liu et al., the nonlinear absorption of GO shows distinct response as compared to its allotrope: carbon nanotubes (CNT) and fullerenes (Liu et al., 2009b). For GO, the nonlinear absorption in the nanosecond regime is more complicated because of the participation of more excited state transitions. Thus, excited state absorption (ESA) will be dominant in the nanosecond time scale. For nonlinear absorption of GO in picosecond regime, two photon absorption is dominant as it is under non-resonant excitation. On the other hand, C_{60} has large singlet and triplet ESA cross sections which leads to strong ESA for both nano- and picosecond pulses. Single-walled CNT has the strongest limiting action in nanosecond regime but poorest in picosecond time scale due to strong nonlinear scattering happens in nanosecond regime. The nonlinear absorption magnitude for GO is also different from its carbon nanotube and fullerene allotropes, as shown by the comparison of open aperture Z-scan measurement results in Figure 1.6. Besides, GO shows in situ third-order nonlinearity during laser reduction process. The negative nonlinear refractive index variation is found to be as large as 10^{-9} cm^2/W, while the nonlinear absorption coefficient is found to be 40000 cm/GW (Zheng et al., 2014). Enhancement of four wave mixing conversion efficiencies by ~9.5 dB is observed in doped silica waveguides integrated with 2 layers of GO coating, which is attributed to the high Kerr nonlinearity of GO (Yang et al., 2018).

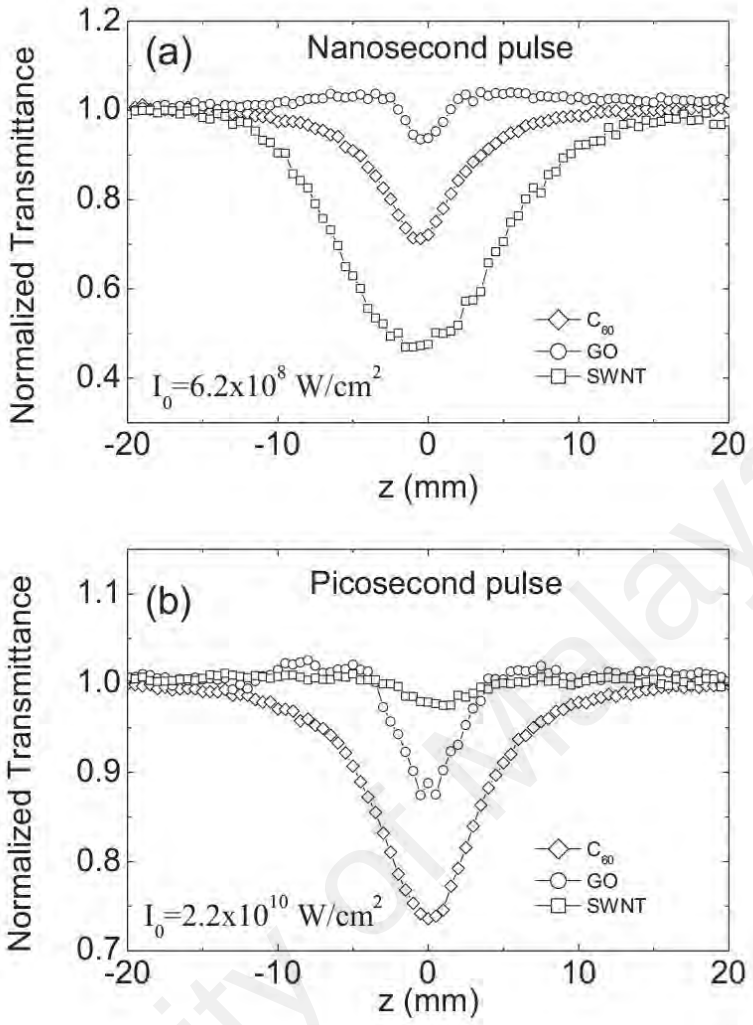

Figure 1.6: The open aperture Z-scan measurement of SWCNT in DMF solution, C_{60} in toluene and GO in (a) nanoseconds and (b) picoseconds regime (Liu et al., 2009b).

1.6 Applications of Graphene Oxide

GO can be used to produce high sensitivity and large bandwidth photodetectors (Chitara et al., 2011; Zhan et al., 2012), attributed to its highly tunable electrical and optical properties to make bandgap tuning possible. The bandgap for GO is approximately 3.5 eV while the bandgap of reduced GO (rGO) can be tuned from 1.0 eV to 1.6 eV by varying the fraction of the oxygen functional group (Liang, 2014; Mathkar et al., 2012). It can simultaneously slow down the recombination time of the carrier and increase the absorption efficiency as compared to graphene. A temperature dependent broadband

photodetector can be made by self-standing rGO film with both ends of the film coated with silver electrodes (Sehrawat et al., 2018).

On the other hand, the observation of tunable fluorescence between ultraviolet (UV) and mid infrared range of the electromagnetic spectrum from GO/rGO with remarkable quantum efficiency (Tung et al., 2009) has opened up a variety of optical applications (Pan et al., 2010; Sun et al., 2008). The versatile optical characteristic of GO is utilized in several biomedical applications, especially for delivery of drug and cellular imaging (Liu et al., 2008; Sun et al., 2008). Dai et al. has successfully synthesize nano-size GO sheets functionalized with polyethylene glycol (PEG) to do live cell imaging (Liu et al., 2008). The use of hydrophilic PEG enhances the solubility of PEGylated GO in water, which allows it to readily form complex with a hydrophobic antineoplastic drug SN38 through Van der Waals bonding. This GO-PEG-SN38 complex can maintain the high potency of SN38 while having high aqueous solubility at the same time. Besides, PEGylated GO can form covalent conjugation with B-cell specific antibody, Rituxan (anti-CD20) and selectively bind to B-cell lymphoma cells but not to negative CEM T-cells. The strong NIR photoluminescence of PEGylated GO attached on B-cell lymphoma cells is observed but not on T-cells, which confirms the selective binding behavior of PEGylated GO. Furthermore, PEGylated nano GO sheet also exhibits high absorption in the near-infrared (NIR) wavelength, thus it can be used for high efficient in-vivo tumor photothermal therapy by irradiating low power NIR laser without inducing any observable cytotoxicity to the mice (Yang et al., 2010). These research findings suggest that GO is a promising material in biomedical applications like cancer therapy.

In addition, one of the important applications of optical nonlinearity is optical limiting, which can limit the transmission of intense light for eye protection. Chen et al. show that the optical limiting performance of GO can be enhanced by linking it to nonlinear optical molecules like fullerene C_{60} and porphyrin (TPP) (Liu et al., 2009a). Another application that utilize the nonlinear absorption characteristic of nonlinear optical material is the saturable absorber for ultrafast pulsed laser. Jia Xu et al. has demonstrated a mode-locked erbium-doped fiber laser with 200 fs pulse width and 22.9 MHz repetition rate using GO as saturable absorber (SA) (Xu et al., 2012). Sobon et al. has also demonstrated comprehensive studies on GO and rGO as SA for mode-locking erbium-doped fiber laser (Sobon et al., 2012). They found out that there is no significant difference in laser performance for GO and rGO based SA, both of them also can produce stable mode-locking soliton pulses with 400 fs pulse width and more than 9 nm bandwidth (1560 nm at center). This observation may be due to the negligible effect of the presence of sp^3 hybridized carbons in the lattice on the nonlinear optical properties of GO and rGO.

Last but not least, GO can also be integrated with optical waveguide to perform various functions. The optical characteristic of GO is exploited to design and produce an all optical waveguide humidity sensor, where GO with water-altering dielectric properties is coated on SU8 polymer waveguide to act as sensing material (Lim et al., 2014a). In addition, a waveguide polarizer with nearly 40 dB polarization extinction ratio (PER) was demonstrated by coating GO bulk film of 2.0 μm thickness and 1.3 mm length on a polymer waveguide. The large PER was attributed to the orderly-stacked GO multilayer structure, which results in the large anisotropic complex dielectric function of GO (Lim et al., 2014b). An all optical GO-coated waveguide modulator with modulation efficiency of 72% has also been demonstrated by utilizing the reversible photo-induced thermal reduction behavior of GO (Chong et al., 2016). Besides, Wu et al. also experimentally

demonstrated an integrated waveguide polarizer and polarization selective micro-ring resonator (MRR) coated with GO films (Wu et al., 2019). A high polarization dependent loss of nearly 53.8 dB is obtained for the straight channel waveguide, while the GO-coated MRR yield a PER of approximately 8.3 dB between TE- and TM-resonance.

1.7 Refractive Index of Graphene Oxide Thin Film

Most if not all of optical applications above can be explained using the refractive index of GO thin film. However, despite all the extraordinary demonstrations made using GO as functional material, the precise value of complex refractive index of GO thin film has yet to be established. Reports on the measurement of GO complex refractive index to date showed large deviations. At 600 nm, the real part of complex refractive index of GO were reported to have values ranging from 1.9 to 2.0, while its imaginary part is in the range of 0.1 to 0.3 (Jung et al., 2007; Jung et al., 2008; Shen et al., 2011). At 1550 nm, the reported complex refractive index of GO showed an even larger uncertainty, ranging from 1.5 to 2.1 and 0.01 to 0.25 for the real and imaginary parts, respectively (Kravets et al., 2015; Schöche et al., 2017). In addition, only reports by (Schöche et al., 2017) considers the anisotropic complex refractive indices of GO in their studies. The omission of polarization dependent optical response of GO (which have been proven to be significant) in most studies creates a gap in the efforts to truly understand the underlying principles of GO-functionalized optical devices in order to optimize their performances. Therefore, the intrinsic optical properties of GO, especially in the NIR wavelength range, require a more comprehensive study and understanding.

1.8 Motivation

The response of optical material to electromagnetic (EM) wave has always been the most crucial information in the design of new optical devices. Also, the present optical fiber communication technology (Jones, 1987) is constructed based on the 1550 nm wavelength range, which results in a large demand of various optical components that operate in this wavelength range. As a new optical functional material, understanding of the optical response of GO thin film in the 1550 nm wavelength range is important. It would very much hinder the development of GO-based optical devices used in the fiber communication system if the optical properties of GO in NIR region is not fully understood. From previous report by Lim et al. (Lim et al., 2014b), GO-coated planar waveguides exhibit very large polarisation response to light in the 1550 nm wavelength range. By designing a suitable planar waveguide structure, the light field distribution of the waveguide coated with GO thin film overlay can be rigorously studied. The understanding of this distribution and the resulting large polarisation response can then be used as useful information to determine the anisotropic complex refractive index of GO thin film.

1.9 Thesis Objectives and Outlines

This project aims to investigate the optical properties of GO in the NIR wavelengths. The complex refractive index of GO will be determined using polarization response of GO-coated planarized optical waveguide. The objectives of this work are:

1. To study the light propagation characteristics of planarized optical waveguide coated with thin films of different complex refractive indices at the 1550 nm optical fiber communication window.
2. To fabricate GO-coated planarized optical waveguide and measure its polarization response.
3. To determine the anisotropic complex refractive index of GO at 1550 nm by analyzing the polarization response of GO-coated planarized optical waveguide.

The outline of this thesis are as follows:

Literature about the various optical characterization technique on determining the complex refractive index of GO at visible and NIR wavelength range will be discussed in Chapter 2. Chapter 2 will also provide an introduction of waveguide theory and simulation model which is important in fulfilling the objectives of this work. Subsequently, Chapter 3 presents the simulation results of the optical properties of thin film coated planarized optical waveguide, namely the effective mode index of the thin film coated optical waveguide. Then, Chapter 4 describes the fabrication of thickness varied (from zero up to 1.0 μm) GO-coated planarized optical waveguide, followed by the measurement of its distinct polarization response. By analyzing the experimental polarization response and cross-referencing with the simulation results, the anisotropic complex refractive index of GO at 1550 nm is determined in the last section of this chapter. Finally, the outcomes of this thesis are concluded in Chapter 5.

CHAPTER 2: LITERATURE REVIEW

2.1 Complex refractive index

When a light passes through a slab of optical material at an angle, a number of interesting phenomena would occur. Firstly, a portion of the light will be reflected from the first surface of the slab with the remaining portion being refracted into the slab. Within the slab, a portion of the refracted light will be absorbed by the medium. Finally, the remaining portion of light reaches the second surface of the slab and undergo both a second reflection and refraction out of the slab. These observations described above summarize a few basic optical interactions between light and matter, namely reflection, refraction, and absorption. By utilizing the interaction between light and matter, certain optical material can be integrated or directly fabricated into various optical functional devices such as prism, mirrors, optical lenses, polarizers and modulators so that they can disperse, reflect, refract, polarize and modulate light, respectively.

The optical phenomena mentioned above is governed by the complex refractive index of an optical material, $\tilde{n}$, shown in eqn. (2.1),

$$\tilde{n} = n + ik \tag{2.1}$$

Reflection and refraction of light at an interface are determined by the real part of complex refractive index, n, as governed by the Fresnel Equations and Snell's Law, respectively. Whereas the absorption of light by an optical material is determined by the imaginary part of complex refractive index, k, which is correlated with the absorption coefficient, α of the optical medium, as governed by Beer-Lambert law. In order to describe the relationship between the k and α, we have to consider a plane electromagnetic (EM) wave propagating through a medium with certain complex refractive index, as shown in eqn. (2.2),

$$E(z,t) = E_0 e^{i(k_0 z - \omega t)} \tag{2.2}$$

where z is the propagating direction of the EM wave, k_0 is the wave vector of the EM wave, E_0 is the electric field amplitude of the EM wave at $z = 0$. The wavelength of the EM wave, λ will be reduced by a factor of n, as compared to free space. Therefore, k_0 can be expressed as eqn. (2.3) below,

$$k_0 = \frac{2\pi}{(\lambda/n)} = \frac{n\omega}{c} \tag{2.3}$$

where λ is the wavelength of the EM wave, ω is the angular frequency of the EM wave, c is the speed of light in vacuum and n is the real part of complex refractive index of the optical medium. When the imaginary part of complex refractive index is also considered, eqn. (2.3) is transformed into eqn. (2.4),

$$k_0 = \frac{\tilde{n}\omega}{c} = (n + ik)\frac{\omega}{c} \tag{2.4}$$

By substituting eqn. (2.4) into eqn. (2.2), we will obtain a more complete spatial and time dependence electric field expression, as shown in eqn. (2.5),

$$\begin{aligned} E(z,t) &= E_0 e^{i\left(\frac{\tilde{n}\omega z}{c} - \omega t\right)} \\ &= E_0 e^{-\frac{k\omega z}{c}} e^{i\left(\frac{n\omega z}{c} - \omega t\right)} \end{aligned} \tag{2.5}$$

Eqn. (2.5) shows that any optical medium having a non-zero k will lead to an exponential decay of the EM wave propagating inside that medium. At the same time, the real part of complex refractive index, n determines the phase velocity of the EM wave. Since the intensity of the EM wave is directly proportional to the square of its amplitude, $I \propto EE^*$, it can be deduced that the intensity of the EM wave will also decay exponentially with a constant absorption coefficient, α,

$$\alpha = \frac{2k\omega}{c} = \frac{4\pi k}{\lambda} \tag{2.6}$$

We can relate the refractive index of the medium to its relative permittivity, ε_r as shown in eqn. (2.7). However, if n is complex so does ε_r. Therefore, the complex relative permittivity is defined as eqn. (2.8), where ε_1 and ε_2 are its real part and imaginary part, respectively. By relating both the complex refractive index and complex relative permittivity, eqn. (2.7) can be rewritten as eqn. (2.9),

$$n = \sqrt{\varepsilon_r} \tag{2.7}$$

$$\tilde{\varepsilon}_r = \varepsilon_1 + i\varepsilon_2 \tag{2.8}$$

$$\tilde{n}^2 = \tilde{\varepsilon}_r \tag{2.9}$$

Using the relationship of eqn. (2.9), eqn. (2.1) and eqn. (2.8) can be combined. And by solving for their explicit relation between the real part and imaginary part of complex refractive index and complex relative permittivity, we obtain the following equations,

$$\varepsilon_1 = n^2 - k^2 \tag{2.10}$$

$$\varepsilon_2 = 2nk \tag{2.11}$$

$$n = \frac{1}{\sqrt{2}}\left(\varepsilon_1 + (\varepsilon_1^2 + \varepsilon_2^2)^{\frac{1}{2}}\right)^{\frac{1}{2}} \tag{2.12}$$

$$k = \frac{1}{\sqrt{2}}\left(-\varepsilon_1 + (\varepsilon_1^2 + \varepsilon_2^2)^{\frac{1}{2}}\right)^{\frac{1}{2}} \tag{2.13}$$

These equations show that $\tilde{n}$ and $\tilde{\varepsilon}_r$ are variables that depend on each other. It is worth noting that if the absorption of a medium is weak, the k of the medium can be assumed to be negligible, which in turn simplifies eqn. (2.12) and eqn. (2.13) to eqn. (2.14) and eqn. (2.15),

$$n \approx \sqrt{\varepsilon_1} \tag{2.14}$$

$$k \approx 0 \tag{2.15}$$

Eqn. (2.14) and (2.15) show that the refractive index and extinction coefficient of a material depends on the real part and imaginary part of complex relative permittivity, respectively.

The complex refractive index of an optical material may also vary with the wavelength of light, which is known as dispersion. This implies that the phase velocity of the light propagating in a medium depends on its wavelength. This wavelength dependency is caused by the interaction between light and electron of the medium. In the early stage of lens design, the amount of dispersion of an optical material can be quantified by the Abbe number (introduced by Ernst Abbe) (Volkmann, 1966),

$$V_D = \frac{n_D - 1}{n_F - n_C} \tag{2.16}$$

where n_D is the refractive index at the orange Fraunhofer D-line (589.2 nm), n_F is the refractive index at the blue Fraunhofer F-line (486.1 nm), and n_C is refractive index at the red Fraunhofer C-line (656.3 nm). A large Abbe number indicates low dispersion and vice versa. This value is useful in the design of achromatic optical elements, but in fact it gives only a rough indication. For a more accurate description of wavelength dependency of refractive index, the Cauchy's equation is normally used because of its mathematical simplicity (Langhoff & Karplus, 1969). However, Cauchy's equation is only valid for normal dispersion in the visible spectrum. Its dispersion curve at infrared region deviates from the actual refractive index value, and it also cannot represent anomalous dispersion. Therefore, as a later development of Cauchy's equation, the Sellmeier equation is used instead for a more accurate modelling of dispersion of light in transparent medium (Sellmeier, 1871). The Sellmeier equation covers a much larger wavelength range than Cauchy's equation, which is between 365 nm and 2300 nm. Nevertheless, Cauchy's and Sellmeier equations are only valid for transparent or semi-transparent material, when it

comes to other absorbing material, oscillator theory such as Drude-Lorentz model is used to describe its dispersion relation (Shibayama et al., 2008).

Another important characteristic of electromagnetic wave is the polarization state of light. Light emitted from the sun or a light bulb is usually randomly polarized. Randomly polarized lights can be polarized into a certain oscillating angle using a polarizer or when reflected from a dielectric surface at Brewster's angle. The electric field of light can either be linearly polarized perpendicular (p-polarized) or parallel (s-polarized) to the plane of propagation. However, p- and s-polarized lights cannot be differentiated in an optical fiber due to its symmetric cylindrical structure. For planar optical waveguide, TE-mode and TM-mode is denoted as the electromagnetic wave with electric field polarized parallel and perpendicular to the substrate surface, respectively. Planar optical waveguides with asymmetric structure will have different propagation characteristics for TE- and TM-polarized lights.

To summarize, the complex refractive index provides information about the phase velocity and absorption strength of an optical material and is the essential optical parameter in determining the optical response of that material when interacting with EM wave of different frequencies. Having an accurate value of complex refractive index of an optical material is crucial in the design and development of new photonics devices.

2.2 Optical characterization technique

2.2.1 Introduction

Optical characterization is the approach taken to investigate or manipulate matter by means of light. Some examples of optical characterization techniques include:

- pump-probe spectroscopy that is used to study the relaxation of electrons in a material over time through changes in transmission or reflectivity of the pump-induced sample,
- photoemission spectroscopy which measures the binding energy of electrons in a material via photoelectric effect, and
- Raman spectroscopy which uses laser induced Raman shifts to identify the chemical bonding of molecules.

However, compared to the characterization methods that interpret the electronic state of material, other optical techniques which specifically investigate the linear dispersion of complex refractive index with wavelength of material is the focus of this work. Hence, a comprehensive review of all optical techniques that are used to examine the linear dispersion relation of GO will be presented in the following subsections.

2.2.2 Prism coupler

With regards to refractive index measurement for dielectric thin film, an established method is the prism coupling measurement. The working principle behind prism coupler was first described by L.V. Logansen et al. in 1967 (Iogansen, 1967). Two years later, physicists in the University of Washington and Bell laboratories experimentally demonstrated the first ever refractive index measurement on a thin film using a prism coupler (Harris et al., 1970; Tien et al., 1969). The concept of prism coupler works as

follows (Ulrich & Torge, 1973): collimated laser beam is first projected into a prism. The laser beam in the prism is then coupled into the underlying dielectric thin film, as shown in Figure 2.1. This coupling efficiency is governed by the refractive index of the thin film and the incident angle, θ that the laser beam makes with the normal of the prism-thin film interface.

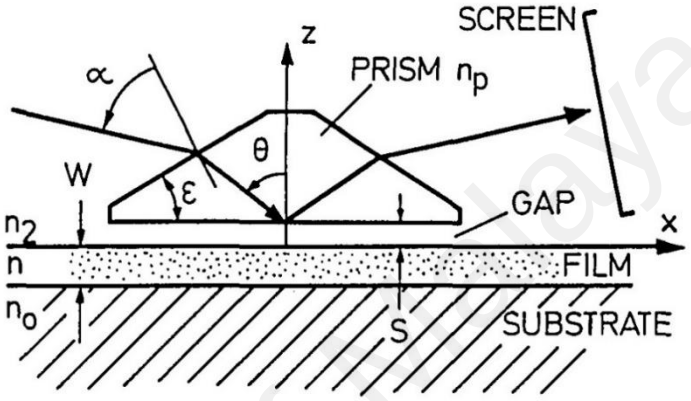

Figure 2.1: Schematic image of prism coupler (Ulrich & Torge, 1973).

The phase velocity of the laser beam in the x-direction depends on the incident angle: $v^{(i)} = c \,/\, n_p \sin\theta$. Strong coupling occurs when $v^{(i)}$ matches with the phase velocity of the propagation mode in the thin film, v_m (m=0,1,2…). Thus, the characteristic mode of propagation can be obtained from the corresponding angles where strong coupling occur, θ_m: $\tilde{N}_m = {}^{c}/_{v_m} = n_p \sin\theta_m$. In addition, the theoretical value for the characteristic propagation mode can be calculated from the dispersion equation of the dielectric thin film as a waveguide: $N_m = N(m, n, W, k, n_0, n_2, \rho)$, where m is the mode number, k is the propagation constant, n_0 and n_2 are the refractive index of the medium sandwiching the thin film, and ρ is the polarization state of laser beam (TE: $\rho = 0$; TM: $\rho = 1$) . All of the parameters in the dispersion equation can be measured separately except *n* (refractive index of thin film) and *W* (thickness of thin film). Computational iteration can be done by adjusting the values of *n* and *W* until the theoretical value of N_m matches with

the experimental value of $\widetilde{N}_m$. As a result, the refractive index and coating thickness of the dielectric thin film can be obtained.

The prism coupler can be considered as a relatively simple and convenient method to characterize a dielectric thin film with high precision, as long as you can experimentally determine the incident angles where the strong couplings occur. However, there are also a few disadvantages in this method that restrict its capability, which are:

(i) The thickness of the film must be large enough to support at least two modes. Otherwise, the results will not be accurate.

(ii) This method requires that the thin film be pressed against the base of the prism. Careless treatment may result in damage to the thin film. In this case, this method is more suitable to examine hard film as compared to soft film.

(iii) High uniformity of the film is required to ensure that no obstruction occurs during the coupling process.

Therefore, prism coupling method is not suitable to be used to characterize sub-micron GO thin film which is relatively "soft" in nature.

2.2.3 Optical Microscopy

Optical microscope can be used to measure the refractive index of a thin film based on the contrast between the reflected beams from substrate and the thin film overlay above. Using this information, one can determine the intrinsic optical properties of the thin film through modeling of multilayer interference (Abergel et al., 2007). However, it is quite difficult to observe the contrast for single layer thin film such as graphene, given that the reflection from the thin film is usually less than 10% of the reflection from the substrate.

Jung et al. successfully overcame this problem by optimizing the substrate to produce extremely high contrast imaging (reflectivity from single layer graphene is 12 times stronger than that from substrate) (Jung et al., 2007). By using this modified confocal microscopy method, they managed to obtain the effective refractive index and optical absorption coefficient of GO and rGO at 488 nm, 543 nm and 633 nm by comparing the theoretically predicted and experimentally measured contrast.

The reflection and transmission of multilayer system in their work is shown in Figure 2.2. There are a total of three interfaces: (i) air and thin film, (ii) thin film and dielectric film and (iii) dielectric film and silicon substrate. The amplitude of the reflection depends on the interference process between the transmitted and reflected light paths between the three interfaces. The interference that occurs between all these light paths will determine the final amplitude of the reflected light beam. The phase shift induced by the thin material (GO) and dielectric thin film are $\delta_2 = d_2(n_2 - ik_2)\cos\frac{2\pi\theta_2}{\lambda}$ and $\delta_3 = d_3(n_3 - ik_3)\cos\frac{2\pi\theta_3}{\lambda}$, respectively. The total amplitude of the reflected light consists of the lights reflected from

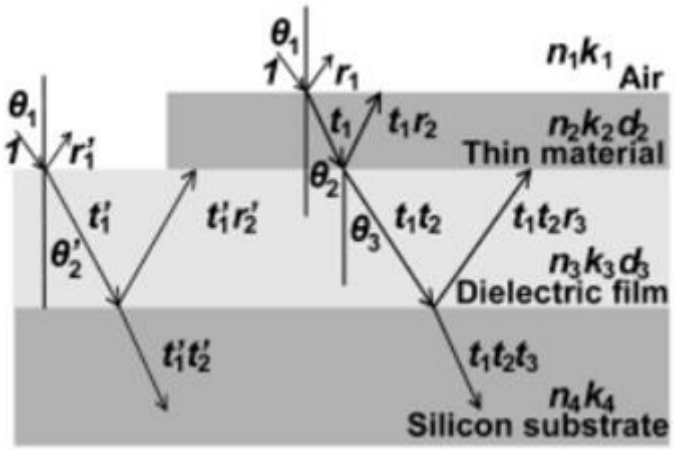

Figure 2.2: Schematic diagram of the multilayer system for confocal microscopy method (Jung et al., 2007).

the interfaces between air and thin film (r_1), thin film and dielectric film (r_2) and dielectric film and silicon substrate (r_3). The reflection from the three layers stacking, $r_{platelet}$ is shown in eqn. (2.17),

$$r_{platelet} = \frac{r_1 + r_2\, exp(-2i\delta_2) + [r_1 r_2 + exp\,(-2i\delta_2)] r_3 exp\,(-2i\delta_3)}{1 + r_1 r_2\, exp(-2i\delta_2) + r_3\, exp(-2i\delta_3)[r_2 + r_1 exp(-2i\delta_2)]} \tag{2.17}$$

However, in the absence of the thin film, the phase change induced by the dielectric film is $\delta'_2 = d_3(n_3 - ik_3)\cos\frac{2\pi\theta_2{}'}{\lambda}$, where the total amplitude of reflected light only consist of the light reflected from the air-dielectric film interface (r'_1) and dielectric film-silicon substrate interface (r'_2). Thus, the reflection from this double layer stacking, $r_{dielectric}$ is shown in eqn. (2.18),

$$r_{dielectric} = \frac{r'_1 + r'_2\, exp(-2i\delta'_2)}{1 + r'_1 r'_2\, exp(-2i\delta'_2)} \tag{2.18}$$

The intensity of the reflected beam can be obtained by multiplying the reflected amplitude with its complex conjugate. Finally, the contrast between the reflected light from GO and the dielectric film is characterized by the Michelson contrast: $contrast = \frac{R_{GO} - R_{dielectric}}{R_{GO} + R_{dielectric}}$, where R_{GO} and $R_{dielectric}$ are the intensity of light reflected from GO and dielectric, respectively. The value of *n* for GO and rGO are determined to be 2.0 and 2.1, whereas the value of *k* are 0.30 and 0.55, at wavelength of 633 nm, respectively. Although this is a non-destructive optical characterization method, but this work only covers the visible spectrum and is not able to determine the anisotropic refractive index of the thin film under test. Therefore, optical information in the NIR wavelength range is still missing.

2.2.4 Spectroscopy ellipsometry

Another well-known and widely used optical technique to determine thin film thickness and complex refractive index is the spectroscopic ellipsometry (Garcia-Caurel

et al., 2013). It is a non-destructive measurement technique. Standard ellipsometry measurement is shown in Figure 2.3. A polarized light is incident upon the thin film sample at an angle. Light reflected from the sample passed through a polarization state analyzer before it reaches the detector. The incident light consists of both s- and p-polarized components, denoted as $E_{in,s}$ and $E_{in,p}$ respectively. Reflection of light from the thin film sample may result in a change in its polarization components. The reflected light of s- and p-polarized components are denoted $E_{out,s}$ and $E_{out,p}$, respectively. The ratio of complex reflection coefficients of s- and p-polarized lights, $r_s = \frac{E_{out,s}}{E_{in,s}}$ and $r_p = \frac{E_{out,p}}{E_{in,p}}$, are then used to determine the values of Δ and ψ, with the relationship shown in eqn. (2.19),

$$\frac{r_s}{r_p} = tan\,\psi \exp(i\Delta) \tag{2.19}$$

where the Δ is the phase difference and ψ equals to $tan^{-1}\left[\frac{|r_s|}{|r_p|}\right]$. By fitting the experimentally measured values of $tan\,\psi$ and Δ using model analysis, the complex refractive index and thickness of the dielectric thin film can be obtained. Cauchy and Sellmier models are often used for describing the index for transparent material. In the case of absorbing material, both the real and imaginary part of the material need to be considered. Therefore, oscillator theories such as Gaussian, Lorentz and Harmonic oscillators are used to describe its dispersion relationship. The idea is to treat atoms and molecules as harmonically bound electrons which is oscillating at a certain resonant frequency, associated with a damping factor. Jung et al. have used imaging spectroscopic ellipsometry to measure the dispersion relation of *n* and *k* for single- and multi-layer GO and rGO films in the wavelength range from 350 nm to 1000 nm (Jung et al., 2008). The results are shown in Figure 2.4. It can be seen that at the wavelength of 600 nm, the value of *n* and *k* for GO is 1.88 and 0.1, respectively. After a thermal treatment, the values of *n*

and *k* increase to 2.4 and 1.0, respectively, indicating reduction of GO to rGO has taken place Besides, Shen et al. also use standard spectroscopic ellipsometry to characterize few layers GO and rGO in the wavelength range from 250 nm to 850 nm (Shen et al., 2011). The ellipsometry parameters obtained are fitted using Lorentz oscillator model, then the values of *n* and *k* of GO and rGO can be calculated. The results are as shown in Figure 2.5. The complex refractive index of GO and rGO at 600 nm are found to be 1.9+0.24*i* and 2.25+0.75*i*, respectively. Also, by analyzing the dielectric function of GO using the same model, the relation between the band-gap energy and proportion of oxygen group to sp^2 carbon domain in GO can be investigated. The results show that the energy bandgap of GO varies from 2.8 eV to 1.8 eV when the fraction of oxygen and hydroxyl groups reduces an amount of 25%.

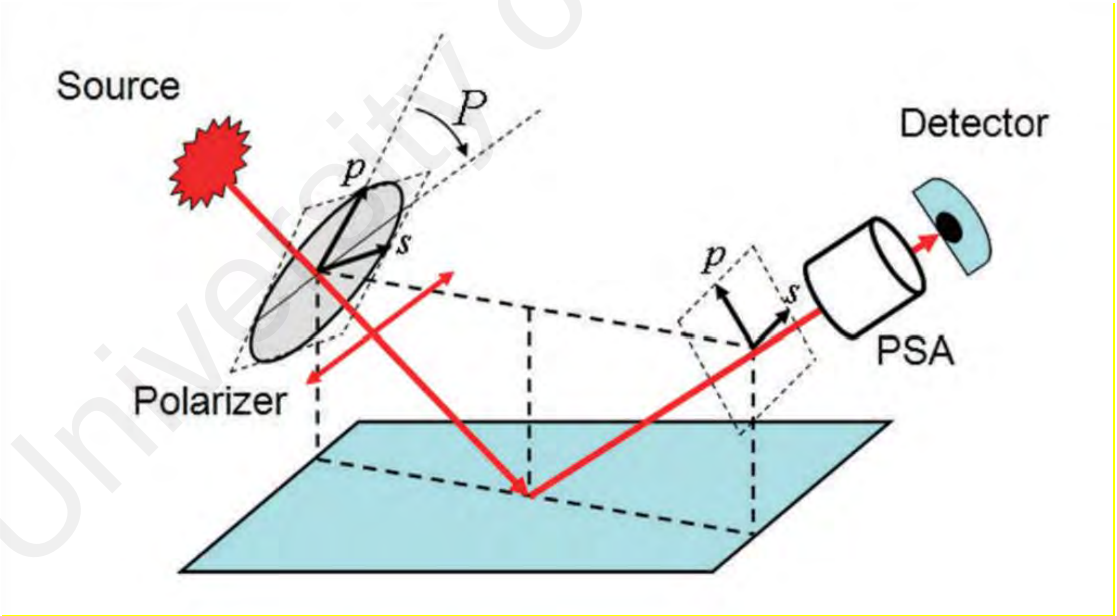

Figure 2.3: Schematic diagram of spectroscopic ellipsometer. PSA is polarization state analyzer (Garcia-Caurel et al., 2013).

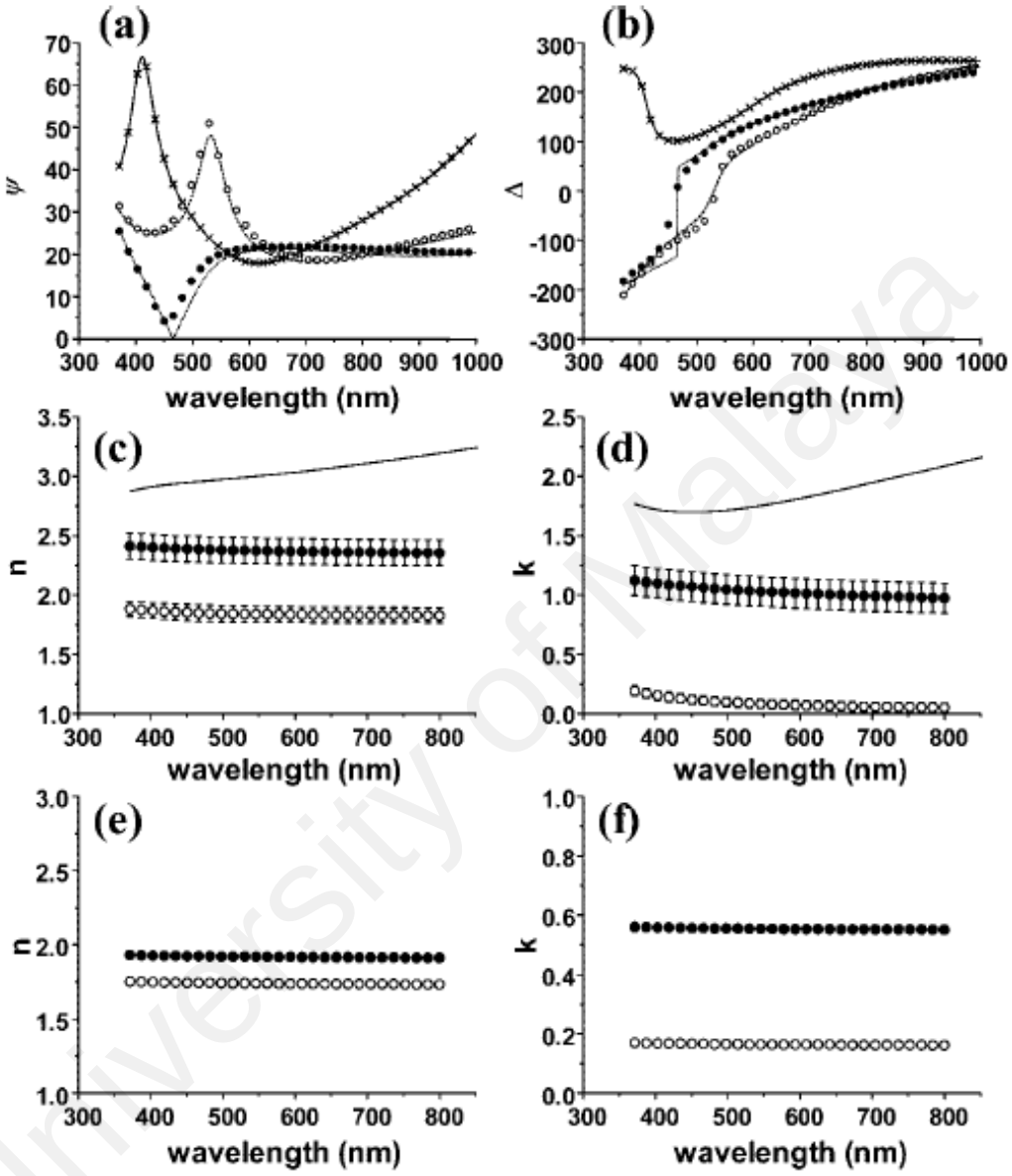

Figure 2.4: (a), (b) Spectroscopic ellipsometry experimental data for substrate (x) and GO stacks before (o) and after (•) thermal treatment, solid line represents the calculated data. (c), (d) Complex refractive index of GO stacks before (o) and after (•) thermal treatment, solid line represents pyrolytic graphite sheets. (e), (f) Complex refractive index of single and multilayer GO before (o) and after (•) thermal treatment (Jung et al., 2008).

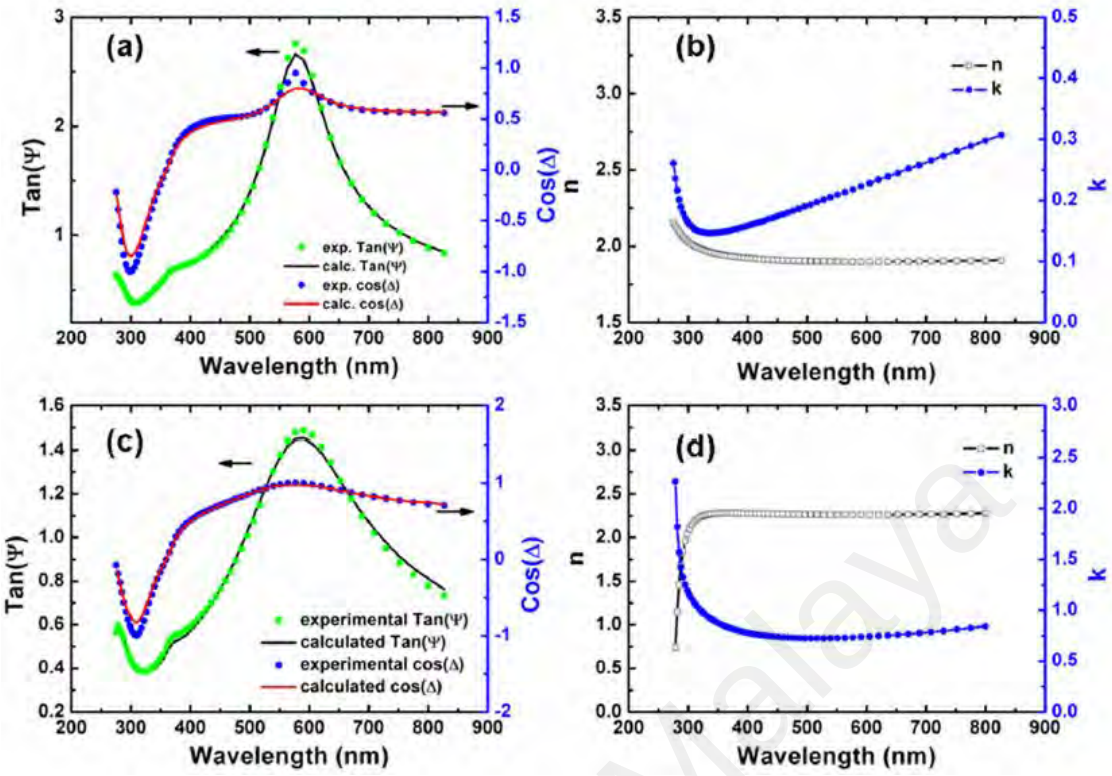

Figure 2.5: The experimental and calculated spectroscopic ellipsometry data of (a) GO and (c) rGO. The calculated values of *n* and *k* of (b) GO (d) rGO (Shen et al., 2011).

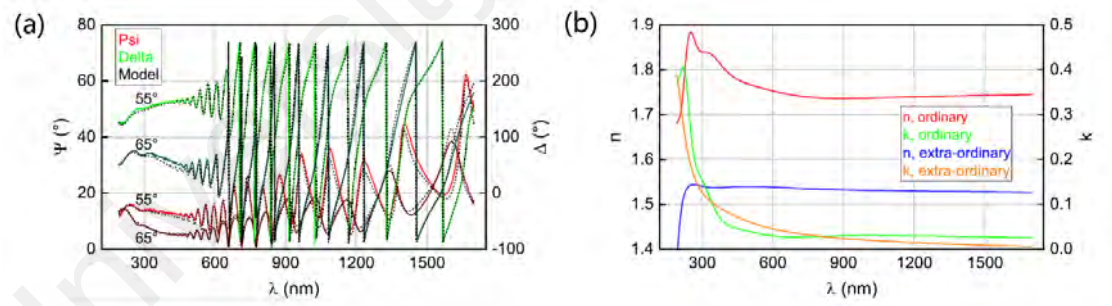

Figure 2.6: (a) ψ (red) and Δ (green) experimental data (solid) and best-match model data (dash) of GO at single measurement. (b) Model derived anisotropic complex refractive index of GO in the function of wavelength λ (Schöche et al., 2017).

Most recently, Stefan et al. show an extraordinary result of the optical constant of GO determined by spectroscopic ellipsometry in which they are able to determine the anisotropic complex refractive index of GO at a wide wavelength range which includes 1550 nm through multiple spot analysis of spatially resolved data over the exposed region (Schöche et al., 2017). Multiple sample of GO are analysed using two different incident angles on nine regions of the sample, the ellipsometer parameters data for single measurement is shown in Figure 2.6 (a). In order to match the experimental data with model data, an anisotropic dielectric function tensor have to be applied. The model derived anisotropic optical constant of GO in the function of wavelength λ is shown in Figure 2.6 (b). The complex refractive index of GO is found to be 1.53+0.01i and 1.76+0.03i for TM- and TE-polarized light, at 1550 nm, respectively.

Spectroscopic ellipsometry is a non-destructive optical measurement technique that can be used to determine the complex refractive index of thin film. However, reports by Jung et al. (Jung et al., 2008) and Shen et al. (Shen et al., 2011) only cover the wavelength up to 1000 nm and did not take into account the anisotropic optical nature of GO. To date, only Stefan et al. (Schöche et al., 2017) investigated the anisotropic complex refractive index of GO at wavelength covering the common telecommunication c-band (1530-1565 nm). Therefore, these values will be used as reference in the current study.

2.2.5 Terahertz time-domain spectroscopy

Time-domain spectroscopy (TDS) is an optical technique that measures the EM wave power as a function of time. TDS normally require the use of Fourier transform to convert information in the time-domain into frequency domain. TDS has several advantages over frequency domain spectroscopy (FDS). In FDS, each of the wavelength have to be

measured one at a time, which is very time consuming. In TDS, a single pulse containing all frequency components are used instead in the measurement. This enables multiple TDS scans to be carried out on the same sample and being averaged to get a more accurate measurement. Hong et al. has successfully determined the frequency dependent complex refractive index of rGO film using terahertz time-domain spectroscopy (THz-TDS) (Hong et al., 2013). The complex optical constant of rGO film can be extracted from the changing of amplitude and phase of the THz pulse after passing through the rGO film. By using complex Fourier transform, the complex AC conductivity, $\tilde{\sigma}(\omega)$ for thin film limit $|n\omega d/c| \ll 1$ can be obtained from the thin film equation below,

$$\frac{E_{rGO+sub}(\omega)}{E_{sub}(\omega)} = \frac{1+n_{sub}}{1+n_{sub}+Z_0\tilde{\sigma}(\omega)d} \tag{2.20}$$

where $E_{rGO+sub}(\omega)$and $E_{sub}(\omega)$ are the time-dependent electric field of THz pulse passing through rGO film on substrate and substrate only, respectively; n is the refractive index of rGO film; n_{sub} is refractive index of substrate; ω is the frequency of the THz radiation; d is the thickness of rGO film; c is the speed of light and Z_0 is the vacuum impedance of free space. The complex conductivity of rGO film which is frequency-dependent is interpreted using Drude free-electron model, as shown in eqn. (2.21),

$$\tilde{\sigma} = \frac{\varepsilon_0\omega_p^2 t}{1-i\omega t} \tag{2.21}$$

where ω_p is the plasma frequency, t is the scattering time, and ε_0 is the vacuum permittivity. The frequency-dependent complex refractive index, $\tilde{n} = n + ik$ can then be extracted from its relationship with complex conductivity, $\tilde{\sigma} = i\varepsilon_0\omega(1-\tilde{\varepsilon})$ and $\tilde{n}^2 = \tilde{\varepsilon}$, where $\tilde{\varepsilon}$ is the complex relative permittivity. The *ac* conductivity of the rGO film at THz frequency and its complex refractive index extracted from the complex conductivity are shown in Figure 2.7. The complex refractive index of GO is found to be 30+26*i* at 1 THz.

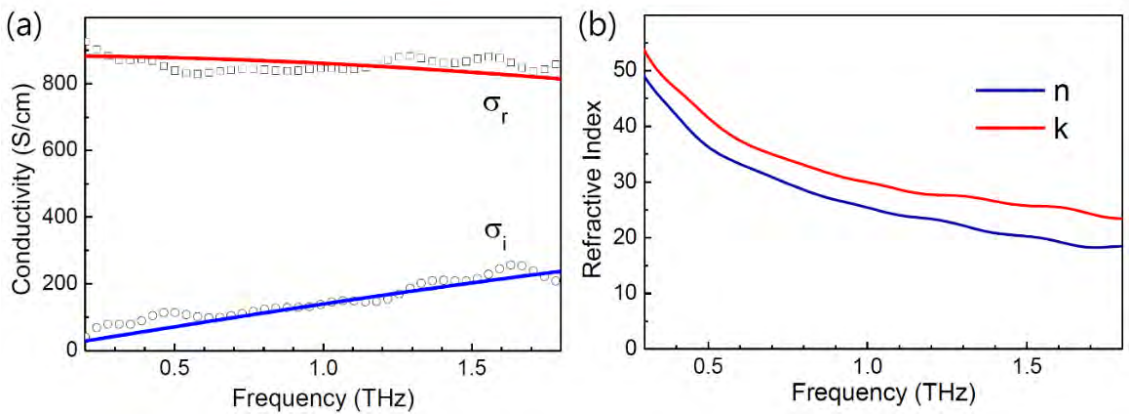

Figure 2.7: (a) The real and imaginary part of the ac conductivity of rGO film. (b) The real and imaginary part of the complex refractive index of rGO film obtained from the complex conductivity in (a) (Hong et al., 2013).

2.2.6 Summary

The results of complex refractive index of GO determined using various optical technique above are summarized in Table 2.1. As can be seen, most of the work were done in the visible wavelength or THz range, with the exception of (Schöche et al., 2017). It is also worth noting that only Stefan's group consider the intrinsic anisotropic properties of GO. This is one of the primary motivations of our research project, which is to obtain a better understanding about the anisotropic optical constants of GO at the optical fiber telecommunication window of 1550 nm. As compared to the conventional optical characterization methods mentioned above, here, optical chip-based device: planar optical waveguide is used instead to determine the anisotropic complex refractive index of GO. Hence, Section 2.3 will discuss the wave guiding principle, structure and various types of waveguide material used in planar optical waveguide.

Table 2.1: Complex refractive index of GO determined by various optical technique

Material	Methodology	Wavelength	Complex refractive index
GO (Jung et al., 2007)	Optical microscopy	488, 543, 633 nm	2.0+0.3*i* at 633 nm
rGO (Jung et al., 2007)	Optical microscopy	488, 543, 633 nm	2.1+0.55*i* at 633 nm
GO (Jung et al., 2008)	Ellipsometry	350-1000 nm	1.88+0.1*i* at 600 nm
rGO (Jung et al., 2008)	Ellipsometry	350-1000 nm	2.4+1.0*i* at 600 nm
GO (Shen et al., 2011)	Ellipsometry	275-826 nm	1.9+0.24*i* at 600 nm
rGO (Shen et al., 2011)	Ellipsometry	275-826 nm	2.25+0.75*i* at 600 nm
GO (Schöche et al., 2017)	Ellipsometry	193-1690 nm	1.53+0.01*i* (TM) at 1550 nm 1.76+0.03*i* (TE) at 1550 nm
rGO (Hong et al., 2013)	THz-TDS	0.2-1.8 THz	30+26*i* at 1 Thz

2.3 Planar optical waveguide

2.3.1 Introduction

In 2009, the Nobel Prize in Physics was awarded to Charles K. Kao for his groundbreaking achievement regarding the transmission of light in optical fiber for telecommunication. The invention of the optical fiber and its application in optical communications - which allows information to be transmitted globally in an instance - has totally changed our daily life over the years. Optical fiber communication possesses not only higher bandwidth and longer data transmission distance when compared to traditional copper wire communications, but also has the benefit of immunity to

electromagnetic interference. These advantages have established optical fiber as the backbone of long haul optical communication systems.

Today, advancement in silicon electronics are reaching its bottleneck as quantum tunneling effect is becoming more significant due to continue miniaturization of transistors in silicon chip. One of the solutions to this bottleneck is to replace these electronics functions with all-optical functions. In other word, replacing electrons with photons as signal carriers. Intense research on achieving all-optical signal processing has been carried out by scientists around the world. 1-dimensional optical devices such as Fiber Bragg Grating (FBG), which serves as a narrow-band wavelength filter, can be fabricated directly on optical fiber through interference lithography. However, more complex optical functions such as array waveguide grating (AWG), Y-branch splitter and interferometry structures cannot be produced in the same way and can only be integrated onto a 2-dimensional planar platform, which is termed Planar Lightwave Circuit (PLC) or planar optical waveguide. This section will provide a description on the waveguide theory, materials used to fabricate PLC, different type of waveguide structures, and its potential.

2.3.2 Waveguide Theory

Optical waveguide consist of a core, where light is being guided, is surrounded by the cladding and substrate with lower refractive index, as shown in Figure 2.8. The refractive index of the core, cladding and substrate are denoted n_c, n_{clad} and n_{sub} respectively. Light is confined along the z-axis while this geometrical waveguide structure is extended to infinity in the y-axis. The primary working principle of an optical waveguide is Total Internal Reflection (TIR), which occurs at the core-cladding boundary due to their

difference in refractive index. For simplicity, n_{sub} is assumed to be equal to n_{clad} . According to Snell's law, the relation between the values of n_{in}, θ_{in}, n_c and θ_c is shown in eqn. 2.22,

$$n_{in} sin\theta_{in} = n_c sin\theta_c \tag{2.22}$$

where θ_{in} and θ_c are the acceptance angle and critical propagation angle, respectively. Light ray entering the core at an incident angle within θ_{in} will be refracted at the air-core interface at a propagation angle within θ_c. The refracted light ray in the waveguide core will arrive at the core-cladding interface at an angle less than the critical angle, α_0 and undergo TIR back into the core. TIR of the light ray will continue until the light ray reaches the opposite end of the waveguide. Any stray light which is incident upon the air-core boundary at an incident angle larger than θ_{in} will be refracted at an angle larger θ_c and smaller α_0. As the refracted stray light reaches the core-cladding interface at an angle less than the critical angle, α_0, it will be refracted out to the cladding instead of experiencing TIR and eventually be lost by radiation.

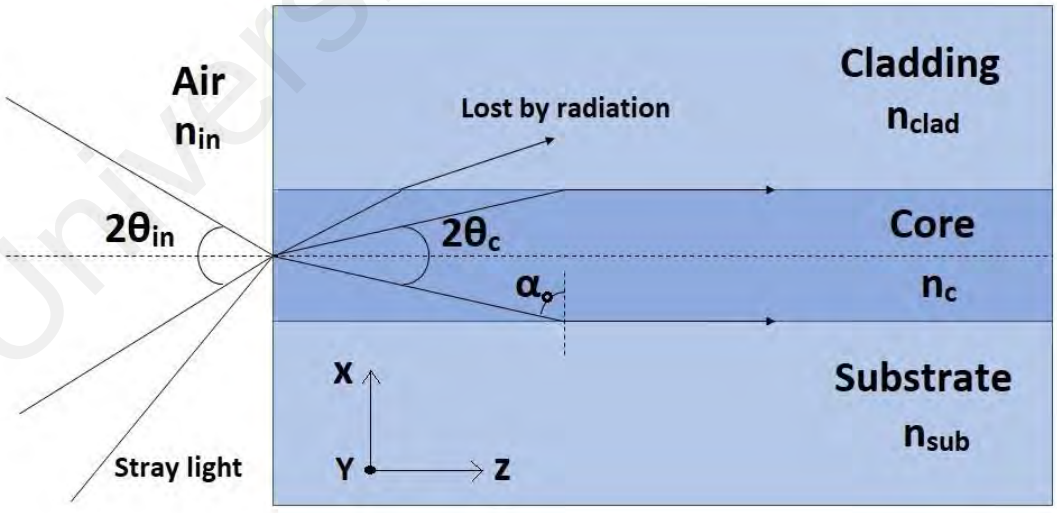

Figure 2.8: Geometrical structure of the optical waveguide (Okamoto, 2006).

The numerical aperture (NA) is a dimensionless number used to define the range of incident angles in which the waveguide can accept or emit light and is related to the critical propagation angles, as shown in eqn. 2.23,

$$NA = sin\ \theta_{in} = n_c sin\ \theta_c \tag{2.23}$$

By using Snell's law and Pythagoras' theorem, $sin\ \theta_c$ can be replaced by the following relations,

$$n_c sin\ \alpha_0 = n_{clad} sin 90^o = n_{clad} \tag{2.24}$$

$$\sin \alpha_0 = \cos \theta_c = \frac{n_{clad}}{n_c} \tag{2.25}$$

$$sin\ \theta_c = \sqrt{1 - cos^2\ \theta_c} = \sqrt{1 - \frac{{n_{clad}}^2}{{n_c}^2}} \tag{2.26}$$

Thus, NA can be rewritten as,

$$NA = sin\ \theta_{in} = n_c sin\ \theta_c = \sqrt{{n_c}^2 - {n_{clad}}^2} \tag{2.27}$$

In addition, NA is also related to the normalized refractive index difference, Δ_0 between the waveguide core and cladding as shown in eqn. 2.28. By solving eqn. 2.27 and eqn. 2.28, NA can be rewritten as eqn. 2.29,

$$\Delta_0 = \frac{{n_c}^2 - {n_{clad}}^2}{2{n_c}^2} \cong \frac{n_c - n_{clad}}{n_c} \tag{2.28}$$

$$NA = n_c \sqrt{2\Delta_0} \tag{2.29}$$

The description of light guiding mechanisms of optical waveguide above is not complete as the ray optics model is just a partial depiction of the characteristic of light propagating inside an optical waveguide. Particularly, it only describe the propagating direction of light in an optical waveguide but does not consider the interference that occurs between waves propagating in the waveguide. If interference is taken into account, it is found that

only distinct modes with discrete angle of propagation can be guided inside the waveguide. These propagation modes can be described using the electromagnetic mode theory.

Consider a plane electromagnetic plane wave traversing along the z-axis of a medium with refractive index of n_1,an angle, ϕ, and with the phase front perpendicular to its propagating direction, as shown in Figure 2.9. The wavelength of the light ray is $\frac{\lambda}{n_1}$ while its wavenumber is kn_1, given that λ is the wavelength of light in vacuum and $k = \frac{2\pi}{\lambda}$. The propagation constant of light in the z- and x-axis can be written as eqn. (2.30) and eqn. (2.31), respectively,

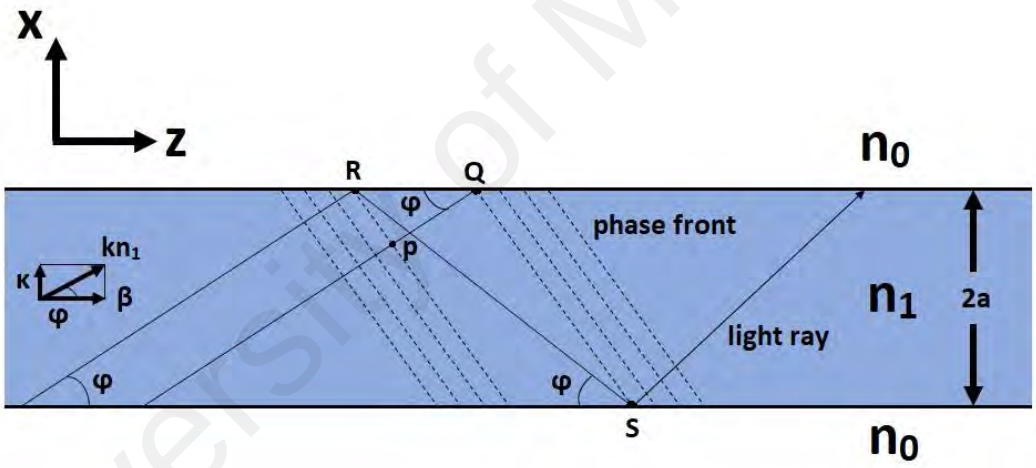

Figure 2.9: Light rays and phase front in optical waveguide (Okamoto, 2006).

$$\beta = kn_1 \cos\varphi \tag{2.30}$$

$$\kappa = kn_1 \sin\varphi \tag{2.31}$$

Before detailing the mode formation in waveguide, we have to discuss about the phase shift that the guided light experienced during total internal reflection. The reflection coefficient of light ray polarized perpendicular to the incident plane (TE-mode) reflected from the core-cladding boundary is shown in eqn. (2.32),

$$r = \frac{A_r}{A_i} = \frac{n_1 \sin\varphi + j\sqrt{n_1^2 \cos^2\varphi - n_0^2}}{n_1 \sin\varphi - j\sqrt{n_1^2 \cos^2\varphi - n_0^2}} \tag{2.32}$$

The complex reflection coefficient, r is expressed as $r = \exp(-j\phi)$, so the amount of phase shift, ϕ is shown in eqn. (2.33) with the substitution of eqn. (2.28). This phase shift for light undergoing total internal reflection is known as Goos-Hanchen shift,

$$\phi = -2\tan^{-1}\frac{\sqrt{n_1^2 \cos^2\varphi - n_0^2}}{n_1 \sin\varphi} = -2\tan^{-1}\sqrt{\frac{2\Delta_0}{\sin^2\varphi} - 1} \tag{2.33}$$

From Figure 2.9, it can be seen that the light ray PQ is not affected by the reflection, while the light ray RS experiences total internal reflection twice - at the top and bottom core-cladding interfaces. As the points P, R or Q, S are on the same phase front, the optical pathlength for PQ and RS (including two Goos-Hanchen phase shifts experienced by light ray RS) should be the same or an integral multiple of 2π. The length of PQ, L_{PQ} and of RS, L_{RS} are expressed as eqn. (2.34) and eqn. (2.35) below,

$$L_{PQ} = \left(\frac{2a}{\tan\varphi} - 2a\tan\varphi\right)cos\varphi = 2a\left(\frac{1}{\sin\varphi} - 2\sin\varphi\right) \tag{2.34}$$

$$L_{RS} = \frac{2a}{sin\varphi} \tag{2.35}$$

The phase matching condition for light rays PQ and RS can be expressed as eqn. (2.36),

$$(kn_1 L_{RS} + 2\phi) - kn_1 L_{PQ} = 2m\pi \tag{2.36}$$

where $m = 0,1,2,3,$ ..... By subtracting eqn. (2.33) with eqn. (2.35) and substituting the product into eqn. (2.36), the condition for the propagation angle is obtained as eqn. (2.37),

$$tan\left(kn_1\, a\, sin\,\varphi - \frac{m\pi}{2}\right) = \sqrt{\frac{2\Delta_0}{sin^2\,\varphi} - 1} \tag{2.37}$$

Eqn. (2.37) indicates that the propagation angle of light is discrete in nature and is determined by the core radius (a), refractive index of core (n_1), refractive index

difference (Δ) and the wavelength of the light (as $k = \frac{2\pi}{\lambda}$). The optical field distribution which satisfies eqn. (2.37) is called a propagation mode and possesses a discrete propagation constant, β_m where $m = 0,1,2,3, ...$ The mode with minimum propagation angle φ (m=0) is called the fundamental mode, while modes with larger angle ($m \geq 1$) are called higher order modes. Figure 2.10 (a) and (b) illustrates the standing waves created by the fundamental mode and higher order modes, respectively. From the figures, it can be seen that the positive phase front and negative phase front meet at the core-cladding boundary and cancel each other by destructive interference. On the other hand, when two positive or negative phase front meet at the middle (fundamental mode) and one fourth position (higher order modes, m=1) of the waveguide core, the electric field amplitude become maximum or minimum, respectively. Thus, the optical field distribution across the x-axis becomes a standing wave, while it varies periodically along z-axis with wavelength as shown in eqn. (2.38),

$$\lambda_p = (\lambda / n_1) / \cos\varphi = \frac{2\pi}{\beta} \tag{2.38}$$

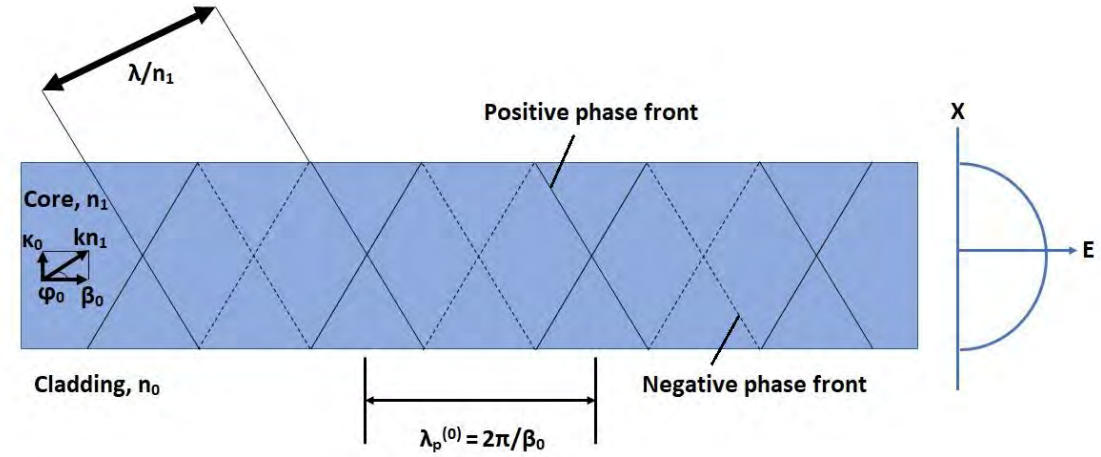

(a) Fundamental mode (m=0)

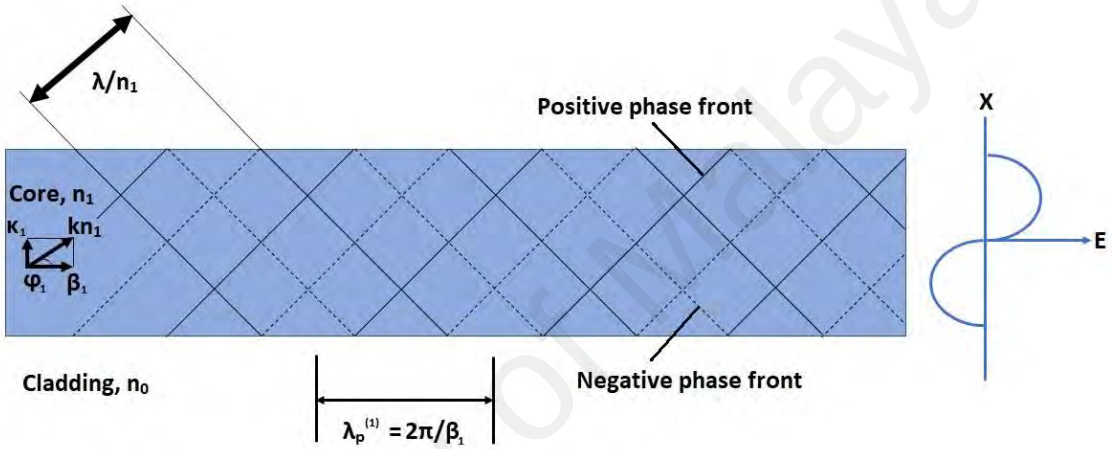

(b) Higher order modes (m=1)

Figure 2.10: Formation of (a) fundamental mode and (b) higher order modes (m=1)

From eqn. (2.27) and eqn. (2.29), the propagation critical angle can be related to Δ_0 as $sin\,\varphi = \sqrt{2\Delta_0}$. To achieve light confinement by TIR, the following condition need to be fulfilled,

$$\xi = \frac{\sin\varphi}{\sqrt{2\Delta_0}} \leq 1 \tag{2.39}$$

By using the trigonometry relation, $\tan^{-1} x = \cos^{-1}\frac{1}{\sqrt{1+x^2}}$ and eqn. (2.39), eqn. (2.37) can rewritten as eqn. (2.40),

$$kn_1 a\sqrt{2\Delta_0} = ka\,NA = \frac{\cos^{-1}\xi + m\frac{\pi}{2}}{\xi} = V \tag{2.40}$$

This V-number is known as the normalized frequency, which can determine the propagation characteristic of an optical waveguide (independent of their structure), such as confinement of energy of light in the waveguide core for different wavelengths and the number of modes supported by the waveguide. For example, in the case of fundamental mode (m=0), since ξ is smaller or equals to 1, the V-number, $V \leq \frac{\pi}{2}$. This means that for the waveguide to supports only a single mode, its V-number must be equal to or lower than $\frac{\pi}{2}$. This is called cut-off V-number, v_c. When we express eqn. (2.40) in term of cut-off wavelength, λ_c, we will obtain,

$$\lambda_c = \frac{2\pi}{v_c} a n_1 \sqrt{2\Delta_0} \tag{2.41}$$

In optical fiber, the cut-off V-number is derived from the same mathematical approach and is found to be 2.405. Fibers with V-number of more than 2.405 can support up to nearly $V^2/2$ modes. In this experimental work, the waveguide dimension is controlled to excite only fundamental mode, so that mode analysis can be done straight forward and time-saving.

2.3.3 Waveguide Material

There are many suitable optical materials for planar optical waveguide fabrication, such as silica (Kawachi, 1990), silicon (Paniccia et al., 2004), lithium niobite (Tanzilli et al., 2001), indium phosphide (Leijtens, 2011) and polymer (Taboada et al., 1999). The choice of optical material will determine the features and limitations for that particular planar optical waveguide. Silica is a very attractive material for passive optical devices because it is highly transparent (low-loss) in the telecommunication window and has excellent light coupling efficiency with optical fiber which is also made of silica. On the other hand, silicon possesses the advantage of compatible fabrication processes with the

established semiconductor manufacturing processes and high index contrast which allow optical designs with compact footprint and therefore high integration density. Furthermore, optical waveguide fabricated using lithium niobate is suitable for active devices such as acousto-optic transducers or electro-optic modulator. However, the downside of using lithium niobate in waveguide fabrication is that it is very difficult to produce polarization-independent device - which is usually needed in fiber optics communication system - due to its intrinsically high birefringence. Indium phosphide is another waveguide material in high performance large scale PLC, thanks to its high electron mobility and tunable bandgap. Indium phosphide is a binary III-V semiconductor that can cover the emission/absorption wavelength range from 0.9 μm to 2 μm by introducing strained material (e.g. Gallium arsenide, Indium arsenide) into the system. As the refractive index is inversely proportional to bandgap energy, indium phosphide itself, with larger bandgap, can act as cladding of an optical waveguide, while indium gallium arsenide, with smaller bandgap, can form the core of an optical waveguide. Therefore, indium phosphide material platform is capable of forming monolithic integrated circuit with all necessary active components (lasers, modulators, photodetector) and passive component (waveguide interconnects, couplers). Finally, polymer as a material for optical waveguide provides an easy and economics way to prototyping and mass production as the fabrication process normally does not involve high temperature or vacuum deposition. Polymers used to form waveguide is usually light sensitive photoresist and can be patterned through photolithography or laser direct writing. Examples of polymer material for waveguide fabrication are polymethyl methacrylate (PMMA) and SU-8. Polymer optical waveguides are passive, with the possibility of performing optical switching by utilizing the thermo-optic effect, which is usually large in polymers. In this work, doped-silica with higher refractive index is used as core, while normal silica is used as cladding. This silica waveguide which is transparent in c-band wavelength is the most suitable

platform for our project: To investigate the anisotropic complex refractive index of GO in 1550 nm.

2.3.4 Waveguide Structures

The basic structure of an optical waveguide consists of a medium with higher refractive index, called the core, surrounded by other mediums with lower refractive index, called the cladding. The guided electromagnetic wave propagates in the waveguide core in the longitudinal direction. The propagation characteristic of an optical waveguide depends on its cross-sectional or transverse refractive index distribution profile. A waveguide with an index profile that changes abruptly at the core-cladding boundary is called a step-index waveguide, whereas waveguide which index profile changes gradually is called graded-index waveguide. The planar waveguide structures can be categorized into five different groups, which are slab, ridge, rib, buried and planarized waveguide. The cross-sectional illustration of these five waveguide structures are shown in Figure 2.11. Their characteristics are briefly described as follow:

- Slab waveguide: An optical waveguide consisting a high index dielectric layer sandwiched by two low index dielectric layer. It is relatively lossier than other structures because the confinement only exist in one transverse direction.
- Ridge waveguide: An optical waveguide in which a high index strip waveguide is placed on top of a low index planar cladding. It has relatively stronger confinement because the core is surrounded by low index air or cladding.
- Rib waveguide: An optical waveguide that has a similar structure to ridge waveguide, only that the planar layer beneath the high index core is also part of the core.

- Buried waveguide: An optical waveguide with its high index core surrounded all around by low index cladding. Normally, it can only be passive device as it is isolated from the surroundings.
- Planarized waveguide: An optical waveguide where the core is sandwiched side-by-side by two low index side cladding and placed on top of another low index under cladding. Only the top section of the core is exposed to surrounding (air or coating).

The slab waveguide is not suitable to be used as the waveguide structures in this work, because it only allows single transverse confinement of light which leads to high loss. For ridge and rib waveguides, there are three interfaces of the waveguide core that is exposed to the surrounding. This will result in increased complexity in the interaction of different polarizations modes of the waveguide core with its surroundings, which makes measuring the orthogonal polarization responses of GO-coated waveguide challenging. For buried waveguide, as its core is surrounded entire with waveguide cladding, light propagating in the waveguide core is not exposed to the surrounding at all. Hence, planarized waveguide which has only one interacting surface with the surrounding (i.e. GO-coating) is selected as the waveguide structure in this work. Interaction of light propagating in the waveguide core with GO coated on the top surface can then be distinguished according to the polarization states of light. As a result, the optical properties of GO thin film can be determined with smaller uncertainty through analyzing the polarization response of the GO-coated planarized optical waveguide.

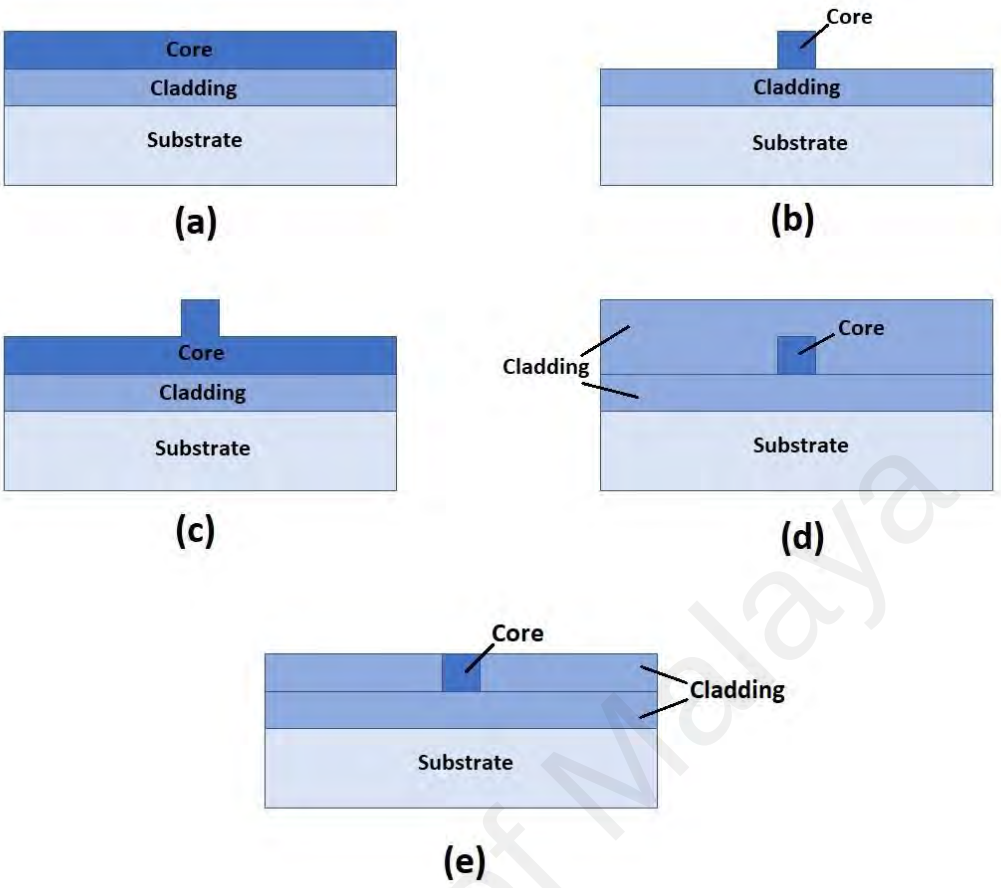

Figure 2.11: Different kind of waveguide structures: (a) Slab waveguide. (b) Ridge waveguide. (c) Rib waveguide. (d) Buried waveguide. (e) Planarized waveguide

2.3.5 Optical Waveguides with High Refractive Index Overlays

In the early 1970s, the effect of adding a dielectric thin film overlay with higher refractive index onto a slab waveguide were studied for their potential in optical applications . Tien et al. demonstrated that light guiding interconnection can be formed in an integrated optical circuit by bridging the optical device with a high index thin film having both ends tapered (Tien et al., 1973). Besides, Batchman et al. also performed a computer modeling of 4 layers silicon-clad planar optical waveguide and shows that the mode index and attenuation behave as exponentially decaying sinusoids when the thickness of the silicon-clad was increased (Batchman & McWright, 1982). Studies carried out by Gauthier et al., by adding a thin film overlay with higher index on a 3-

layers slab waveguide system, shows that the amplitude of the modal power is located within the high index layer while the effective index is in between the values of the substrate and the waveguide (Gauthier et al., 2012). The literatures above shows that the light propagation characteristic in a planar waveguide is highly sensitive to the presence of dielectric thin film overlay integrated on top of the waveguide. Therefore, thin film overlays can be used as an approach to functionalize a passive optical waveguide. The same approach can also be used to determine the optical properties, namely the complex refractive index, of a dielectric thin film materials by analyzing the optical response of planar waveguide coated with the dielectric thin film overlay and then cross-referencing with suitable simulation model.

In this work, a planarized optical waveguide structure that allows only one interacting interface with thin film overlay will be used. Silica is used as waveguide material as the low light propagation loss will simplify the determination of the complex refractive index of GO. However, before proceeding to experiment works, simulations is first carried out to study the optical characteristic of planarized optical waveguide, namely its effective mode index. Then, the effect of thin film coating on the optical waveguide optical characteristics will be studied. Particularly, the change in effective mode index of thin film coated waveguide with different thin film coating thicknesses and complex refractive indices, are rigorously studied, which will be discussed on the Chapter 3.

2.4 Finite Element Method

2.4.1 Introduction

The simulation method used in this work to study light propagation in an optical waveguide is Finite Element Method (FEM). In classical analytical procedures, an optical system is modeled using analytical functions defined over the whole domain of interest, which limits its application to simple waveguide geometries only. FEM is a numerical method that can solve the boundary-value problems characterized by a series of partial differential equations (Maxwell's equation in electromagnetism case) and a set of boundary conditions. The domain of the boundary-value problem is discretized into sub-domains called finite elements. Each element has an approximated solution for the problem, and it is linked at the nodal points of those elements to form a solution model for the entire domain. A series of linear equations are first obtained for each of the discretized element. Then, a global matrix can be formed after the assembly of all elements. Therefore, FEM is a powerful tool for mode analysis in optical waveguide with arbitrary refractive index profile and complicated domain structures.

In general, FEM analysis can be categorized into three sections: variational formulation, discretization of functional and computation (Okamoto, 2006). Since FEM is capable of solving wave equation for waveguide with arbitrary refractive index profiles, a slab waveguide with inhomogeneous core index, as shown in Figure 2.12, is used as an example. The region $0 \leq x \leq A$ with inhomogeneous refractive index distribution is denoted as the core (maximum refractive index = n_1), while the constant distribution of n_0 ($x \leq 0$) and n_s ($x \geq 0$) are denoted as the cladding and substrate, respectively.

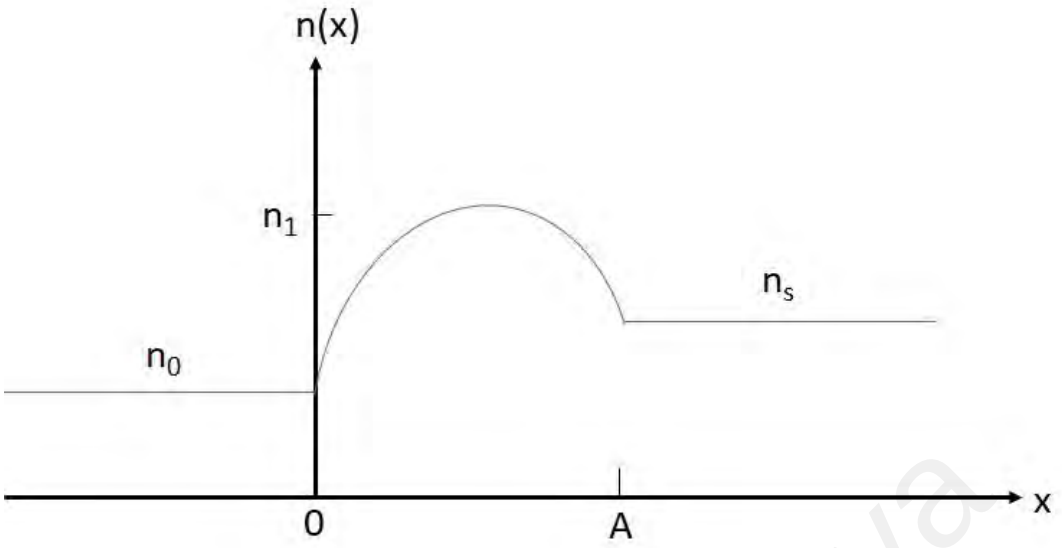

Figure 2.12: Distribution of refractive index of the slab optical waveguide with inhomogeneous core index

2.4.2 Variational formulation – Model setup

The formulation of FEM starts with the general TE-mode equation which is shown in eqn. (2.42). The boundary conditions require the continuity of electric field in y-axis, E_y and magnetic field in z-axis, H_z at $x = 0$ and $x = A$, which is described by eqn. (2.43). However, before transforming the TE-mode wave equation (2.42) and boundary condition (2.43) into variational formulation, the parameters are normalized as in eqn. (2.44).

$$\frac{d^2E_y}{dx^2} + (k^2n^2 - \beta^2)E_y = 0 \tag{2.42}$$

$$H_z = \frac{j}{\omega\mu_0}\frac{dE_y}{dx} \tag{2.43}$$

$$p = \frac{x}{a}\ ;\ E_y(x) = R(p)\ ;\ D = \frac{A}{a} \tag{2.44}$$

where $R(p)$ and $\frac{dR(p)}{dp}$ are continuous at $p = D$ and $p = 0$. Eqn. (2.42) and (2.43) are rewritten as eqn. (2.45),

$$\frac{d^2R}{dp^2} + [(v^2q(p) - \omega^2)]R = 0 \tag{2.45}$$

The normalized frequency v, normalized refractive index distribution $q(p)$ and normalized transverse wavenumber ω can be defined as follow,

$$\omega = a\sqrt{\beta^2 - k^2n_s^2} \tag{2.46}$$

$$v = ka\sqrt{n_1^2 - n_s^2} \tag{2.47}$$

$$q(p) = \frac{n^2 - n_s^2}{n_1^2 - n_s^2} \tag{2.48}$$

The solution for the variational formulation (wave equation) under the constraint of boundary condition which satisfies the functional with stationary condition is defined as,

$$I[R] = -\int_{-\infty}^{\infty} \left(\frac{dR}{dp}\right)^2 dp + \int_{-\infty}^{\infty} [v^2q(p) - \omega^2]R^2\, dp \tag{2.49}$$

By assuming that $I[R]$ is stationary for $R(p)$ and considering a slightly deviated function, the validity of variational method is shown as eqn.(2.50),

$$R_{pert}(p) = R(p) + \delta \cdot \eta(p) \tag{2.50}$$

where δ is a very small quantity of deviation and $\eta(p)$ is the arbitrary continuous function of p.

By substituting $R_{pert}(p)$ into eqn. (2.49) and taking $I[R_{pert}]$ as stationary when $\delta = 0$, a new relation is obtained as eqn. (2.51). After partial integration, eqn. (2.51) is rewritten into eqn. (2.52).

$$\lim_{\delta \to 0}\left\{\frac{1}{2}\frac{\partial}{\partial \delta} I[R_{pert}]\right\} = -\int_{-\infty}^{\infty} \frac{dR}{dp}\frac{d\eta}{dp}\, dp + \int_{-\infty}^{\infty} [v^2q(p) - \omega^2]R\eta\, dp = 0 \tag{2.51}$$

$$-\left[n\frac{dR}{dP}\right]_{-\infty}^{\infty}+\int_{-\infty}^{\infty}\left\{\frac{d^2R}{dp^2}+[v^2q(p)-\omega^2]R\right\}\eta(p)dp=0 \qquad (2.52)$$

The first and second terms in eqn. (2.52) equal to zero given that $\eta(p)$ is an arbitrary function of p. Then the $R(p)$ will satisfy the wave equation - eqn. (2.45), and the boundary condition of $\frac{dR}{dp}$ is continuous and $\lim_{p\to\pm\infty}\frac{dR}{dp}=0$. The second term in boundary condition shows that the electromagnetic wave will decay at the infinity. It is also proven that $R(p)$ enables the functional (2.49) stationary to satisfy the wave equation – eqn. (2.45) and the boundary condition – $R(p)$ and $\frac{dR(p)}{dp}$ are continuous at $p=D$ and $p=0$, simultaneously.

2.4.3 Discretization of the functional - Meshing

To simplify the calculation of functional, the electric field profile in the waveguide core is discretized using eqn. (2.53),

$$R(p)=\begin{cases}R_0\,exp(\omega_0 p) & (p<0)\\ \sum_{i=0}^{N}R_i\phi_i(p) & (0\le p\le D)\\ R_N\,exp[-\omega(p-D)] & (p>D)\end{cases} \qquad (2.53)$$

where R_0-R_N are the electric field values at that particular sub-domain.

The normalized transverse wavenumber, ω_0, normalized electric field R_i and normalized domain position p_i are defined as,

$$\omega_0 = a\sqrt{\beta^2 - k^2 n_0^2}$$

$$R_i = R(p_i) \quad (i = 0 - N) \tag{2.54}$$

$$p_i = i\frac{D}{N} \quad (i = 0 - N)$$

The solution in the substrate and cladding is relatively simpler, so it can be given by the analytical functions. Hence, the precise expressions for $\phi_i(p)$ are shown in eqn. (2.55).

$$\begin{aligned}
\phi_0(p) &= \tfrac{N}{D}(p_1 - p) \quad (0 \le p \le p_1) \\
&\quad 0 \qquad\qquad all\ other\ areas \\
\phi_i(p) &= \tfrac{N}{D}(p - p_{i-1}) \qquad (p_{i-1} \le p \le p_i) \\
&\quad \tfrac{N}{D}(p_{i+1} - p) \qquad (p_i \le p \le p_{i+1}) \\
&\quad 0 \qquad\qquad all\ other\ areas \\
\phi_N(p) &= \tfrac{N}{D}(p - p_{N-1}) \qquad (p_{N-1} \le p \le p_N) \\
&\quad 0 \qquad\qquad all\ other\ areas
\end{aligned} \tag{2.55}$$

Since $\phi_i(p)$ is a linear function of p, eqn. (2.53) has the continuous function of $R(p)$ is approximated by broken lines. On the other hand, the normalized distribution of refractive index $q(p)$ can also be approximated by $\phi_i(p)$, as shown in eqn. (2.56), when dealing with waveguides having arbitrary refractive index profile.

$$q(p) = \textstyle\sum_{i=0}^{N} q_i \phi_i(p)\,;\ q_i = \frac{n^2(p_i) - n_s^2}{n_1^2 - n_s^2} \tag{2.56}$$

Finally, by substituting eqn. (2.53) into eqn. (2.49), the functional is obtained as eqn. (2.57).

$$I = -\omega_0 R_0^2 - \int_0^D \left(\frac{dR}{dp}\right)^2 dp + \int_0^D [v^2 q(p) - \omega^2] R^2 dp - \omega R_N^2 \tag{2.57}$$

2.4.4 Dispersion equation based on stationary condition - computation

The functional – eqn. (2.57) at stationary condition, is given by partially differentiating it with respect to $R_i (i = 0 - N)$,

$$0 = \frac{1}{2}\frac{\partial I}{\partial R} = -\omega_0 R_0 \delta_{i,0} - \int_0^D \frac{dR}{dp}\frac{d\phi_i}{dp} dp + v^2 \int_0^D q(p) R \phi_i \, dp$$

$$-\omega^2 \int_0^D R\phi_i dp - \omega R_N \delta_{i,N} \qquad (i = 0 - N) \tag{2.58}$$

The sampling function $\phi_i(p)$ is zero outside the region of $P_{i-1} \leq P \leq P_{i+1}$, eqn. (2.58) is rewritten as eqn. (2.59), (2.60) and (2.61).

$$0 = \tfrac{1}{2}\tfrac{\partial I}{\partial R_0} = -\omega_0 R_0 - \int_0^{p_1} \left(R_0 \tfrac{d\phi_0}{dp} + R_1 \tfrac{d\phi_1}{dp}\right)\tfrac{d\phi_0}{dp} dp$$

$$+v^2 \int_0^{p_1} (q_0\phi_0 + q_1\phi_1)\,(R_0\phi_0 + R_1\phi_1)\phi_0 dp$$

$$-\omega^2 \int_0^{p_1} (R_0\phi_0 + R_1\phi_1)\phi_0 \, dp \tag{2.59}$$

$$0 = \tfrac{1}{2}\tfrac{\partial I}{\partial R_i} = -\int_{p_{i-1}}^{p_i} \left(R_{i-1} \tfrac{d\phi_{i-1}}{dp} + R_i \tfrac{d\phi_i}{dp}\right)\tfrac{d\phi_i}{dp} dp$$

$$-\int_{p_i}^{p_{i+1}} \left(R_i \tfrac{d\phi_i}{dp} + R_{i+1} \tfrac{d\phi_{i+1}}{dp}\right)\tfrac{d\phi_i}{dp} dp$$

$$+v^2 \int_{p_{i-1}}^{p} (q_{i-1}\phi_{i-1} + q_i\phi_i)(R_{i-1}\phi_{i-1} + R_i\phi_i)\phi_i dp$$

$$+v^2 \int_{p_i}^{p_{i+1}} (q_i\phi_i + q_{i+1}\phi_{i+1})(R_i\phi_i + R_{i+1}\phi_{i+1})\phi_i dp$$

$$-\omega^2 \int_{p_{i-1}}^{p_i} (R_{i-1}\phi_{i-1} + R_1\phi_1)\phi_i \, dp$$

$$-\omega^2 \int_{p_i}^{p_{i+1}} (R_i\phi_i + R_{i+1}\phi_{i+1})\phi_i \, dp \qquad (i = 1 - N - 1) \tag{2.60}$$

$$0 = \tfrac{1}{2}\tfrac{\partial I}{\partial R_N} = -\int_{p_{N-1}}^{p_N} \left(R_{N-1} \tfrac{d\phi_{N-1}}{dp} + R_N \tfrac{\phi_N}{dp}\right)\tfrac{d\phi_N}{dp} dp$$

$$+v^2 \int_{p_{N-1}}^{p_N} (q_{N-1}\phi_{N-1} + q_N\phi_N)(R_{N-1}\phi_{N-1} + R_N\phi_N)\phi_N dp$$

$$-\omega^2 \int_{p_{N-1}}^{p_N} (R_{N-1}\phi_{N-1} + R_N\phi_N)\phi_N \, dp - \omega R_N \tag{2.61}$$

The integral of the sample functions – eqn. (2.59), eqn. (2.60) and eqn. (2.61) are given as follows:

$$\int_{p_{i-1}}^{p_i} \frac{d\phi_{i-1}}{dp}\frac{d\phi_i}{dp}\,dp = -\frac{N}{D} \quad \textit{(i=1-N)} \tag{2.62a}$$

$$\int_{p_{i-1}}^{p_i} \left(\frac{d\phi_i}{dp}\right)^2 dp = \frac{N}{D} \quad \textit{(i=1-N)} \tag{2.62b}$$

$$\int_{p_i}^{p_{i+1}} \left(\frac{d\phi_i}{dp}\right)^2 dp = \frac{N}{D} \quad \textit{(i=0-N-1)} \tag{2.62c}$$

$$\int_{p_{i-1}}^{p_i} \phi_{i-1}^2\phi_i dp = \frac{1}{12}\frac{D}{N} \quad \textit{(i=1-N)} \tag{2.62d}$$

$$\int_{p_{i-1}}^{p_i} \phi_{i-1}\phi_i^2 dp = \frac{1}{12}\frac{D}{N} \quad \textit{(i=1-N)} \tag{2.62e}$$

$$\int_{p_{i-1}}^{p_i} \phi_i^3 dp = \frac{1}{4}\frac{D}{N} \quad \textit{(i=1-N)} \tag{2.62f}$$

$$\int_{p_i}^{p_{i+1}} \phi_i^3 dp = \frac{1}{4}\frac{D}{N} \quad \textit{(i=0-N-1)} \tag{2.62g}$$

$$\int_{p_{i-1}}^{p_i} \phi_{i-1}\phi_i dp = \frac{1}{6}\frac{D}{N} \quad \textit{(i=1-N)} \tag{2.62h}$$

$$\int_{p_{i-1}}^{p_i} \phi_i^2 dp = \frac{1}{3}\frac{D}{N} \quad \textit{(i=1-N)} \tag{2.62i}$$

$$\int_{p_i}^{p_{i+1}} \phi_i^2 dp = \frac{1}{3}\frac{D}{N} \quad \textit{(i=0-N-1)} \tag{2.62j}$$

By substituting eqn. (2.62) into eqn. (2.59), (2.60) and (2.61), we will obtain new relations as follows:

$$0 = -\frac{1}{2}\frac{D}{N}\frac{\partial I}{\partial R_0} = R_0\left\{1-(3q_0+q_1)\frac{v^2}{12}\left(\frac{D}{N}\right)^2+\frac{\omega^2}{3}\left(\frac{D}{N}\right)^2+w_0\frac{D}{N}\right\}$$

$$+R_1\left\{-1-(q_0+q_1)\frac{v^2}{12}\left(\frac{D}{N}\right)^2+\frac{\omega^2}{6}\left(\frac{D}{N}\right)^2\right\} \quad (2.63)$$

$$0 = -\frac{1}{2}\frac{D}{N}\frac{\partial I}{\partial R_i} = R_{i-1}\left\{-1-(q_{i-1}+q_i)\frac{v^2}{12}\left(\frac{D}{N}\right)^2+\frac{\omega^2}{6}\left(\frac{D}{N}\right)^2\right\}$$

$$+R_i\left\{2-(q_{i-1}+6q_i+q_{i+1})\frac{v^2}{12}\left(\frac{D}{N}\right)^2+\frac{2\omega^2}{3}\left(\frac{D}{N}\right)^2\right\}$$

$$+R_{i+1}\left\{-1-(q_i+q_{i+1})\frac{v^2}{12}\left(\frac{D}{N}\right)^2+\frac{\omega^2}{6}\left(\frac{D}{N}\right)^2\right\} \quad \textit{(i=1-N-1)} \quad (2.64)$$

$$0 = -\frac{1}{2}\frac{D}{N}\frac{\partial I}{\partial R_N} = R_{N-i}\left\{-1-(q_{N-1}+q_N)\frac{v^2}{12}\left(\frac{D}{N}\right)^2+\frac{\omega^2}{6}\left(\frac{D}{N}\right)^2\right\}$$

$$+R_N\left\{1-(q_{N-1}+3q_N)\frac{v^2}{12}\left(\frac{D}{N}\right)^2+\frac{\omega^2}{3}\left(\frac{D}{N}\right)^2+\omega\frac{D}{N}\right\} \quad (2.65)$$

The eqn. (2.63), (2.64) and (2.65) are a set of *(N+1)* order simultaneous equations having $R_0 - R_N$ as the unknown. To make the eqn. (2.63), (2.64) and (2.65) have nontrivial solution except for $R_0 = R_1 = \cdots = R_N = 0$, the determinant of the matrix C have to be zero.

$$\det(C) = 0 \quad (2.66)$$

The matrix C is transformed from the eqn. (2.63), (2.64) and (2.65), it is shown as below:

$$C_{0,0} = 1-(3q_0+q)\frac{v^2}{12}\delta^2+\frac{\omega^2}{3}\delta^2+\omega_0\delta \quad (2.67a)$$

$$C_{i,i} = 2-(q_{i-1}+6q_i+q_{i-1})\frac{v^2}{12}\delta^2+\frac{2\omega^2}{3}\delta^2 \quad \textit{(i=1-N-1)} \quad (2.67b)$$

$$C_{i,i+1} = C_{i+1,i} = -1-(q_i+q_{i+1})\frac{v^2}{12}\delta^2+\frac{\omega^2}{6}\delta^2 \quad \textit{(i=0-N-1)} \quad (2.67c)$$

$$C_{N,N} = 1-(q_{N-1}+3q_N)\frac{v^2}{12}\delta^2+\frac{\omega^2}{3}\delta^2+\omega\delta \quad (2.67d)$$

where discretization step δ is given by:

$$\delta = \left(\frac{D}{N}\right) \quad (2.68)$$

Eqn. (2.66) is the dispersion or eigenvalue equation for the TE-mode in an arbitrary refractive index profile. When the distribution of refractive index $q(p)$ and normalized frequency v are given, the propagation constant β (contained in ω and ω_0) can be calculated from eqn. (2.66) and eqn. (2.67). We can get the cutoff v-value of the waveguide from the solution of eqn. (2.66) by setting the $\omega = 0$ ($\beta = kn_s$) in eqn. (2.67). The TM-modes analysis is similar to the above steps, so it will not be discussed.

2.4.5 Summary

To conclude, FEM is a power tool in mode analysis for optical waveguide with arbitrary refractive index profile and complicated structures. To date, scientists, researchers, and engineers have been using FEM to conduct research and develop innovative products in a variety of field of studies. A wide range of photonics devices can be modelled using FEM, such as photonics crystal cavities, waveguide interferometer, plasmonic waveguide, etc. In this work, simulation using FEM is first carried out to perform mode analysis on planarized optical waveguide. Also, the effect of a dielectric thin film coating on planarized optical waveguide is studied. The results obtained from simulation will be discussed on next chapter.

CHAPTER 3: OPTICAL CHARACTERISTIC OF THIN FILM COATED PLANARIZED OPTICAL WAVEGUIDE

3.1 Introduction

The FEM software used to simulate the optical characteristic of planarized optical waveguide with or without thin film coating is COMSOL Multiphysics, specifically the Wave Optics Module. The Wave Optics Module has extended the physics user interfaces function of the base package for COMSOL Multiphysics. It can be used to solve electromagnetic waves problem at optical frequencies, which corresponds to the micro- to nano-meter wavelength range. This module is capable of designing and running simulation on a variety of optical applications involving electromagnetic waves, such as optical fibers, photonics waveguides, photonics crystals, laser resonator, nonlinear optics, etc. Compared to the RF module which can also handle electromagnetic wave simulation at high frequency, the Wave Optics Module has the advantage of performing time-harmonic simulations of domains which are much larger than the wavelength. This situation is common among optical phenomena, optical systems and components. The interaction length between electromagnetic wave and optical material is usually much larger than the wavelength due to their weak coupling, which applies to linear coupler such as Fiber Bragg Grating, directional couplers, etc. With the aid of Wave Optics Module, these types of problems can be directly addressed without the demand of huge computer memory.

In the Wave Optics Module, there are generally four types of physics user interface under “Electromagnetic Waves”, which are Beam Envelopes, Frequency Domain, Time Explicit and Transient. The Time explicit and Transient methods can be used to solve problems that have variation in time. However, in this case, we treat the electromagnetic

problem as time-harmonic in the frequency domain since we are using continuous wave (CW) light source in this work. Therefore, the Frequency Domain and Beam Envelopes methods are used. It allows us to simplify the analysis by assuming that all time variation occurs as sinusoidal waveform, making it possible to formulate it as stationary problem with complex valued solutions. The complex values represent the phase and amplitude of an electromagnetic field, while the frequency will be a scalar model input. One of the typical frequency domain simulation is the wave propagation problems. Although both the Frequency Domain and Beam Envelopes methods can be used to solve for time-harmonic Maxwell's equations, they still possess their own advantage over each other. For Frequency Domain method, it is very flexible in solving both wave propagation and scattering problems, as long as the mesh element size is a fraction of the input wavelength. On the other hand, in many optical application, the propagation length is often much longer than the wavelength (e.g. 1 μm optical wavelength propagates in devices with mm to cm in length). It would take a huge amount of computer memory to solve for this kind of problems using Frequency Domain method. The Beam Envelopes method in turn can solve this type of problem without the need of large memory, by assuming a slow varying amplitude factor and rapid changing phase factor. However, as the waveguide structure used in this work is invariant along the wave propagation direction, performing simulations on the waveguide cross section, which is a 2D space dimension, is sufficient. Therefore, Frequency Domain method is used to simulate the propagation mode of planarized optical waveguide in this work.

3.2 Electromagnetic Waves - Frequency Domain method

The Frequency Domain method applies Maxwell's partial differential equations (PDE) to solve for the electromagnetic problems. The FEM simulation is based on four steps, as described in detail in Chapter 2. The first step is to discretize the domain of interest into

thousands of identical shapes (usually triangle), but of different sizes, called finite mesh element. These finite mesh element can be defined as 1D, 2D or 3D depending on the domain of interest of the optical object. Moreover, the meshing can be generated uniformly or non-uniformly based on the requirement of the situation. For important regions in the domain of interest where the parameters under study vary rapidly (at a waveguide core-cladding interface, for example), it is preferable to concentrate many small finite elements in these regions than other regions. The second step is to derive the governing Maxwell's PDE in each finite element of the mesh. After that, the third step is to assemble all the finite elements in the domain of interest. Finally, the general solution of the electromagnetic problem can be obtained by solving all the equations under the right boundary condition.

3.3 Waveguide Structure

The proposed planarized optical waveguide structure in this work is shown in Figure 3.1. The refractive index of the core, side cladding, undercladding and air are set to 1.486, 1.44, 1.444 and 1.0 respectively, with reference to the values of a 3.0% index contrast silica optical waveguide. These layers are assumed to be lossless – the imaginary part of complex refractive index is zero. A thin film is coated on top of the waveguide core, represented by the red dash line in Figure 3.1. The range of optical constants for the thin film coating is determined by the values of a variety of 2D material (graphene, GO, molybdenum disulfide and black phosphorus) at 1550 nm that are obtained from (Bullock et al., 2018; Kravets et al., 2015; Li et al., 2018; Li et al., 2017; Samassekou et al., 2017; Schöche et al., 2017; Ullah et al., 2018; Xu, 2018; Zheng, 2016). Thus, the real part of complex refractive index of 2D material (n_{2D}) ranges from 1.5 to 3.5, while the range of imaginary part of complex refractive index (k_{2D}) studied is 0.01 to 1.5. The coating

thicknesses of 2D material (t_{2D}) is set to 0.5 nm, 2.0 nm and 5.0 nm, which represents monolayer, few-layer and multilayer coatings, respectively.

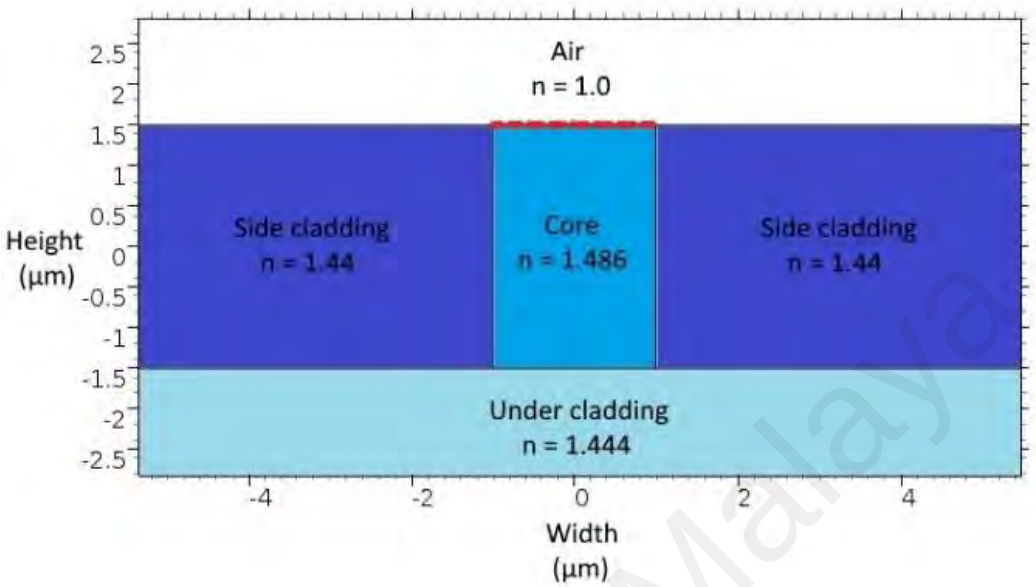

Figure 3.1: Schematic diagram of the cross-sectional part of the planarized optical waveguide

3.4 Modelling Procedure

COMSOL Multiphysics software is used to model the planarized optical waveguide (with and without thin film coating) to find their corresponding guided modes for both TE- and TM-polarized light. The mesh node formed in the domain of interest of the planarized optical waveguide with and without thin film coating are shown in Figure 3.2. It can be seen that the meshing used in designing the planarized optical waveguide coated with thin film is non-uniform, where highly dense mesh node is formed within and around the narrow regions of thin film overlay. It is because higher accuracy is required to solve for the variation of Maxwell's wave equation in each of the finite element over the densely meshed region.

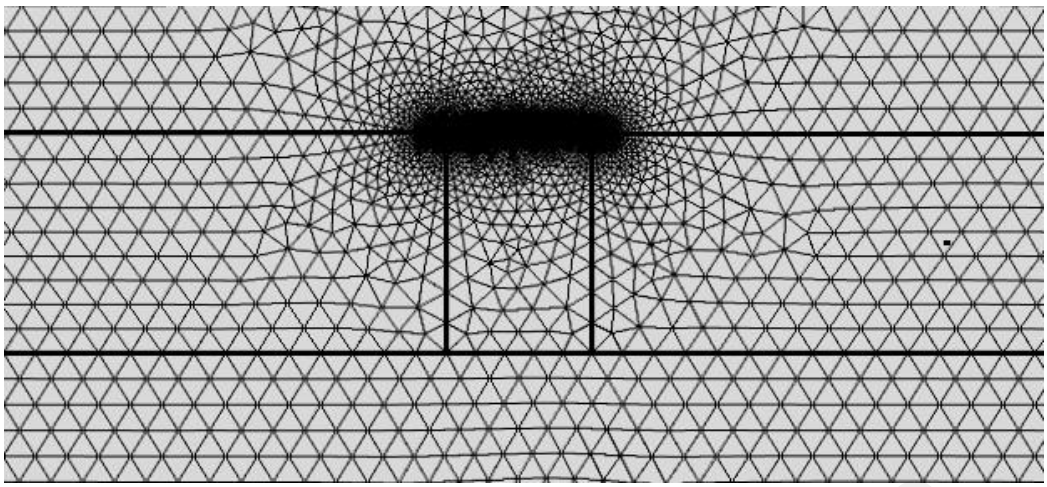

(a)

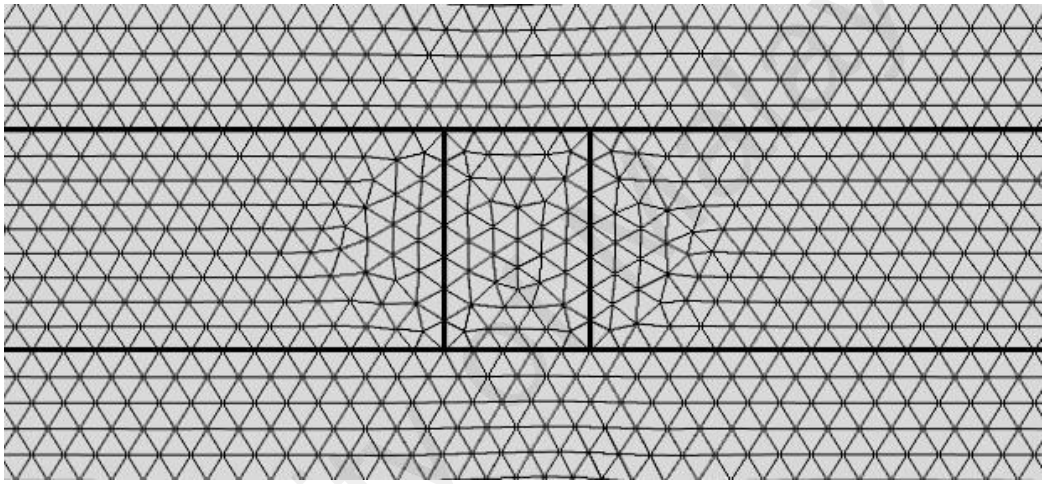

(b)

Figure 3.2: Mesh node formed in planarized optical waveguide (a) with and (b) without thin film coating

COMSOL Multiphysics solve the electromagnetic fields within the modeling domains under the assumption that the electric fields oscillates sinusoidally at certain frequency and all material properties are linear with respect to the field strength, the governing Maxwell's equations in three dimensions will be reduced to equation (3.1),

$$\nabla \times (\nabla \times E) - {k_0}^2 \varepsilon_r E = 0 \qquad (3.1)$$

where E is electric field (V/m), ε_r is relative permittivity and k_0 is the wavenumber in vacuum. The relative permittivity can further relate to the optical properties of material as shown as below,

$$\varepsilon_r = (n - ik)^2 \tag{3.2}$$

where n and k are the real part and imaginary part of complex refractive index of the material, respectively. These values will then be incorporated into the numerical model to compute the propagation modes which are supported by the optical waveguide and their corresponding effective mode index. The effective mode index is the complex function of the waveguide. The real part (n_{eff}) determine how much phase shift is induced on a particular waveguide mode, whereas the imaginary part (k_{eff}) provides information about the propagation loss experienced by the waveguide mode.

3.5 Simulation Results

3.5.1 Waveguide dimension tolerance for single and higher order mode operation

In this work, the waveguide dimension needs to be controlled to allow only the excitation of the fundamental mode at the wavelength of interest of 1550 nm so as to achieve mode analysis with higher accuracy using a shorter simulation duration. As a result, the waveguide dimension tolerance test of single mode operation is first carried out. The effect of core width on single and higher order mode operation of planarized optical waveguide, given that the height of core is fixed at 3 μm, is shown in Figure 3.3. The effective index of the fundamental and higher order TE- and TM-mode as the function of waveguide core width is obtained. It can be observed that the cut-off core width for single mode operation is at around 4 μm, which means that to maintain single mode light propagation, the fabricated planarized optical waveguide should a core width of smaller than 4 μm when the core height is 3 μm. After weighing up other factors, the

planarized optical waveguide with 2 μm width and 3 μm height is considered the suitable dimension to carry out the experiment, with the advantages of single mode operation, small NA and mode field diameter mismatch with input/output fiber used for butt-coupling process in the optical characterization part of experiment. The effective mode index of planarized optical waveguide with core dimension of 2 μm width and 3 μm height is 1.4561 and 1.4558 for TE- and TM-polarized light, respectively. The imaginary part of the effective mode index is zero because these materials are assumed to be lossless.

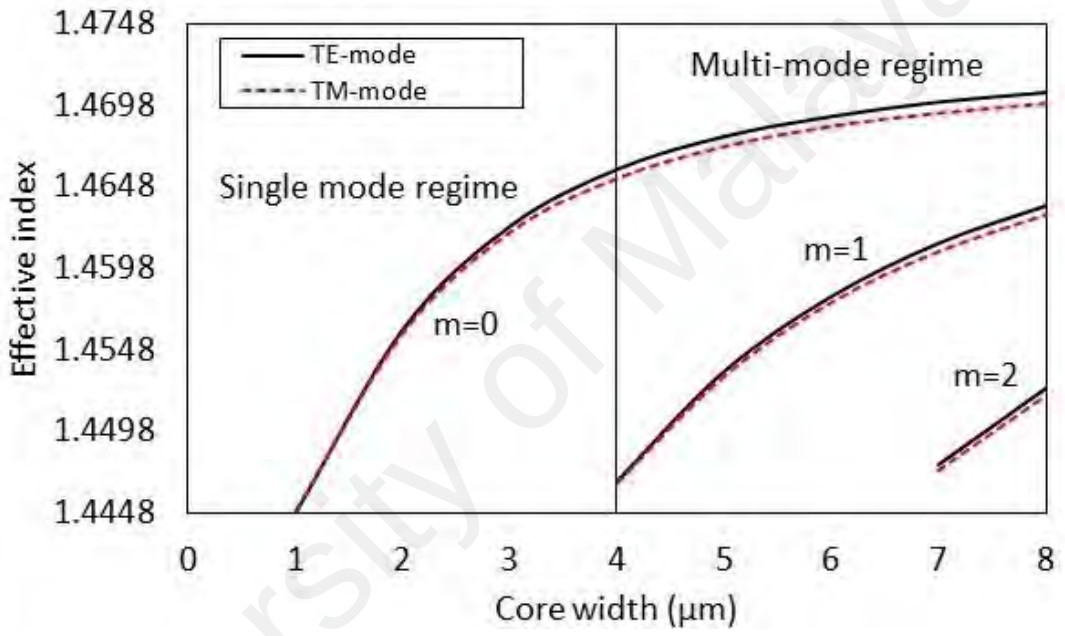

Figure 3.3: The effect of core width on single/higher order mode operation of planarized optical waveguide

3.5.2 Effect of thin film coating

This section shows the simulation results of planarized optical waveguide coated with thin film that has a varying complex refractive index and thickness. The change in n_{eff} of TE-polarized light with n_{2D}, k_{2D} and t_{2D} is shown in Figure 3.4. It can be seen that n_{eff} increases when n_{2D} is increased but decreases slightly with the increase of k_{2D}. In Figure 3.4(b), where t_{2D} is 2.0 nm, n_{eff} increases by 8.08×10^{-5} when n_{2D} is varied from 1.5 to 3.5 and with k_{2D} set at the minimum value of 0.01. When k_{2D} is set at 1.5, n_{eff} increases by a

smaller magnitude of 7.38x10^{-5} for the same variation of n_{2D}. The decrease in n_{eff} with larger k_{2D} is due to the slight decrease of mode field distribution in the waveguide core. On the other hand, n_{eff} changes by a larger magnitude with variation of n_{2D} and k_{2D} for thicker t_{2D}, which can be seen by comparing the contour gradient between Figure 3.4(a), 3.4(b) and 3.4(c). The increase in n_{eff} with variation of n_{2D} is close to one order of magnitude larger (2.25x10^{-4} compared to 1.92x10^{-5}) when t_{2D} is increased from 0.5 nm to 5.0 nm (for k_{2D} = 0.01). This can be attributed to the enhancement of evanescent field interaction between the waveguide mode and 2D material when the coating thickness is increased.

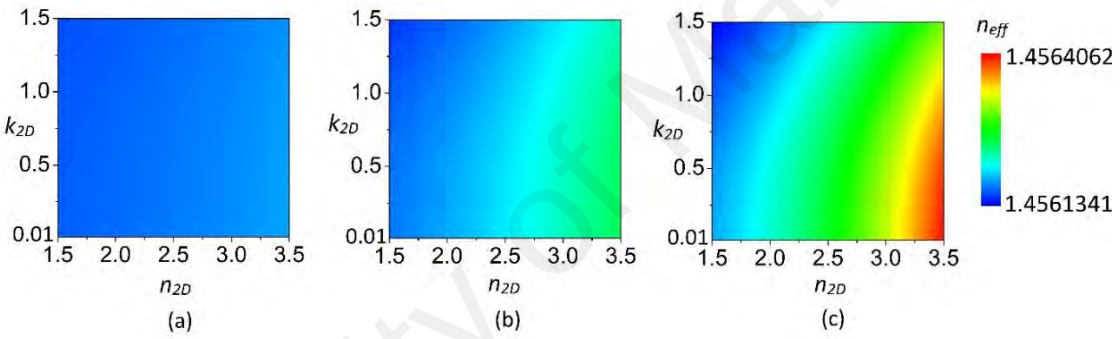

Figure 3.4: n_{eff} of the 2D material coated planarized optical waveguide for TE-mode corresponding to different n_{2D} and k_{2D} for t_{2D} at (a) 0.5 nm, (b) 2.0 nm and (c) 5.0 nm

The effect of n_{2D} and k_{2D} on k_{eff} of the 2D material coated planarized waveguide is shown in Figure 3.5. In this case, k_{eff} is proportional to both n_{2D} and k_{2D}. For t_{2D} of 2.0 nm, it can be seen that k_{eff} increases by 3.73x10^{-7} when n_{2D} is varied from 1.5 to 3.5 and k_{2D} fixed at 0.01, as shown in Figure 3.5(b). Larger n_{2D} will result in greater interaction of light with the 2D material coating, which leads to higher k_{eff} and corresponding increase in propagation loss. When k_{2D} is set at 1.5, k_{eff} increases by a much larger magnitude of 5.39x10^{-5} for the same variation of n_{2D}, which is more than 2 orders of magnitude higher compare to the increase in k_{eff} when k_{2D} is 0.01. This implies that k_{2D} have a more significant effect on the change in k_{eff} compared to n_{2D}. Similar to Figure 3.4, comparison

between Figure 3.5(a), 3.5(b) and 3.5(c) indicates that the change in k_{eff} with both n_{2D} and k_{2D} will become more significant when the 2D material thickness is increased. The change in k_{eff} with variation of n_{2D} increases from 1.19x10^{-5} to 1.69x10^{-4} when the t_{2D} increases from 0.5 nm to 5.0 nm (for k_{2D} = 1.5).

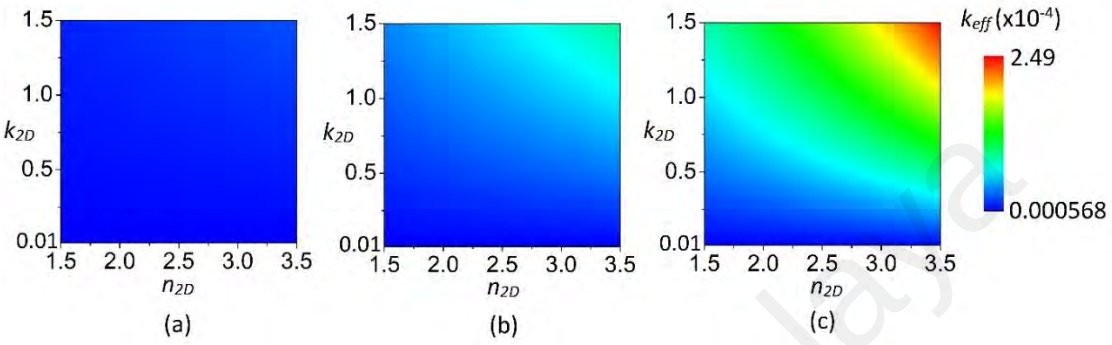

Figure 3.5: k_{eff} of the 2D material coated planarized optical waveguide for TE-mode corresponding to different n_{2D} and k_{2D} for t_{2D} at (a) 0.5 nm, (b) 2.0 nm and (c) 5.0 nm

TM-polarized light propagation characteristics in the 2D material coated waveguide are similar to that of TE-polarized light, as shown in Figure 3.6 and Figure 3.7. However, the magnitude of change of n_{eff} and k_{eff} for TM-polarized light is smaller compared to TE-polarized light. For fixed values of t_{2D} = 2.0 nm and k_{2D} = 0.01, the change of n_{eff} with n_{2D} for TM-polarized light decreases from 8.08x10^{-5} to 4.97x10^{-5} when compared to TE-polarized light. Likewise, the change in k_{eff} with n_{2D} for TM-polarized light is reduced by half (from 5.39x10^{-5} to 2.62x10^{-5}) when compared to TE-polarized light (for t_{2D} = 2.0 nm and k_{2D} = 1.5). The smaller magnitude of change in both n_{eff} and k_{eff} is due to the weaker coupling of TM-polarized light into the 2D material overlay when compared to TE-polarized light.

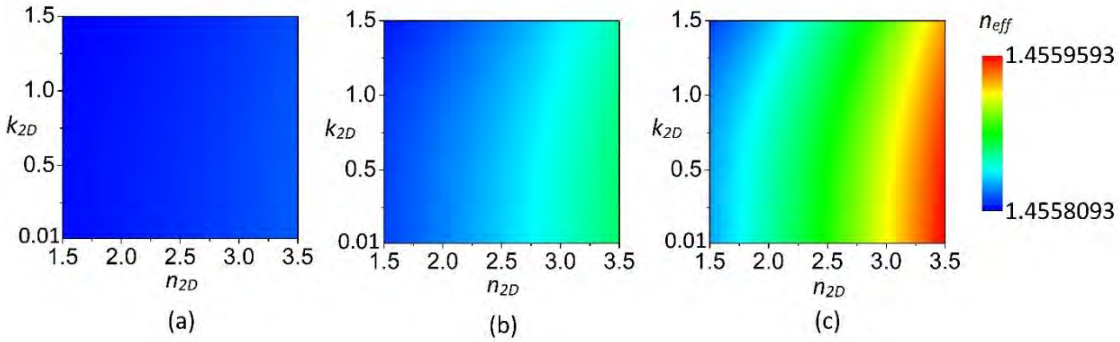

Figure 3.6: n_{eff} of the 2D material coated planarized optical waveguide for TM-mode corresponding to different n_{2D} and k_{2D} for t_{2D} at (a) 0.5 nm, (b) 2.0 nm and (c) 5.0 nm

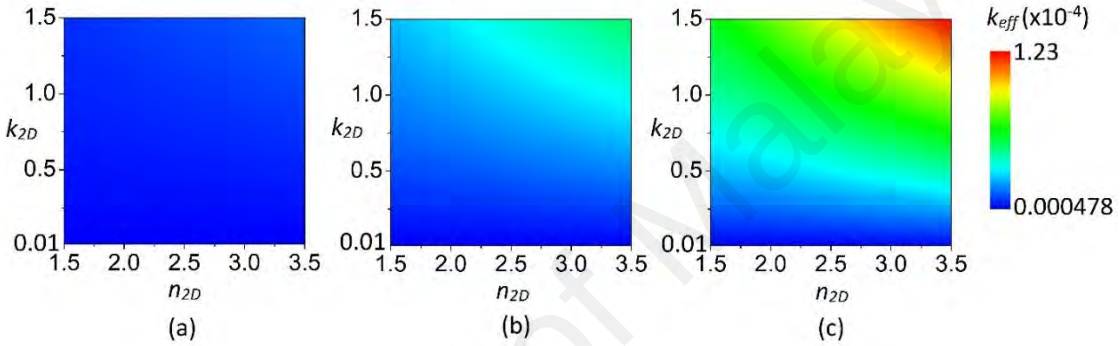

Figure 3.7: k_{eff} of the 2D material coated planarized optical waveguide for TM-mode corresponding to different n_{2D} and k_{2D} for t_{2D} at (a) 0.5 nm, (b) 2.0 nm and (c) 5.0 nm

3.5.3 Potential

Based on the results above, it can be seen that 2D materials with intrinsic birefringence significantly change the effective mode index of the planarized optical waveguide. This characteristics enable us to determine the anisotropic complex refractive index of a thin film overlay by analyzing its distinct polarization response on planarized optical waveguide. Other than that, it also allow us to design and develop a compact waveguide polarizer by optimizing the coating thickness of the thin film. Among the 2D materials being studied, BP and GO show potential as the functional optical material for in-plane waveguide polarizer due to their large anisotropic optical properties. The optical constants of BP when oriented in armchair direction are approximately $2.6+0.55i$ and $1.7+0.001i$ for TE- and TM-polarized lights, respectively (Bullock et al., 2018). On the other hand,

the optical constants of GO for TE- and TM-polarized light are approximately 1.76+0.03*i* and 1.53+0.01*i*, respectively (Schöche et al., 2017). By extending the coating thickness dependent analysis, an optimized coating thickness where maximum polarization extinction ratio (PER) occurs can be determined. As shown in Figure 3.8, while k_{eff} of TM-polarized light remains low with the increase of coating thickness, it increases significantly for TE-polarized light. As k_{eff} is proportional to the insertion loss, a large different in k_{eff} between TE- and TM-polarized lights will result in very large PER. It can also be seen that the coating thickness where the largest difference in k_{eff} between TE- and TM-polarized lights is achieved depends on the optical constants of the coating material.

The insertion loss and polarization extinction ratio (PER) for BP and GO coated planarized optical waveguides are summarized in Table 3.1 and 3.2. For consideration of a compact footprint, the coating length is set at 1 mm. In Table 3.1, a BP-coated waveguide polarizer with PER of 78.5 dB and a low insertion loss of only 0.024 dB can be produced with 60 nm of coating thickness with the BP oriented in armchair direction toward the incident light. On the other hand, as shown in table 3.2, a GO-coated waveguide polarizer with GO coating thickness of 275 nm exhibits an even larger PER of 97.7 dB, but with a relatively higher insertion loss penalty of 1.9 dB. The 10-dB PER tolerance for BP-coated planarized optical waveguide is around ±10 nm, whereas for GO-coated planarized optical waveguide, the same tolerance is about ±25 nm. These thickness tolerances are well within the capability of current coating technologies. Therefore, waveguide polarizer with superior performances can be produced using a planarized waveguide structure coated with BP as well as GO with controlled coating thickness.

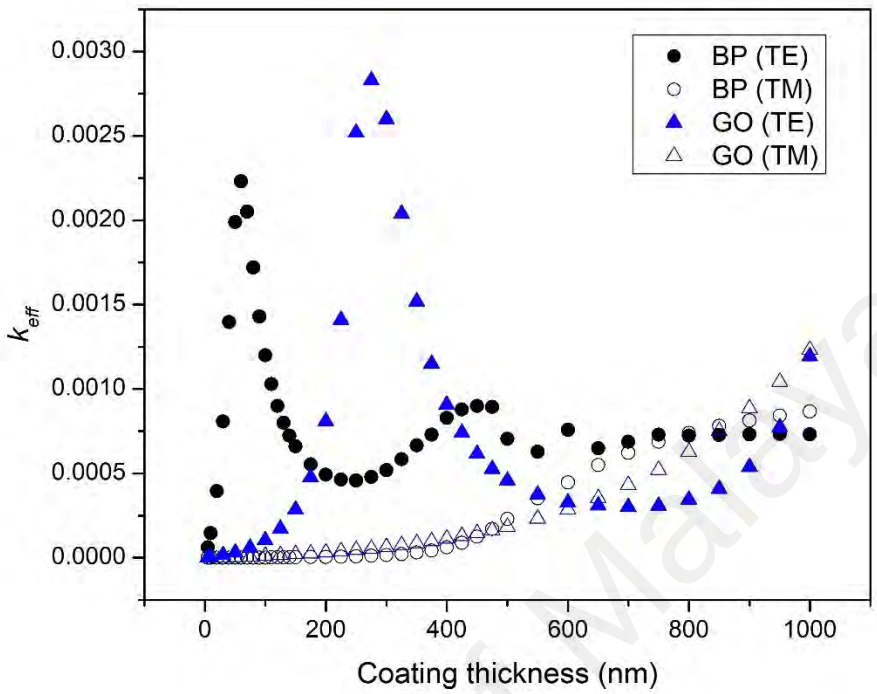

Figure 3.8: k_{eff} of BP- and GO-coated planarized optical waveguide versus coating thickness for TE- and TM-polarised light

Table 3.1: Insertion loss and PER of BP-coated planarized optical waveguide TM-pass polarizer

Coating thickness (nm)	Insertion loss BP-coated waveguide (dB)	PER (dB)
30	0.011	28.4
40	0.015	49.1
50	0.019	70.0
60	0.024	78.5
70	0.029	72.2
80	0.035	60.5
90	0.041	50.3

Table 3.2: Insertion loss and PER of GO-coated planarized optical waveguide TM-pass polarizer

Coating thickness (nm)	Insertion loss GO-coated waveguide (dB)	PER (dB)
200	1.1	27.4
225	1.4	48.3
250	2.3	86.4
275	1.9	97.7
300	2.2	89.2
325	2.6	69.2
350	4.1	49.3

3.6 Summary

The light propagation characteristics of planarized optical waveguide with and without thin film overlay coating have been studied using numerical approach. In the waveguide dimension tolerance analysis for single mode operation, it is found that, based on the optical properties of silica waveguide material, planarized optical waveguide with 2 μm width and 3 μm height is the suitable dimension to be used for the works in Chapter 4, with the advantages of single mode operation, small NA and mode field diameter mismatch with input/output fiber used for butt-coupling process during the optical characterization experiment. Besides, the simulation results also show that the effective mode index of planarized optical waveguide is highly dependent on the thickness of thin film coating. In addition, n_{eff} increases with the increase of refractive index of the thin film overlay but decreases with its extinction coefficient, while k_{eff} increases with the increase of both refractive index and extinction coefficient of the thin film overlay. Lastly, by extending the coating thickness analysis, it is found that using the anisotropic optical properties of BP and GO together with the planarized waveguide structure, an in-plane

TM-pass waveguide polarizer with very large PER and low insertion loss can be produced by optimizing their coating parameters.

CHAPTER 4: DETERMINATION OF ANISOTROPIC COMPLEX REFRACTIVE INDEX OF GRAPHENE OXIDE AT 1550 NM

4.1 Introduction

As mentioned earlier, studies of the complex refractive index of GO reported so far still has a large deviation from each other. The *n* values of GO was reported to be in the range of 1.8 – 1.9, while *k* values are in the range of 0.1 – 0.8, at wavelength of 600 nm (Jung et al., 2008; Shen et al., 2011). At the wavelength of 1550 nm, the reported complex refractive index of GO have even larger range, which are 1.5 – 2.1 and 0.01 – 0.25 for *n* and *k*, respectively (Kravets et al., 2015; Schöche et al., 2017). This Chapter will attempt to determine the complex refractive index of GO using a novel approach, which is through the study and analysis of optical response of GO-coated planarized optical waveguide.

From the simulation results obtained in Chapter 3, it can be seen that the polarization response of planarized optical waveguide is notably high to the integration of thin film overlay. Thus, it is capable of determining the anisotropic complex refractive index of GO coated on top of it, by making careful experimental measurements and cross referencing with finite element analysis for the effective mode index of the GO-coated waveguide. Following the completion of simulation work, an experiment of measuring the propagation loss-to-coating thickness profile of GO-coated planarized optical waveguide is carried out. In this chapter, the fabrication of planarized optical waveguide, GO coating method, simulation model specific to the fabricated GO-coated waveguide, and optical characterization of GO-coated waveguide will first be discussed. Then, cross-referencing between experimental and simulation data will be carried out to determine the complex refractive index of GO thin film. Finally, the uncertainties of this determination method will be discussed.

4.2 Fabrication of Germanium-doped Silica Planarized Optical Waveguide

Flame hydrolysis deposition (FHD) is carried out to deposit a silica core layer on silicon substrate covered by thermal oxide layer with 7 μm thickness, which involves the hydrolysis of metal halides like silicon tetrachloride, germanium tetrachloride or boron trichloride into chemical flame to form oxide soot. In this case, germanium tetrachloride is used as the metal halides source for hydrolysis. By adjusting the process parameter, the germanium-doped (GD) silica layer with 1.486 refractive index and 3 μm thickness is formed on top of the silicon substrate. Then the propagation loss of the GD silica layer is examined using prism coupler, and the results show that its propagation loss is less than 0.2 $dB.mm^{-1}$ at 1550nm. After that, the GD silica layer can be made into straight channel waveguide through photolithography and plasma etching process. Spin-coating of ZPU13 polymer with refractive index of 1.44 measured at 1550 nm on the GD silica waveguide as overcladding, followed by oxygen plasma etching to etch down the ZPU13 polymer until it reaches the top of the silica core. Finally, a planarized optical waveguide with straight channel structure is produced.

A Scanning Electron Microscope image of the planarized optical waveguide with straight channel structure is shown in Figure 4.1. The image shows that the ZPU13 polymer is slightly over-etched, while the surface quality of the GD silica core and the ZPU13 polymer side cladding turn out to be very good. Despite the overall good fabrication quality of the optical waveguide, the over-etched part of the ZPU13 polymer still indicates that it is actually a waveguide with a slightly protruding core instead of a perfectly planarized waveguide. By using surface profiling machine (Veeco DEKTAK D150), the height of the protrusion of GD silica core is found to be in the range from 0.5 μm to 0.9 μm which constitutes around 16% to 30% of the total height of core. To ensure that Finite Element Analysis is carried out as accurate as possible, this actual profile of

the cross section of the planarized optical waveguide will be used in the analysis, as discussed in Section 4.4.

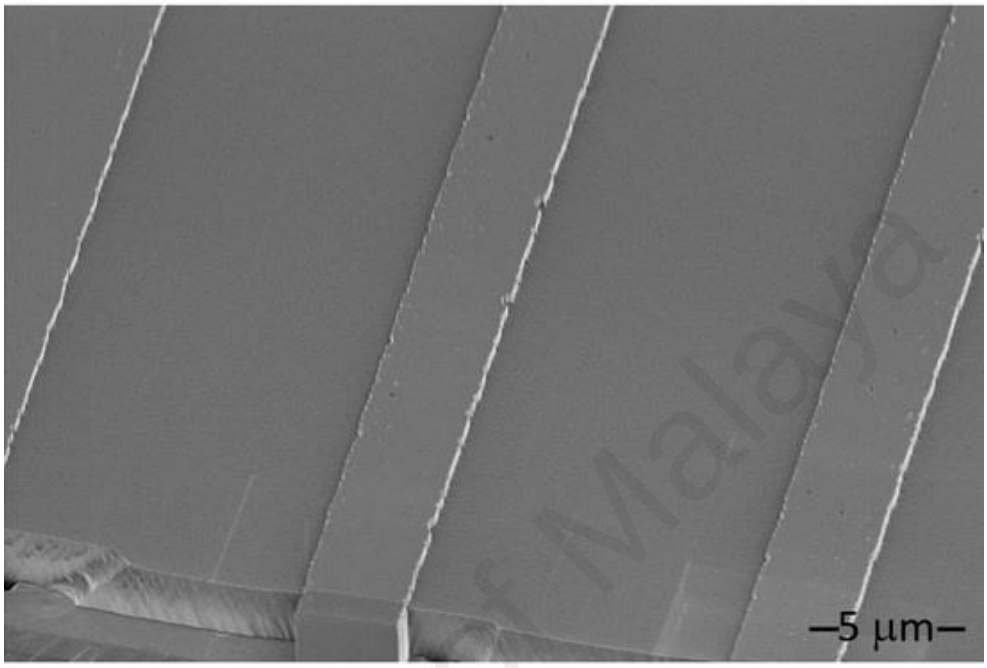

Figure 4.1: SEM image of the planarized silica waveguide with straight channel structure

4.3 Graphene Oxide Coating

GO is fabricated using modified Hummer's method (Hummers & Offeman, 1958), which a graphite is firstly oxidized by potassium permanganate ($KMnO_4$) and sulphuric acid to form graphite oxide, then it will be further exfoliated in de-ionized water via ultrasonication, finally producing GO flake with only single or few layers. The concentration of the produced GO solution is initially 12 µg/µl, then it is diluted by adding unequal volume of de-ionized water to several different lower concentration: 1.6 µg/µl, 2.0 µg/µl, 3.0 µg/µl and 4.0 µg/µl. The GO solution is drop-casted on planarized waveguide using micropipette, it is allowed to dry naturally under room temperature and ambient atmospheric condition. Each GO droplet must be dried completely (normally in

20 to 30 minutes) before the next drop of GO is casted on top of the dried GO coating. The concentration and number of drops of GO solution is varied to get the different coating thickness of GO layer, in order to study the light propagation in planarized optical waveguide coated by multilayer GO with different thicknesses. The coating thickness of GO versus different concentration for single drop of GO is shown in Figure 4.2, while the coating thickness of GO versus number of drops of GO for concentration of 1.6 μg/μl is shown in Figure 4.3.

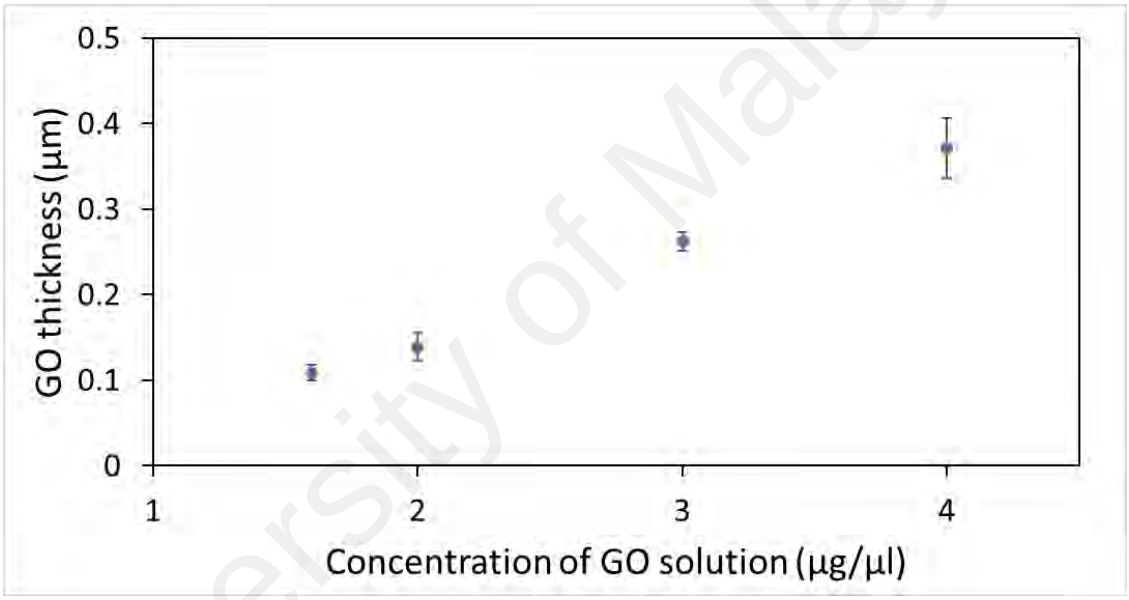

Figure 4.2: The coating thickness of GO versus different concentration for single drop of GO.

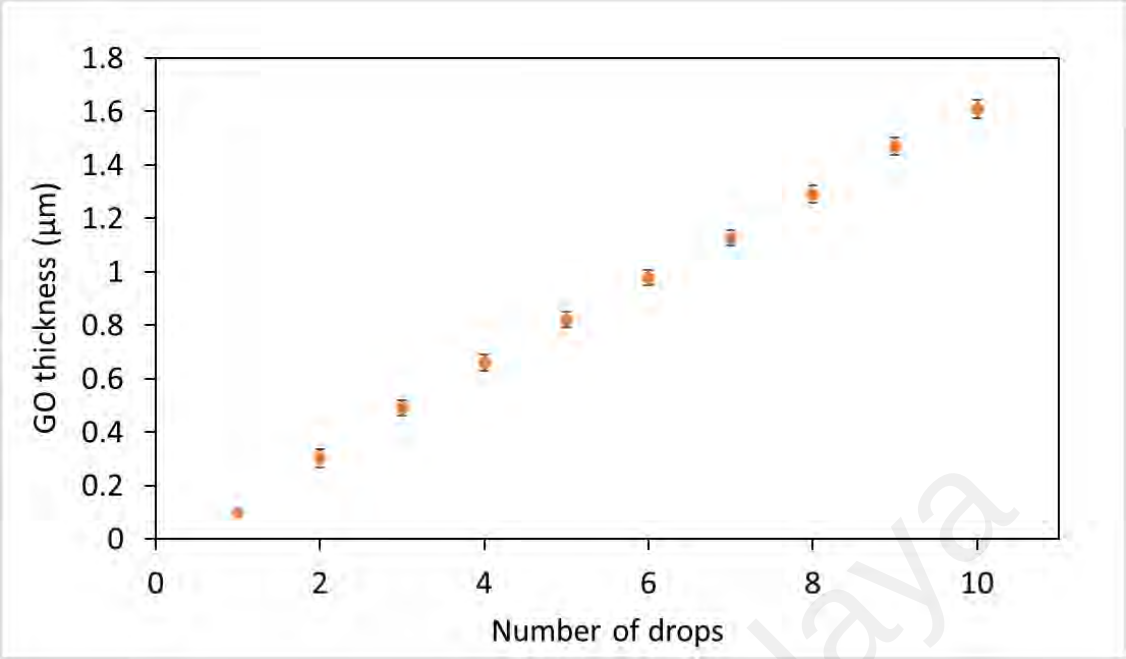

Figure 4.3: The coating thickness of GO versus number of drops of GO for concentration of 1.6 µg/µl.

4.4 Simulation Model of GO-coated Planarized Optical Waveguide

This optical characteristic of GO-coated waveguide with different GO coating thicknesses can be described by the mode field distributions of the 1550 nm light in waveguides. In order to achieve a more accurate cross-referencing, the actual structure of the GO-coated waveguide have to be obtained. The microscope image in Figure 4.4(a) shows the cleaved cross-section of the fabricated planarized optical waveguide. It can be observed that both the side walls of waveguide core are slanted. Details of the waveguide include air gap which is formed between the GO sheet and the protruded section of waveguide core is captured by the field-emission scanning electron microscope (FESEM) image and shown in Figure 4.4(b). Finite element method (FEM) is used for modal analysis and the structure model is shown in Figure 4.4(c). The GO-coated waveguide's height is set to 3 µm. The top and bottom surface width are set to 1.9 µm and 2.8 µm, respectively, as measured by the microscope scaling. The refractive indices of different regions of the waveguide structure are obtained from prism coupling measurement during

the fabrication processes. The protrusion of the waveguide core used in experiment is measured using surface profiler, it is found to be 0.8 μm – and this value is used in the analysis. The air gaps formed between the GO sheet and side cladding with a spacing of 0.5 μm at the base is considered in the simulation. The wavelength of signal used is 1550 nm. The variables in this analysis are the GO coating thickness and its complex refractive index. GO coating thickness is varied from 0.1 μm to 1.0 μm. On the other hand, the complex refractive index of GO was first measured using spectroscopic ellipsometry (J. A. Wollam M-2000) to be 1.655+0.02i. Together with the value reported by Stefan et al (Schöche et al., 2017), a range of complex refractive index values of GO are used in the simulation. The real part of refractive index of GO is varied from 1.50 to 1.80, whereas the imaginary part is varied from 0.001 to 0.2.

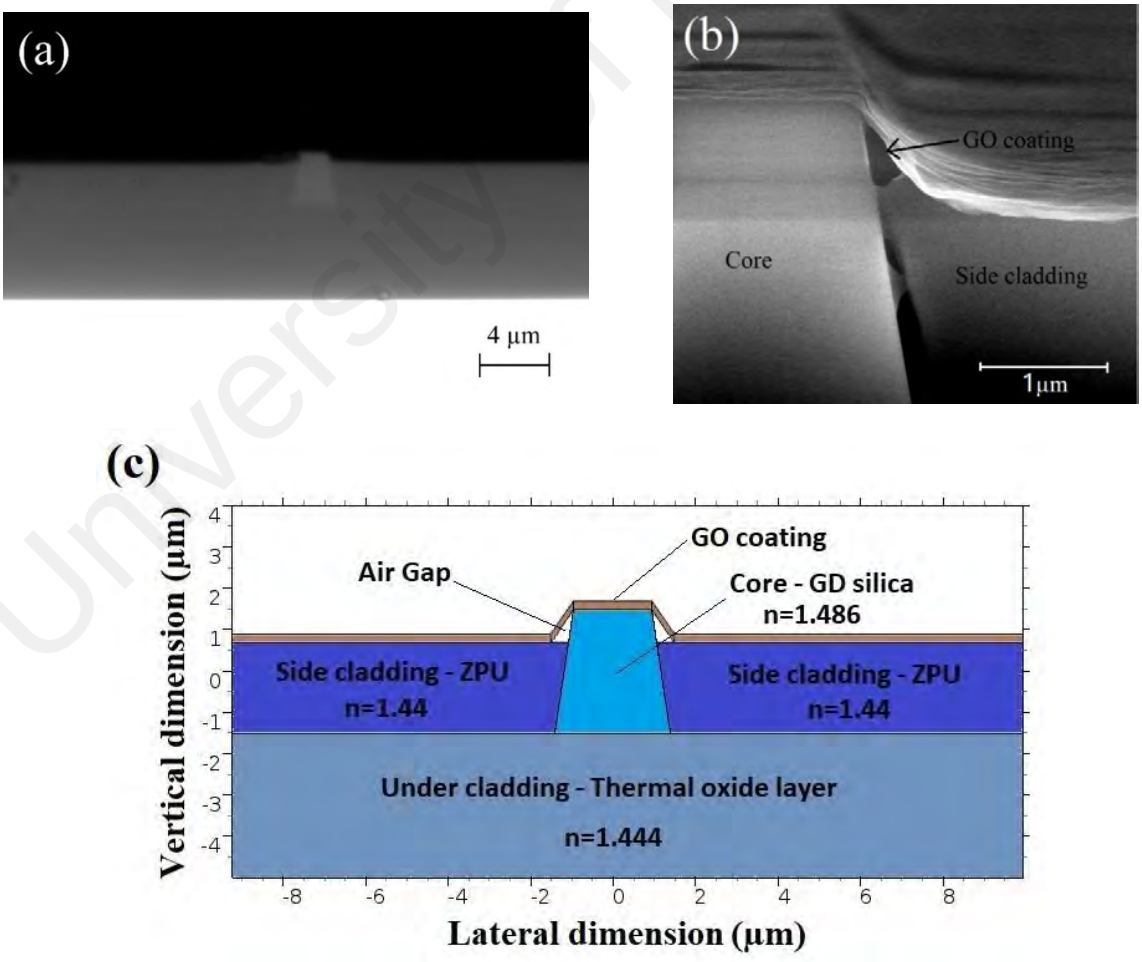

Figure 4.4: (a) Microscope image of the cleaved cross-section of waveguide. (b) FESEM image of the air gap formed between the GO sheet and protrusion section. (c) Corresponding structure model used for finite element analysis

4.5 Optical Characterization of GO-coated Planarized Optical Waveguide

The experiment set-up is shown in Figure 4.5. The light source used was a 1550 nm tunable laser source (TLS-AQ4321D). An ultra-high numerical aperture fiber (Nufern UHNA-3) was used for light coupling because of better NA and mode matching with the planarized optical waveguide. The 1550 nm light is coupled from UHNA fiber to waveguide input using butt-coupling technique, then an objective lens with 40x magnification and 0.45 NA was used to focus the waveguide output into a polarimeter (Thorlabs PAN5710IR3) and IR camera for polarization state measurement and mode profiling, respectively. The mode profile for the output beam of the planarized optical waveguide with different width is shown in Figure 4.6. The waveguides with 1 μm and 2 μm width only supports fundamental mode, whereas the higher order can be excited in addition to the fundamental mode by changing the input coupling condition (such as lateral misalignment between the input fiber and waveguide) for other waveguides which have a wider width (3 μm to 6 μm). On the other hand, for insertion loss and polarization dependent loss measurement, the objective lens and polarimeter/IR camera combination was replaced by an output UHNA fiber, and it was connected to an optical power meter (OPM; Thorlabs S144C). The absorption coefficient and extinction coefficient of GO-coated waveguide can be calculated from the insertion loss and polarization dependent loss measured. To ensure only single-mode excitation, planarized optical waveguide with 2 μm width is used in the optical characterization.

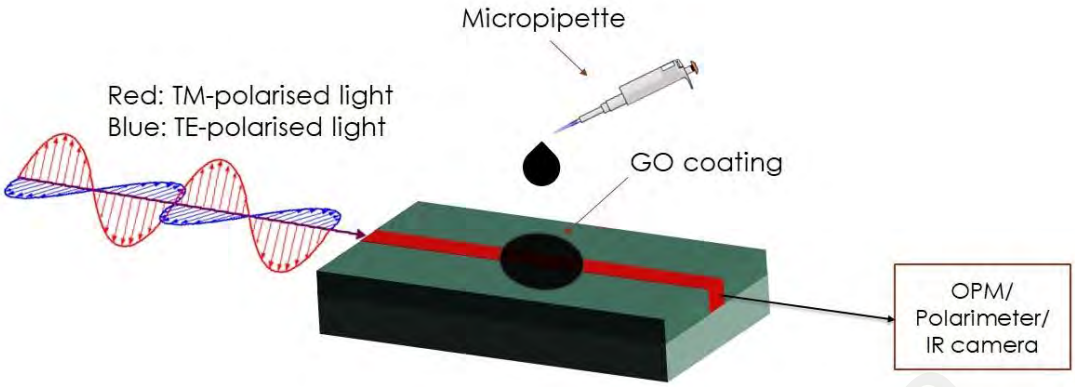

Figure 4.5: Experiment set-up for input fiber alignment, mode profiling of 1550 nm light propagating in waveguide core, and optical characterization of GO-coated waveguide.

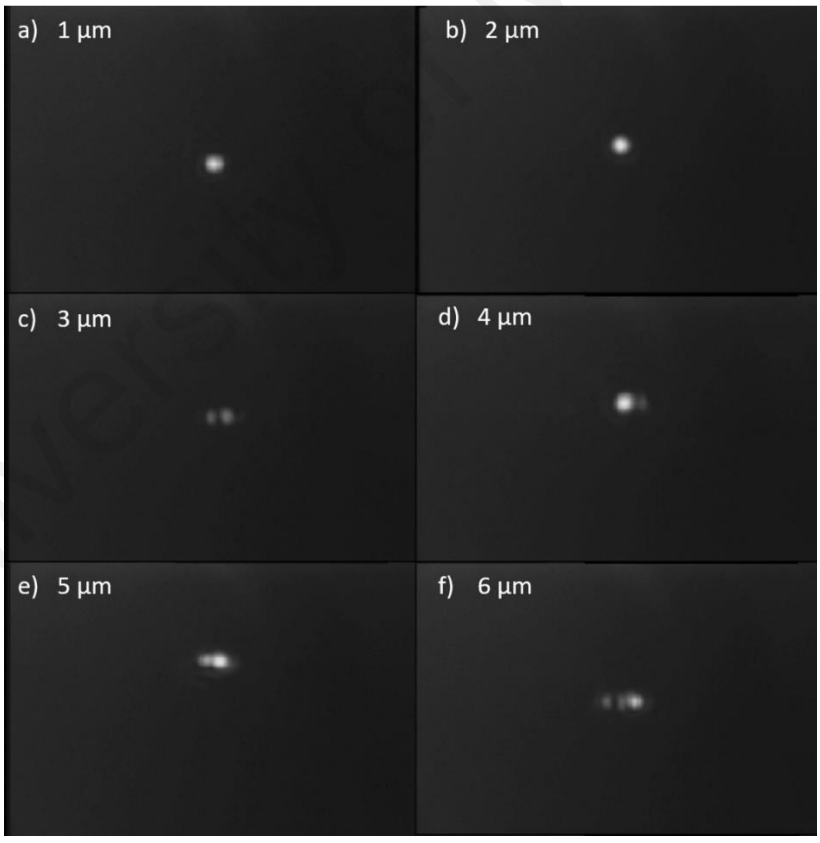

Figure 4.6: Mode profiling of 1550nm light at the output of the planarized optical waveguide with width of (a) 1 µm (b) 2 µm (c) 3 µm (d) 4 µm (e) 5 µm (f) 6 µm

4.6 Results and Discussions

4.6.1 Comparison of Experimental and Simulation Results

Figure 4.7 shows the experimentally obtained propagation loss per unit length of GO-coated planarized optical waveguide for both TM- and TE-polarized lights. The TM-mode propagation loss remains at a low level (1.5 to 9.7 $dB.mm^{-1}$) for coating thickness up to 0.42 μm. Then, the loss increases steeply to more than 61.3 $dB.mm^{-1}$ when the GO thickness exceeds 0.71 μm. Note that the x-axis error bar represents the standard deviation of GO coating thickness measured using surface profiler. For y-axis, the values are obtained from power measurement using optical power meter which has a very high measurement precision. In addition, the optical power measured is very stable, with a fluctuation of less than 3%. Therefore, the y-axis error bar is too small to be observable in Figure 4.7. However, for GO thickness higher than 0.7 μm, the transmitted power for TM-polarized light is close to, or lower than the detection limit of the OPM used, therefore the propagation loss for TM-mode at GO thickness greater than 0.7 μm may be even higher. On the other hand, the TE-mode propagation loss increases from 2.48 $dB.mm^{-1}$ to 44.5 $dB.mm^{-1}$ over the thickness range up to 0.34 μm, before falling to 15.1 $dB.mm^{-1}$ at thickness of 0.71 μm and increasing to 23.9 $dB.mm^{-1}$ at 1.04 μm thickness. The significantly different propagation loss-thickness profiles between TE- and TM-polarized lights shows that the optical response of GO-coated planarized optical waveguide is sensitive to the complex refractive index of the GO coating.

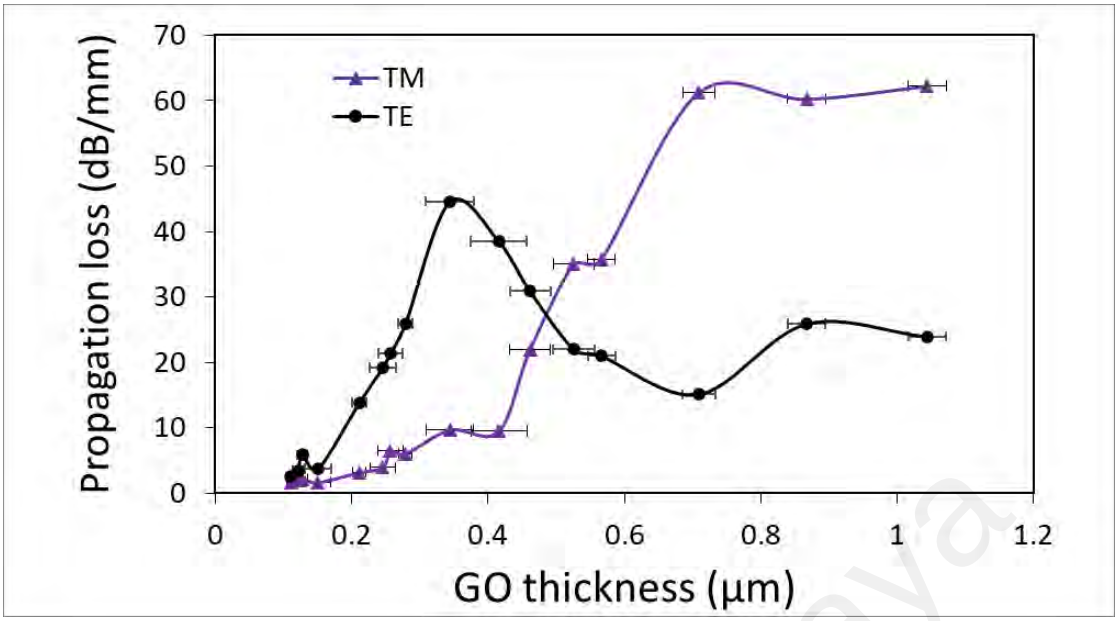

Figure 4.7: Propagation loss per unit length of GO-coated planarized optical waveguide for TM- and TE-polarized light with different GO coating thickness.

The abrupt increase in propagation losses, and hence extinction coefficient, for TM-polarised light when the thickness of the GO layer is increased beyond 0.4 μm, and also the maximum propagation loss happens at GO thickness of ~0.34 μm for TE-polarised light can both be explained by the power distribution of the optical mode in the GO-coated waveguide, as shown in Figure 4.8. For TE-polarised light, the modal power is mostly confined in the waveguide core at low GO thickness (up to ~0.2 μm), then the optical mode is having strong interaction with the GO coating when its thickness is increased to ~0.34 μm, and finally the mode is distributed back into the core at bigger GO thickness (0.5 μm to 1.0 μm). On the other hand, for TM-polarised light, the interaction is only between the evanescent field in the waveguide core and the GO-layer for a GO coating thickness up to 0.4 μm. When the GO coating thickness is greater than 0.4 μm, TM-polarised light is almost completely coupled into the GO coating and results in very high propagation loss.

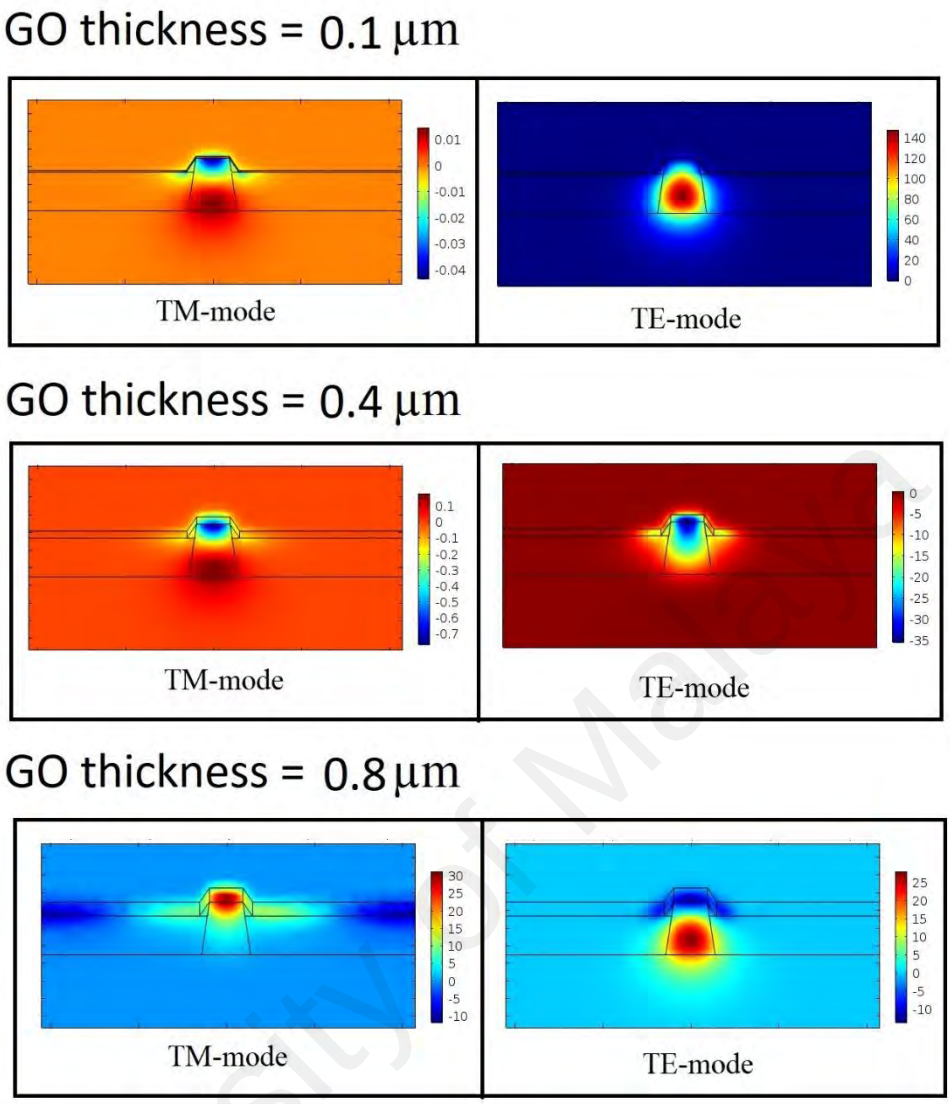

Figure 4.8: Simulated mode distributions for TM-polarised light in waveguide coated with GO-layer at thicknesses of 0.1 µm, 0.4 µm and 0.8 µm.

Figure 4.9 and Figure 4.10 shows the relationship between effective extinction coefficient (k_{eff}) of the GO-coated waveguide – calculated from the experimentally obtained propagation loss – and GO coating thickness, for TM-mode and TE-mode, respectively. Simulation results obtained using different real- (n_{GO}) and imaginary-part (k_{GO}) of complex refractive index are also included for comparison. From Figure 4.9 (a), it can be seen that the critical thickness where the abrupt increase in k_{eff} takes place becomes smaller with the increase of n_{GO}, with just a minor change in the rising gradient

of k_{eff} and the magnitude of k_{eff} at GO thickness between 0.5 μm and 1.0 μm. This is due to the higher tendency for the guided mode to be coupled into the GO coating when n_{GO} is higher. On the other hand, it can be seen that larger value of k_{GO} will result in larger k_{eff} for GO-coating thicknesses between 0.5 μm and 1.0 μm as well as a steeper gradient of increase at the critical thickness, as shown in Figure 4.9 (b). However, the critical thickness does not change by the variation of k_{GO}.

From Figure 4.10 (a), the increase in n_{GO} of GO coating will reduce the value of GO thickness where maximum k_{eff} takes place, with just a minor change of rising and falling gradient of the k_{eff} profile. On the other hand, Figure 4.10 (b) shows that larger value of k_{GO} will decrease the value of maximum k_{eff} of GO-coated waveguide, which corresponds to the decrease in the rising and falling gradients the precedes and follows the maxima, respectively. A negligible change in the thickness of GO coating where the maxima takes place is observed. Using the information gathered, the anisotropic complex refractive index values of GO film and their uncertainties can be determined through cross-refencing between experimental and simulation data. This is discussed in detail in section 4.6.2.

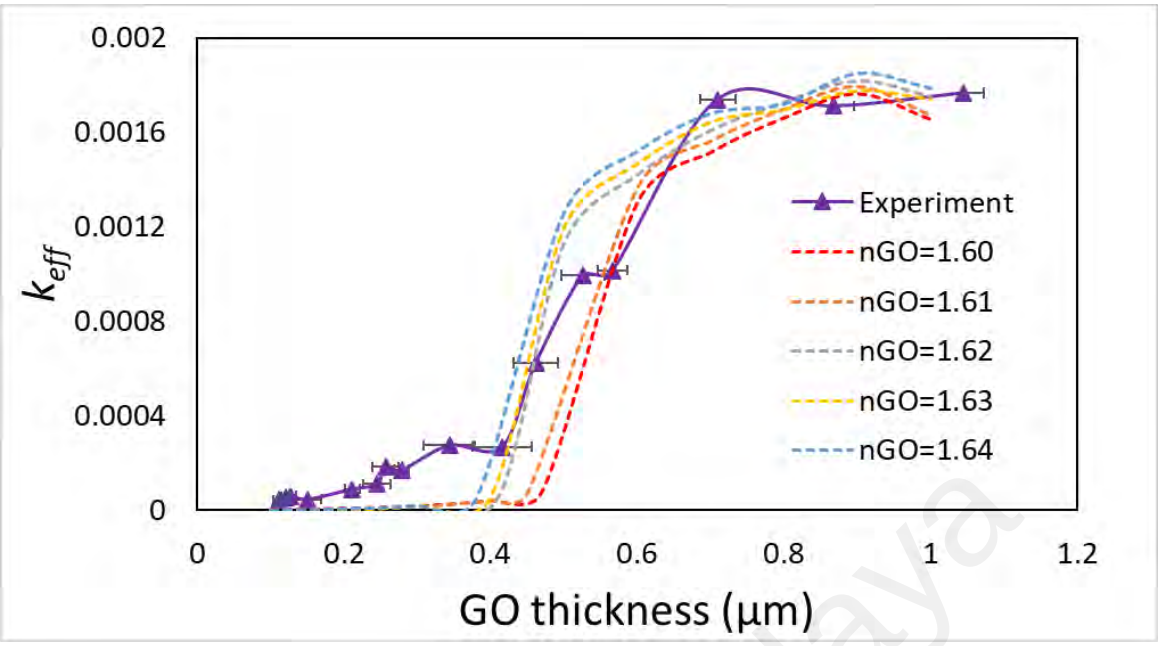

(a)

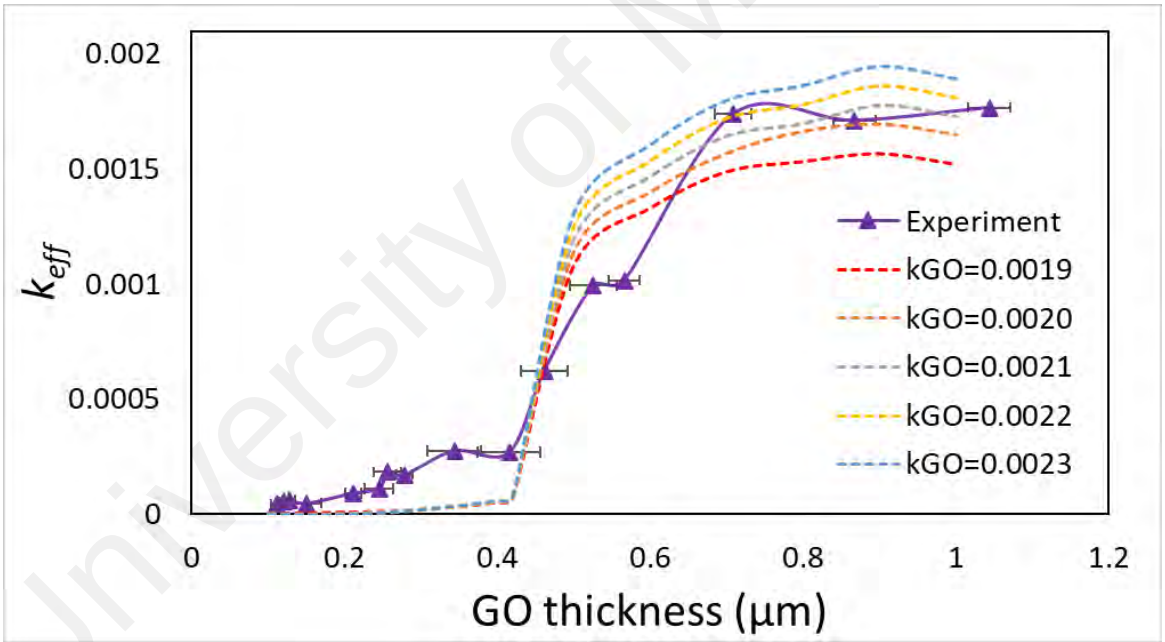

(b)

Figure 4.9: Change in effective extinction coefficient of GO-coated waveguide with variation of coating thickness for different values of (a) n_{GO} (with k_{GO} = 0.002) and (b) k_{GO} (with n_{GO}=1.615) of GO refractive index for TM-mode.

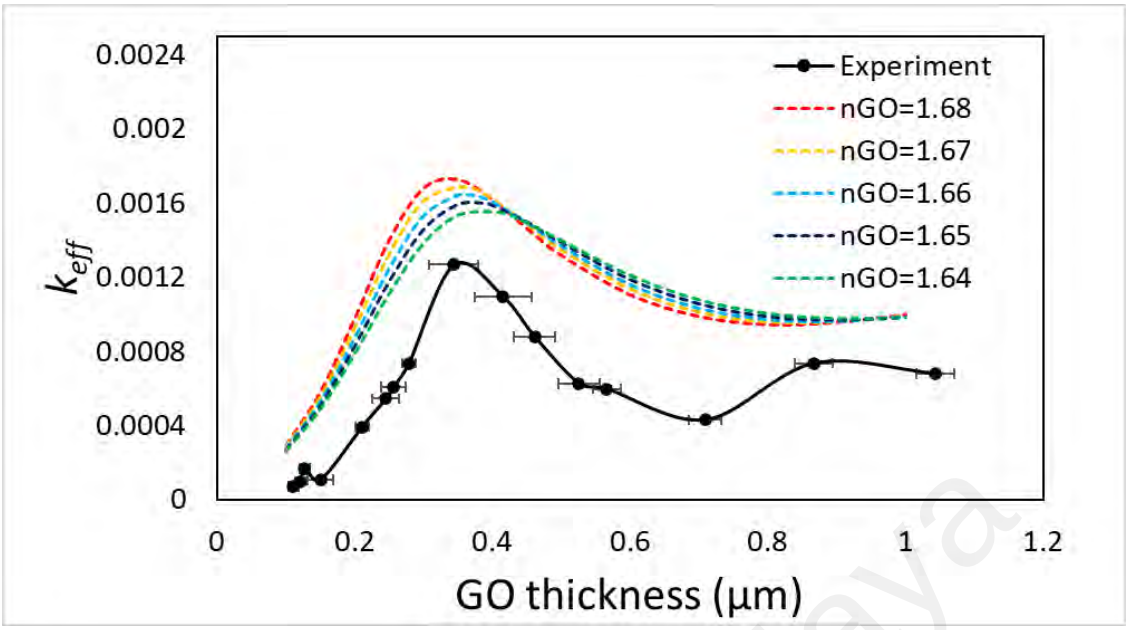

(a)

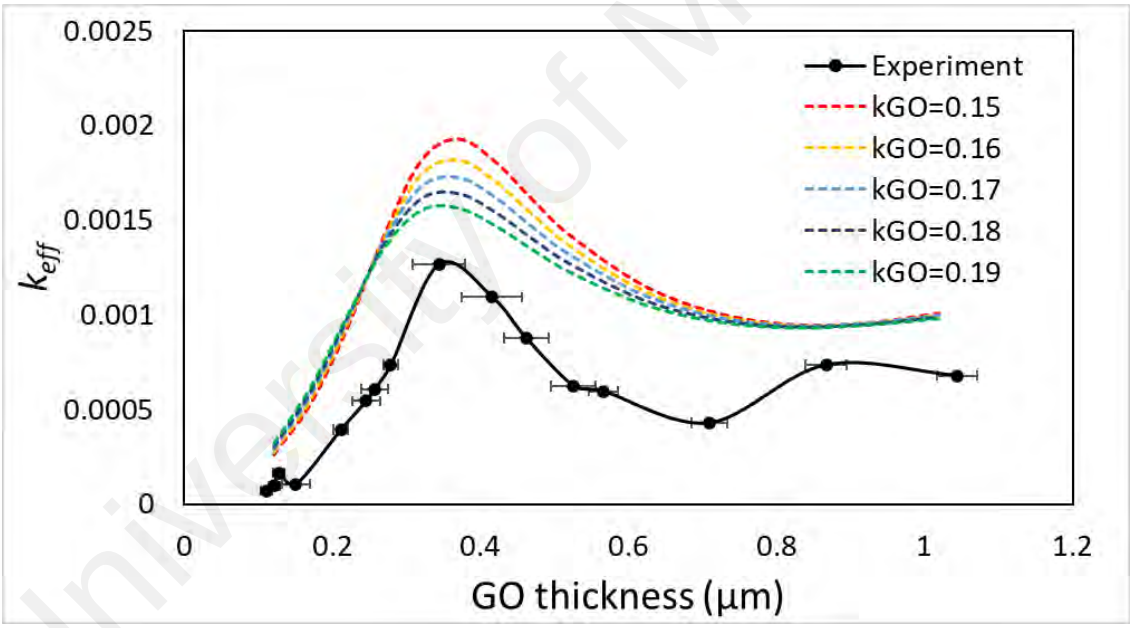

(b)

Figure 4.10: Change in effective extinction coefficient of GO-coated waveguide with variation of coating thickness for different values of (a) n_{GO} (with k_{GO}=0.17) and (b) k_{GO} (with n_{GO}=1.66) of GO refractive index for TE-mode.

4.6.2 Determination of complex refractive indices and their uncertainties

The determination of complex refractive index of GO thin film is based on the *figure-of-merit function* (or *"merit function"* for short) (Korn & Korn, 2000; Press et al., 1992). This function measures the agreement between the experimental data and the model with a particular choice of parameters, and is used in other optical measurement technique such as ellipsometry (Jellison, 1993). The merit function is conventionally arranged so that small difference between the selected experimental and simulation data represent close agreement (Press et al., 1992). The parameters of the fitting model are adjusted to achieve a minimum in the merit function to yield *best-fit parameters*. In this work, the fitting parameters and *figure-of-merit* of the self-design merit function are shown in Table 4.1 below.

Table 4.1: Fitting parameters and *figure-of-merit* of the self-design merit function

Fitting parameters	*Figure-of-merit*
Real part of GO complex refractive index for TM-mode, $n_{GO(TM)}$	GO thickness where abrupt increase in k_{eff} takes place
Real part of GO complex refractive index for TE-mode, $n_{GO(TE)}$	GO thickness where maximum k_{eff} occurs
Imaginary part of GO complex refractive index for TM-mode, $k_{GO(TM)}$	Gradient of the k_{eff} rising curve
Imaginary part of GO complex refractive index for TE-mode, $k_{GO(TE)}$	Positive and negative gradient for the rising and falling k_{eff} curve

As discussed in section 4.6.1, the experimental uncertainty mainly arises from the measurement uncertainty of GO coating thickness, and the maximum uncertainty in coating thickness is measured to be around 10% of the average thickness value. Therefore, a threshold of 10% is set in determining the uncertainties of GO complex refractive indices. However, an exception is applied in determining the uncertainty of k_{GO} for TM-polarized light. As can be seen from Figure 4.9, the GO coating thickness uncertainty is larger at GO thickness of 0.53 um and 0.57 um. As k_{GO} for TM-polarized light is determined from the gradient, which is acquired from this thickness range, the uncertainty of k_{GO} is expected to be larger. Therefore, a threshold of 20% is set in determining the uncertainty of the k_{GO} for TM-polarized light.

With the approach discussed above and the assumptions that (1) complex refractive index of GO remains constant with the increase of coating thickness from 0.1 um to 1.0 um and (2) the waveguide loss is negligible (all propagation loss is contributed solely by GO), the uncertainties of the real part of GO complex refractive index, Δn_{GO} for TM- and TE-polarized lights can be determined by the merit function (4.1) and (4.2), while the uncertainties of the imaginary part of GO complex refractive index, Δk_{GO} for TM- and TE-polarized lights can be determined using merit function (4.3) and (4.4) below.

$$\Delta n_{GO(TM)} = \left|\frac{S_{sim} - S_{exp}}{S_{exp}}\right| x100\% \tag{4.1}$$

where S_{sim} is the simulated value of GO thickness where abrupt increase in k_{eff} takes place;

S_{exp} is the experimental value of GO thickness where abrupt increase in k_{eff} takes place.

$$\Delta n_{GO(TE)} = \left|\frac{T_{sim}-T_{exp}}{T_{exp}}\right| x100\% \tag{4.2}$$

where T_{sim} is the simulated value of GO thickness where maximum k_{eff} occurs;

T_{exp} is the experimental value of GO thickness where maximum k_{eff} occurs.

$$\Delta k_{GO(TM)} = \left|\frac{Q_{sim}-Q_{exp}}{Q_{exp}}\right| x100\% \tag{4.3}$$

Where Q_{sim} is the gradient of the k_{eff} rising curve for simulation;

Q_{exp} is the gradient of the k_{eff} rising curve for experiment

$$\Delta k_{GO(TE)} = \left|\frac{(R-F)_{sim}-(R-F)_{exp}}{(R-F)_{exp}}\right| x100\% \tag{4.4}$$

where R_{sim} is the positive gradient of k_{eff} rising curve for simulation;

F_{sim} is the negative gradient of k_{eff} falling curve for simulation;

R_{exp} is the positive gradient of k_{eff} rising curve for experiment;

F_{exp} is the negative gradient of k_{eff} falling curve for experiment

Using merit function (4.1) to (4.4), the percentage of deviation of k_{eff} of the GO-coated optical waveguide for TM- and TE-polarized lights are plotted for different values of real part and imaginary part of GO complex refractive indices and are shown in Figure 4.11. By setting the 10% deviation threshold (and 20% deviation threshold for Δk_{GO} of GO for TM-polarized light), the uncertainties for the real part of the GO complex refractive index,

Δn_{GO} are ±0.020 and ±0.03 for TM- and TE-polarized lights, respectively. On the other hand, the uncertainties for the imaginary part of the GO complex refractive index, Δk_{GO} are ±0.001 and ±0.01 for TM- and TE-polarized lights, respectively.

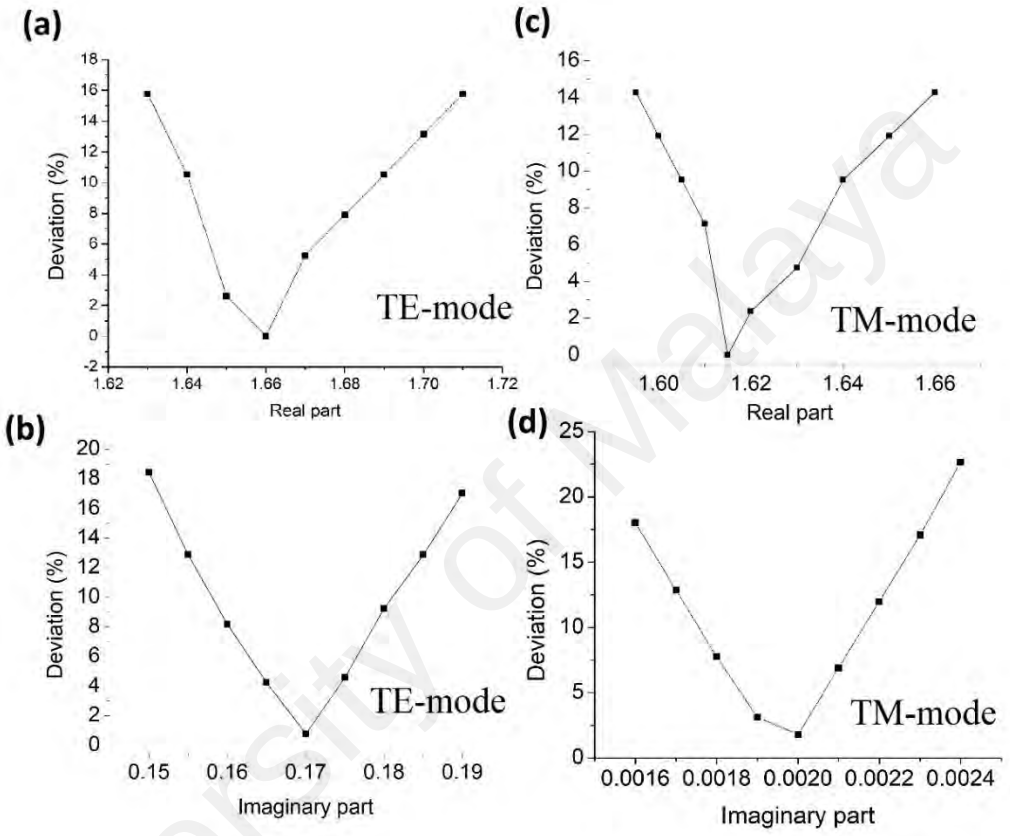

Figure 4.11: The deviation percentage of k_{eff} with the variation of (a) real part (at k_{GO}=0.17) and (b) imaginary part (at n_{GO}=1.66) for TE-polarized light along with the variation of (c) real part (at k_{GO}=0.002) and (d) imaginary part (at n_{GO}=1.615) for TM-polarized light

4.7 Summary

The anisotropic complex refractive index of GO for TM- and TE-polarised light at wavelength of 1550 nm, are determined to be $1.615 + 0.002i$ and $1.66 + 0.17i$, respectively. The uncertainties of FEM analysis for real part of complex refractive index are ±0.020 and ±0.03 for TM- and TE-polarised light respectively, whereas the uncertainties for the

imaginary part of complex refractive index is ±0.001 and ±0.01 for TM- and TE-polarised light respectively. Compared to other common optical technique, like spectroscopic ellipsometry which involves complicated model-based analysis and having limitation on determining the extremely low extinction coefficient, k value of certain material under tested, the proposed optical method on investigating the dielectric optical properties of GO by means of optical planar waveguide has given us an alternative and simpler approach to study the optical constant of suitable dielectric material.

CHAPTER 5: THESIS CONCLUSION AND FUTURE WORK

5.1 Conclusion

Determination of the anisotropic complex refractive index of GO by cross-referencing the polarization response of GO-coated planarized optical waveguide with finite element analysis has been successfully demonstrated. The demonstration is achieved with the successful accomplishment of the following:

1. Single mode planarized optical waveguide was designed based on silica as waveguide material. The planarized optical waveguide dimensions for single mode operation were found to be 2 μm in width and 3 μm in height. This is followed by the simulation of light propagation characteristics of planarized optical waveguide coated with thin film overlay of different complex refractive indices at the 1550 nm. The simulation results show that the effective mode index of thin film-coated planarized optical waveguide is highly dependent on the thickness of thin film coating. In addition, n_{eff} of planarized waveguide increases with the increase of refractive index of the thin film overlay but decreases with its extinction coefficient, while k_{eff} of planarized waveguide increases with the increase of both refractive index and extinction coefficient of the thin film overlay. Finally, by extending the coating thickness analysis, an in-plane TM-pass waveguide polarizer with very large PER (BP: 78.5 dB, GO: 97.7 dB) and low insertion loss can be produced using the anisotropic optical properties of BP and GO as the thin film overlay with optimized coating parameters.
2. Planarized optical waveguide was fabricated using a modified waveguide fabrication method. The refractive index of the waveguide core is 1.486, while side cladding (refractive index: 1.44) and bottom cladding have a refractive index of 1.44 and 1.444, respectively. The core dimension is 3 μm in height, while the top and bottom surface width are found to be 1.9 μm and 2.8 μm, respectively, which allows only the

excitation of fundamental mode at the wavelength of 1550 nm. On the other hand, GO was fabricated using modified Hummer's method. Then, GO thin film overlays were coated onto the planarized optical waveguide using drop casting technique to produce GO-coated planarized optical waveguide. The thickness of GO thin film was varied by drop casting GO solution with different concentration and by carrying out multiple drop casting. The polarization response of GO-coated planarized optical waveguide was then measured. The experimental results show that the change in propagation loss with different GO coating thickness are very distinct for TE- and TM-polarized lights. This distinction provides useful information of the polarization-dependent optical properties of GO thin film.

3. The strong polarization response of GO-coated planarized optical waveguide, together with finite element analysis, were used to determine the complex refractive index of the GO film. Using the *figure-of-merit function* approach, the complex refractive indices of the GO film at the wavelength of 1550 nm were determined be 1.66+0.17i and 1.615+0.002i for TE- and TM-polarised lights, respectively. Error analysis of this determination approach were also analyzed, and the uncertainties for the real parts of the refractive index were ±0.03 and ±0.020 for TE- and TM-polarised light, respectively. On the other hand, the uncertainties for the imaginary part of the refractive index were ±0.01 and ±0.001 for TE- and TM-polarized light, respectively.

The anisotropic complex refractive index values of GO obtained is valuable for the future development of GO-based optical telecommunication devices where NIR wavelengths are used as signal carrier. The advancement in optical telecommunication would in turn contribute significantly to national security, such as recovery from natural disaster, homeland security and military support. In addition, the thin film anisotropic complex refractive index determination method used in this work can be extended to the analysis of other thin film materials with large optical anisotropy.

5.2 Future Works

Based on the current achievements, a number of studies can be explored in the future. The current waveguide structure (straight channel) can only measure the insertion loss of the GO-coated waveguide, which is related to effective extinction coefficient of the waveguide. In this case, the anisotropic optical properties of GO is obtained via cross-referencing between simulation and experimental results of effective extinction coefficient. By designing more complex structures like Mach-Zehnder interferometer and micro-ring resonator on the same planarized optical waveguide platform, the complex refractive index of GO and other thin films can be determine using a more direct, analytical approach. Furthermore, the planarized optical waveguide platform can also be extended to study the nonlinear optical properties of GO and other thin films. Unlike conventional Z-scan technique that can only measure the nonlinear absorption and nonlinear refraction of a thin film sample in one polarization state, the nonlinear properties of GO thin film for both polarization states of light can be studied using the proposed platform with suitable waveguide structure designs.

REFERENCES:

Abergel, D., Russell, A., & Fal'ko, V. (2007). Visibility of graphene flakes on a dielectric substrate. *Applied Physics Letters, 91*(6), Article#063125.

Avouris, P. (2010). Graphene: electronic and photonic properties and devices. *Nano letters, 10*(11), 4285-4294.

Bao, Q., & Loh, K. P. (2012). Graphene photonics, plasmonics, and broadband optoelectronic devices. *ACS Nano, 6*(5), 3677-3694.

Bao, Q., Zhang, H., Wang, Y., Ni, Z., Yan, Y., Shen, Z. X., . . . Tang, D. Y. (2009). Atomic - layer graphene as a saturable absorber for ultrafast pulsed lasers. *Advanced Functional Materials, 19*(19), 3077-3083.

Batchman, T., & McWright, G. M. (1982). Mode coupling between dielectric and semiconductor planar waveguides. *IEEE Transactions on Microwave Theory and Techniques, 30*(4), 628-634.

Becerril, H. A., Mao, J., Liu, Z., Stoltenberg, R. M., Bao, Z., & Chen, Y. (2008). Evaluation of solution-processed reduced graphene oxide films as transparent conductors. *ACS Nano, 2*(3), 463-470.

Behabtu, N., Lomeda, J. R., Green, M. J., Higginbotham, A. L., Sinitskii, A., Kosynkin, D. V., . . . Kesselman, E. (2010). Spontaneous high-concentration dispersions and liquid crystals of graphene. *Nature Nanotechnology, 5*(6), Article#406.

Bonaccorso, F., Sun, Z., Hasan, T., & Ferrari, A. (2010). Graphene photonics and optoelectronics. *Nature Photonics, 4*(9), Article#611.

Bullock, J., Amani, M., Cho, J., Chen, Y.-Z., Ahn, G. H., Adinolfi, V., . . . Chueh, Y.-L. J. N. P. (2018). Polarization-resolved black phosphorus/molybdenum disulfide mid-wave infrared photodiodes with high detectivity at room temperature. *Nature Photonics, 12*(10), Article#601.

Chen, J.-L., & Yan, X.-P. (2010). A dehydration and stabilizer-free approach to production of stable water dispersions of graphene nanosheets. *Journal of Materials Chemistry, 20*(21), 4328-4332.

Chitara, B., Panchakarla, L., Krupanidhi, S., & Rao, C. (2011). Infrared photodetectors based on reduced graphene oxide and graphene nanoribbons. *Advanced Materials, 23*(45), 5419-5424.

Chong, W., Lim, W., Yap, Y., Lai, C., De La Rue, R., & Ahmad, H. (2016). Photo-induced reduction of graphene oxide coating on optical waveguide and consequent optical intermodulation. *Scientific Reports, 6*, Article#23813.

De La Torre, G., Vazquez, P., Agullo-Lopez, F., & Torres, T. (2004). Role of structural factors in the nonlinear optical properties of phthalocyanines and related compounds. *Chemical Reviews, 104*(9), 3723-3750.

Garcia-Caurel, E., De Martino, A., Gaston, J.-P., & Yan, L. (2013). Application of spectroscopic ellipsometry and Mueller ellipsometry to optical characterization. *Applied Spectroscopy, 67*(1), 1-21.

Gauthier, R. C., Medri, K. E., & Newman, S. R. (2012). Modal analysis and device considerations of thin high index dielectric overlay slab waveguides. *Applied Optics, 51*(9), 1266-1275.

Grigorenko, A., Polini, M., & Novoselov, K. (2012). Graphene plasmonics. *Nature Photonics, 6*(11), Article#749.

Harris, J., Shubert, R., & Polky, J. (1970). Beam coupling to films. *Journal of the Optical Society of America, 60*(8), 1007-1016.

Hofmann, U., & Holst, R. (1939). Über die Säurenatur und die Methylierung von Graphitoxyd. *Berichte der deutschen chemischen Gesellschaft (A and B Series), 72*(4), 754-771.

Hong, J., Lee, K., Son, B., Park, S., Park, D., Park, J.-Y., . . . Ahn, Y. (2013). Terahertz conductivity of reduced graphene oxide films. *Optics Express, 21*(6), 7633-7640.

Hummers, W. S., & Offeman, R. E. (1958). Preparation of graphitic oxide. *Journal of the American Chemical Society, 80*(6), 1339-1339.

Inagaki, M., & Kang, F. (2014). Engineering and applications of carbon materials. In (pp. 219-525): Butterworth-Heinemann, Waltham, MA.

Ingle, J. D., & Crouch, S. R. (1988). Spectrochemical Analysis.

Iogansen, L. (1967). Theory of Resonant Electromagnetic Systems with Total Internal Reflection. *Soviet Physics Technical Physics, 11*(11), Article#1529.

Jellison. (1993). Data analysis for spectroscopic ellipsometry. *234*(1-2), 416-422.

Jones, W. B. (1987). *Introduction to optical fiber communication systems.* Paper presented at the IEEE Workshop (10 June 1987), Washington, D.C.

Jung, I., Pelton, M., Piner, R., Dikin, D. A., Stankovich, S., Watcharotone, S., . . . Ruoff, R. S. (2007). Simple approach for high-contrast optical imaging and characterization of graphene-based sheets. *Nano Letters, 7*(12), 3569-3575.

Jung, I., Vaupel, M., Pelton, M., Piner, R., Dikin, D. A., Stankovich, S., . . . Ruoff, R. S. (2008). Characterization of thermally reduced graphene oxide by imaging ellipsometry. *The Journal of Physical Chemistry C, 112*(23), 8499-8506.

Kawachi, M. (1990). Silica waveguides on silicon and their application to integrated-optic components. *Optical and Quantum Electronics, 22*(5), 391-416.

Kim, K. S., Zhao, Y., Jang, H., Lee, S. Y., Kim, J. M., Kim, K. S., . . . Hong, B. H. (2009). Large-scale pattern growth of graphene films for stretchable transparent electrodes. *Nature, 457*(7230), Article#706.

Korn, G. A., & Korn, T. M. (2000). *Mathematical handbook for scientists and engineers: definitions, theorems, and formulas for reference and review*: Courier Corporation.

Kravets, V., Marshall, O., Nair, R., Thackray, B., Zhukov, A., Leng, J., & Grigorenko, A. (2015). Engineering optical properties of a graphene oxide metamaterial assembled in microfluidic channels. *Optics Express, 23*(2), 1265-1275.

Kumar, P., Subrahmanyam, K., & Rao, C. (2011). Graphene produced by radiation-induced reduction of graphene oxide. *International Journal of Nanoscience, 10*(04n05), 559-566.

Langhoff, P., & Karplus, M. (1969). Pade summation of the cauchy dispersion equation. *Journal of the Optical Society of America, 59*(7), 863-871.

Leijtens, X. (2011). JePPIX: the platform for Indium Phosphide-based photonics. *IET Optoelectronics, 5*(5), 202-206.

Lerf, A., He, H., Forster, M., & Klinowski, J. (1998). Structure of graphite oxide revisited. *The Journal of Physical Chemistry B, 102*(23), 4477-4482.

Li, C., Xie, Z., Chen, Z., Cheng, N., Wang, J., & Zhu, G. J. M. (2018). Tunable bandgap and optical properties of black phosphorene nanotubes. *Materials, 11*(2), Article#304.

Li, D., & Kaner, R. B. (2008). Graphene-based materials. *Science, 320*(5880), 1170-1171.

Li, L.-J., Gong, S.-S., Liu, Y.-L., Xu, L., Li, W.-X., Ma, Q., . . . Guo, X.-L. J. C. P. B. (2017). Temperature-induced effect on refractive index of graphene based on coated in-fiber Mach–Zehnder interferometer. *Chinese Physics B, 26*(11), Article#116504.

Li, M., Cushing, S. K., Zhou, X., Guo, S., & Wu, N. (2012). Fingerprinting photoluminescence of functional groups in graphene oxide. *Journal of Materials Chemistry, 22*(44), 23374-23379.

Li, W., Chen, B., Meng, C., Fang, W., Xiao, Y., Li, X., . . . Wang, H. (2014). Ultrafast all-optical graphene modulator. *Nano Letters, 14*(2), 955-959.

Liang, G., Hu, X., Yu, X., Shen, Y., Li, L. H., Davies, A. G., . . . Yu, S. F. (2015). Integrated terahertz graphene modulator with 100% modulation depth. *ACS Photonics, 2*(11), 1559-1566.

Liang, H. (2014). Mid-infrared response of reduced graphene oxide and its high-temperature coefficient of resistance. *Aip Advances, 4*(10), Article#107131.

Lim, W., Yap, Y., Chong, W., & Ahmad, H. (2014a). All-optical graphene oxide humidity sensors. *Sensors, 14*(12), 24329-24337.

Lim, W., Yap, Y., Chong, W., Pua, C., Huang, N., De La Rue, R., & Ahmad, H. (2014b). Graphene oxide-based waveguide polariser: From thin film to quasi-bulk. *Optics Express, 22*(9), 11090-11098.

Liu, M., Yin, X., Ulin-Avila, E., Geng, B., Zentgraf, T., Ju, L., . . . Zhang, X. (2011). A graphene-based broadband optical modulator. *Nature, 474*(7349), Article#64.

Liu, Z.-B., Xu, Y.-F., Zhang, X.-Y., Zhang, X.-L., Chen, Y.-S., & Tian, J.-G. (2009a). Porphyrin and fullerene covalently functionalized graphene hybrid materials with large nonlinear optical properties. *The Journal of Physical Chemistry B, 113*(29), 9681-9686.

Liu, Z., Robinson, J. T., Sun, X., & Dai, H. (2008). PEGylated nanographene oxide for delivery of water-insoluble cancer drugs. *Journal of the American Chemical Society, 130*(33), 10876-10877.

Liu, Z., Wang, Y., Zhang, X., Xu, Y., Chen, Y., & Tian, J. (2009b). Nonlinear optical properties of graphene oxide in nanosecond and picosecond regimes. *Applied Physics Letters, 94*(2), Article#021902.

Mathkar, A., Tozier, D., Cox, P., Ong, P., Galande, C., Balakrishnan, K., . . . Ajayan, P. M. (2012). Controlled, stepwise reduction and band gap manipulation of graphene oxide. *The Journal of Physical Chemistry Letters, 3*(8), 986-991.

Mattevi, C., Eda, G., Agnoli, S., Miller, S., Mkhoyan, K. A., Celik, O., . . . Chhowalla, M. (2009). Evolution of electrical, chemical, and structural properties of transparent and conducting chemically derived graphene thin films. *Advanced Functional Materials, 19*(16), 2577-2583.

Matthias Vaupel, U. S. *Application Note Graphene and Graphene Oxide*: Accurion GmbH, Stresemannstrasse 30, 37079 Goettingen, Germany.

Mermoux, M., Chabre, Y., & Rousseau, A. (1991). FTIR and 13C NMR study of graphite oxide. *Carbon, 29*(3), 469-474.

Nair, R., Wu, H., Jayaram, P., Grigorieva, I., & Geim, A. (2012). Unimpeded permeation of water through helium-leak–tight graphene-based membranes. *Science, 335*(6067), 442-444.

Nakajima, T., Mabuchi, A., & Hagiwara, R. (1988). A new structure model of graphite oxide. *Carbon, 26*(3), 357-361.

Nakajima, T., & Matsuo, Y. (1994). Formation process and structure of graphite oxide. *Carbon, 32*(3), 469-475.

Novoselov, K. S., Geim, A. K., Morozov, S. V., Jiang, D., Zhang, Y., Dubonos, S. V., . . . Firsov, A. A. J. s. (2004). Electric field effect in atomically thin carbon films. *Science, 306*(5696), 666-669.

Okamoto, K. (2006). *Fundamentals of optical waveguides*: Academic press.

Omidvar, A., Rashidian, V. M., & Jaleh, B. (2018). Enhancing the nonlinear optical properties of graphene oxide by repairing with palladium nanoparticles. *Physica E: Low-dimensional Systems and Nanostructures, 103*, 239-245.

Omidvar, A., Rashidian, V. M., Jaleh, B., Shabestari, N. P., & Noroozi, M. (2016). Metal-enhanced fluorescence of graphene oxide by palladium nanoparticles in the blue–green part of the spectrum. *Chinese Physics B, 25*(11), Article#118102.

Organization, N. P. (2010). The Nobel Prize in Physics 2010.

Pan, D., Zhang, J., Li, Z., & Wu, M. (2010). Hydrothermal route for cutting graphene sheets into blue-luminescent graphene quantum dots. *Advanced Materials, 22*(6), 734-738.

Paniccia, M., Morse, M., & Salib, M. (2004). Silicon photonics. *Springer, Berlin*.

Pei, S., & Cheng, H.-M. (2012). The reduction of graphene oxide. *Carbon, 50*(9), 3210-3228.

Pei, S., Zhao, J., Du, J., Ren, W., & Cheng, H.-M. (2010). Direct reduction of graphene oxide films into highly conductive and flexible graphene films by hydrohalic acids. *Carbon, 48*(15), 4466-4474.

Popa, D., Sun, Z., Torrisi, F., Hasan, T., Wang, F., & Ferrari, A. C. (2010). Sub 200 fs pulse generation from a graphene mode-locked fiber laser. *Applied Physics Letters, 97*(20), Article#203106.

Press, W. H., Teukolsky, S. A., Flannery, B. P., & Vetterling, W. T. (1992). *Numerical recipes in Fortran 77: volume 1, volume 1 of Fortran numerical recipes: the art of scientific computing*: Cambridge university press.

Ruess, G. (1947). Über das graphitoxyhydroxyd (graphitoxyd). *Monatshefte für Chemie und verwandte Teile anderer Wissenschaften, 76*(3-5), 381-417.

Samassekou, H., Alkabsh, A., Wasala, M., Eaton, M., Walber, A., Walker, A., . . . Jayasekera, T. J. D. M. (2017). Viable route towards large-area 2D MoS2 using magnetron sputtering. *2D Materials, 4*(2), Article#021002.

Schöche, S., Hong, N., Khorasaninejad, M., Ambrosio, A., Orabona, E., Maddalena, P., & Capasso, F. J. A. S. S. (2017). Optical properties of graphene oxide and reduced graphene oxide determined by spectroscopic ellipsometry. *Applied Surface Science, 421*, 778-782.

Scholz, W., & Boehm, H. (1969). Untersuchungen am graphitoxid. VI. Betrachtungen zur struktur des graphitoxids. *Zeitschrift für anorganische und allgemeine chemie, 369*(3-6), 327-340.

Schwierz, F. (2010). Graphene transistors. *Nature Nanotechnology, 5*(7), Article#487.

Sehrawat, P., Islam, S., Mishra, P., & Ahmad, S. (2018). Reduced graphene oxide (rGO) based wideband optical sensor and the role of Temperature, Defect States and Quantum Efficiency. *Scientific Reports, 8*(1), Article#3537.

Sellmeier, W. (1871). Zur Erkarung der abnormen Farbenfolge im Spectrum einiger. Substanzen. *Annalen der Physik und Chemie, 219*, 272-282.

Shang, J., Ma, L., Li, J., Ai, W., Yu, T., & Gurzadyan, G. G. (2012). The origin of fluorescence from graphene oxide. *Scientific Reports, 2*, Article#792.

Shen, Y., Zhou, P., Sun, Q., Wan, L., Li, J., Chen, L., . . . Wang, X. (2011). Optical investigation of reduced graphene oxide by spectroscopic ellipsometry and the band-gap tuning. *Applied Physics Letters, 99*(14), Article#141911.

Shibayama, J., Ando, R., Nomura, A., Yamauchi, J., & Nakano, H. (2008). Simple trapezoidal recursive convolution technique for the frequency-dependent FDTD analysis of a Drude–Lorentz model. *IEEE Photonics Technology Letters, 21*(2), 100-102.

Siochi, E. J. (2014). Graphene in the sky and beyond. *Nature Nanotechnology, 9*(10), Article#745.

Sobon, G., Sotor, J., Jagiello, J., Kozinski, R., Zdrojek, M., Holdynski, M., . . . Abramski, K. M. (2012). Graphene oxide vs. reduced graphene oxide as saturable absorbers for Er-doped passively mode-locked fiber laser. *Optics Express, 20*(17), 19463-19473.

Sun, P., Ma, R., Wang, K., Zhong, M., Wei, J., Wu, D., . . . Zhu, H. (2013). Suppression of the coffee-ring effect by self-assembling graphene oxide and monolayer titania. *Nanotechnology, 24*(7), Article#075601.

Sun, X., Liu, Z., Welsher, K., Robinson, J. T., Goodwin, A., Zaric, S., & Dai, H. (2008). Nano-graphene oxide for cellular imaging and drug delivery. *Nano Research, 1*(3), 203-212.

Sun, Z., Hasan, T., Torrisi, F., Popa, D., Privitera, G., Wang, F., . . . Ferrari, A. C. (2010). Graphene mode-locked ultrafast laser. *ACS Nano, 4*(2), 803-810.

Taboada, J. M., Maki, J. J., Tang, S., Sun, L., An, D., Lu, X., & Chen, R. T. (1999). Thermo-optically tuned cascaded polymer waveguide taps. *Applied Physics Letters, 75*(2), 163-165.

Tanzilli, S., De Riedmatten, H., Tittel, W., Zbinden, H., Baldi, P., De Micheli, M., . . . Gisin, N. (2001). Highly efficient photon-pair source using periodically poled lithium niobate waveguide. *Electronics Letters, 37*(1), 26-28.

Tien, P., Martin, R., & Smolinsky, G. (1973). Formation of light-guiding interconnections in an integrated optical circuit by composite tapered-film coupling. *Applied Optics, 12*(8), 1909-1916.

Tien, P., Ulrich, R., & Martin, R. (1969). Modes of propagating light waves in thin deposited semiconductor films. *Applied Physics Letters, 14*(9), 291-294.

Tran, V. C., Viet, H. P., Eun, W. S., Jin, S. C., Seung, H. H., Eui, J. K., . . . Kohl, P. A. (2011). Temperature-dependent photoluminescence from chemically and thermally reduced graphene oxide. *Applied Physics Letters, 99*(4), Article#041905.

Tran, V. K., Tran, D. L., & Kim, H. W. (2015). A two-step method for the preparation of highly conductive graphene film and its gas-sensing property. *Materials Sciences and Applications, 6*(11), Article#963.

Tung, V. C., Allen, M. J., Yang, Y., & Kaner, R. B. (2009). High-throughput solution processing of large-scale graphene. *Nature Nanotechnology, 4*(1), Article#25.

Ullah, M. S., Yousuf, A. H. B., Es-Sakhi, A. D., & Chowdhury, M. H. (2018). *Analysis of optical and electronic properties of MoS2 for optoelectronics and FET applications.* Paper presented at the AIP Conference Proceedings (19 April 2018), Maharashtra, India.

Ulrich, R., & Torge, R. (1973). Measurement of thin film parameters with a prism coupler. *Applied Optics, 12*(12), 2901-2908.

Venugopal, G., Krishnamoorthy, K., Mohan, R., & Kim, S.-J. (2012). An investigation of the electrical transport properties of graphene-oxide thin films. *Materials Chemistry and Physics, 132*(1), 29-33.

Volkmann, H. (1966). Ernst Abbe and his work. *Applied Optics, 5*(11), 1720-1731.

Wang, S. J., Geng, Y., Zheng, Q., & Kim, J.-K. (2010). Fabrication of highly conducting and transparent graphene films. *Carbon, 48*(6), 1815-1823.

Wu, J., Yang, Y., Qu, Y., Xu, X., Liang, Y., Chu, S. T., . . . Moss, D. J. (2019). Graphene Oxide Waveguide and Micro‐Ring Resonator Polarizers. *Laser & Photonics Reviews, 13*(9), Article#1900056.

Xu, J. (2018). *Linear Optical Characterization of Graphene Structure*: Master Thesis, University of Waterloo, Canada.

Xu, J., Liu, J., Wu, S., Yang, Q.-H., & Wang, P. (2012). Graphene oxide mode-locked femtosecond erbium-doped fiber lasers. *Optics Express, 20*(14), 15474-15480.

Yang, K., Zhang, S., Zhang, G., Sun, X., Lee, S.-T., & Liu, Z. (2010). Graphene in mice: ultrahigh in vivo tumor uptake and efficient photothermal therapy. *Nano Letters, 10*(9), 3318-3323.

Yang, Y., Wu, J., Xu, X., Liang, Y., Chu, S. T., Little, B. E., . . . Moss, D. J. (2018). Invited Article: Enhanced four-wave mixing in waveguides integrated with graphene oxide. *APL Photonics, 3*(12), Article#120803.

Zhan, Z., Zheng, L., Pan, Y., Sun, G., & Li, L. (2012). Self-powered, visible-light photodetector based on thermally reduced graphene oxide–ZnO (rGO–ZnO) hybrid nanostructure. *Journal of Materials Chemistry, 22*(6), 2589-2595.

Zhang, H., Bao, Q., Tang, D., Zhao, L., & Loh, K. (2009a). Large energy soliton erbium-doped fiber laser with a graphene-polymer composite mode locker. *Applied Physics Letters, 95*(14), Article#141103.

Zhang, H., Tang, D., Zhao, L., Bao, Q., Loh, K., Lin, B., & Tjin, S. C. (2010a). Compact graphene mode-locked wavelength-tunable erbium-doped fiber lasers: from all anomalous dispersion to all normal dispersion. *Laser Physics Letters, 7*(8), Article#591.

Zhang, H., Tang, D. Y., Zhao, L., Bao, Q., & Loh, K. P. (2009b). Large energy mode locking of an erbium-doped fiber laser with atomic layer graphene. *Optics Express, 17*(20), 17630-17635.

Zhang, J., Yang, H., Shen, G., Cheng, P., Zhang, J., & Guo, S. (2010b). Reduction of graphene oxide via L-ascorbic acid. *Chemical Communications, 46*(7), 1112-1114.

Zhao, L., Tang, D., Zhang, H., Wu, X., Bao, Q., & Loh, K. P. (2010). Dissipative soliton operation of an ytterbium-doped fiber laser mode locked with atomic multilayer graphene. *Optics Letters, 35*(21), 3622-3624.

Zheng, X. (2016). *The optics and applications of graphene oxide*: PhD thesis, Swinburne University of Technology, Melbourne, Australia.

Zheng, X., Jia, B., Chen, X., & Gu, M. (2014). In Situ Third-Order Non-linear Responses During Laser Reduction of Graphene Oxide Thin Films Towards On-Chip Non-linear Photonic Devices. *Advanced Materials, 26*(17), 2699-2703.

Zhu, Y., Murali, S., Cai, W., Li, X., Suk, J. W., Potts, J. R., & Ruoff, R. S. (2010). Graphene and graphene oxide: synthesis, properties, and applications. *Advanced Materials, 22*(35), 3906-3924.

LIST OF PUBLICATIONS AND PAPERS PRESENTED

List of publications

1. **S.X. Gan**, C.K. Lai, W.S. Chong, W.Y. Chong, S. Madden, H. Ahmad. *Large polarization response of planarized optical waveguide functionalized with 2D material overlays.* Journal of Modern Optics, (2020) 1-7.
2. W.S. Chong, **S.X. Gan**, C.K. Lai, W.Y. Chong, D. Choi, S. Madden, R. De La Rue, H. Ahmad. *Configurable TE-and TM-pass Graphene Oxide-coated waveguide polarizer.* IEEE Photonics Technology Letters, (2020).
3. W.S. Chong, **S.X. Gan**, A.-T.H. Mohammed, W.Y. Chong, C.S. Lim, H. Ahmad. *Nanolitre solution drop-casting for selective area graphene oxide coating on planar surfaces.* Materials Chemistry and Physics, (2020) 122970.

Papers Presented

1. W. S. Chong, **S. X. Gan**, C. K. Lai, W. Y. Chong, S. Madden, D. Choi, R. De La Rue, H. Ahmad. *Using the polarisation response of planar optical waveguides to determine the anisotropic complex refractive index of graphene oxide thick films*. ECIO 2019.